Design and Control of a Compact Hydraulic Manipulator for Quadruped Robots

Bilal Ur Rehman

Doctor of Philosophy (Ph.D.)
University of Genova, Italy
Istituto Italiano di Tecnologia (IIT)
April 2016

Thesis Supervisors:

Dr. Claudio Semini
Principle Adviser
Department of Advanced Robotics
Istituto Italiano di Tecnologia (IIT)

Prof. Darwin G. Caldwell
Director
Department of Advanced Robotics
Istituto Italiano di Tecnologia (IIT)

Copyright © 2016 by Bilal Ur Rehman
All rights reserved

Declaration

I declare that this thesis was composed by myself and that the work contained therein is my own, except where explicitly stated otherwise in the text.

(*Bilal Ur Rehman*)

To my parents and grandparents

"Life consists of two days, one for you one against you. So when it's for you don't be proud or reckless, and when it's against you be patient, for both days are test for you." Ali (RA)

Abstract

A common shortcoming of quadruped robots is that they often lack manipulation capability. To overcome this limitation, a single or dual arm can be added to the body of the quadruped robot, to perform manipulation tasks and provide assistance for locomotion. However, a suitable robotic arm for a quadruped platform requires specific features which might not *all* be available in off-the-shelf manipulators (e.g, fast, torque-controlled, light-weight, compact and without external control unit).

On the other hand, the integration of the arm(s), opens new challenges such as: What is the optimal mounting position of the arm(s) on the quadruped robot? How can the mobility of the quadruped robot be maintained? When the integrated arm(s) interacts with the environment or carries an unknown payload, a fundamental issue arises because the Center of Mass (CoM) of the whole robot can be dramatically shifted and the overall robot balance can be affected.

To this end, the object of this dissertation is to make a significant contribution toward, the design and development of a novel, compact, hydraulic manipulator for quadruped robots that can be mount as a single or dual arm system. The design evolution of the robotic arm is presented step-by-step starting by defining: (a) robot performance, physical and design specifications; (b) estimation of required design parameters such as joint range-of-motion, torque, speed and the optimal shoulder base mounting position of single and dual arm system with a quadruped robot; and (c) based on simulation results, the selection of the commercially available actuators.

Furthermore, the mechanical design of the robotic arm is discussed. The designed robotic arm is compact ($0.745[m]$), light-weight $12.5[kg]$, without a big control unit and able to carry a heavy payload $10[kg]$. The robotic arm is called *HyArm*. It has six degree-of-freedom (DoF) actuated with a combination of hydraulic motors and cylinders. The $3DoF$ shoulder joint is actuated by hydraulic motors and the $1DoF$ elbow joint is designed with an optimized four bar linkage mechanism powered by hydraulic cylinder, whereas, the $2DoF$ wrist joint is actuated by a hydraulic motor and cylinder [Rehman et al., 2015].

We also developed low-level and high-level controllers for the designed robotic arm. We developed and tested a control framework which integrates the robotic arm and mobile platform to ensure mobility and balance [Rehman et al., 2016]. We carried out various experiments on the robotic arm with fixed and mobile platform multi-legged mobile manipulator. We presented experimental results on real robotic arm both with fixed base and mobile base.

Acknowledgements

First of all, my special and humble thanks is only for Almighty Allah, Who gave me the strength and opportunity to complete this research, by giving me a healthy and beautiful life, surrounded by amazing people and HIS help in difficult times.

Second, I would like to thank my supervisor and mentor, Dr. Claudio Semini for giving me the opportunity to do a Ph.D. at Dynamic Legged System Lab (DLS). Without his help and hardware designing experience in robotics *HyArm* would be still in designing phase. I am sincerely thankful for all his support, time, patience and teaching during my stay at the DLS lab.

Prof. Darwin Caldwell for his support, freedom for creativity, for sharing the vision to create such a robot, and giving me the opportunity to work under his leadership in IIT.

In this dissertation, you will also find *we* and *our* instead of *I*, because I believe this work would not have been possible without the contributions and support of countless people. I have greatly enjoyed working with different people from all over world, which has made me feel at home in this continent.

I would like to thank the following people:
Jake Goldsmith, thank you for the thorough support and help in each phase of mechanical design. Without Jake's help and inspiration, I wouldn't have been able to design such a amazing robot. Dr. Hamza Khan, thank you for your continuous support, feedback and motivations. Dr. Michele Focchi, thank you for teaching and helping me for dynamics simulation, low-level torque control and implementing the mobile platform controller. Dr. Marco Frigerio, thank you for introducing me to *RobCoGen* and helping me to understand the dark world of low-level software, EtherCAT, electronics, and amazing debugging scripts and tools. Dr. Jinoh Lee, thank you for helping with the arm controller tuning and your valuable support. Prof. Roy Featherstone, Dr. Ioannis Havoutis, Dr. Victor Barasuol, Dr. Stephane Bazeille, Carlos Mastalli, Marco Camurri, Felipe Polido, Jose Colmenares, Yifu Gao, Romeo Orsolino, and Alex Posatskiy, thank you for your valuable company and support throughout my stay. Dr. Nawid Jamali, thank you for your helping me with proof reading and also for amazing company and valuable feedback throughout my Ph.D. You truly played an important role to make me feel at home in this continent. Dr. Houman Dallali, thank you for your support during my Ph.D.

I would like to thank our team of technicians Marco Migliorini, Phil Hudson, Gianluca Pane, Giuseppe Sofia, Stefano Cordasco, and Alessio Margan. Also, I would like to thank our departmental secretaries for helping me with the most difficult tasks

regarding bureaucracy, purchasing and travelling arrangements. As well as the whole team of the Advanced Robotics Department of the Istituto Italiano di Tecnologia.

Last but not least, I would like to particularly thank my brothers Awais Ur Rehman and Muhammad Ali, and my sweet and lovely sister Kunza Muzammil, and all my family for all their affection and happiness. I sincerely thank to my beloved parents for keeping me motivated and for their unconditional love. I would like to express my deep gratitude to the above-mentioned people.

Contents

Abstract **7**

Acknowledgements **10**

List of Figures **15**

List of Tables **19**

1 Introduction **21**

- 1.1 Motivations 22
- 1.2 Project Objectives 24
- 1.3 Contributions 24
- 1.4 Outline 25

2 State of the Art **27**

- 2.1 Fixed-based manipulators 27
  - 2.1.1 Electrically actuated manipulators 28
    - 2.1.1.1 Barrett Technology 28
    - 2.1.1.2 DLR 28
    - 2.1.1.3 Robotnik 29
    - 2.1.1.4 Universal Robots 30
    - 2.1.1.5 HDT 30
  - 2.1.2 Hydraulically actuated manipulators 30
    - 2.1.2.1 FMC Schilling Robotics 31
    - 2.1.2.2 KNR systems 31
    - 2.1.2.3 HYDRO-LEK 33
- 2.2 Multi-legged Mobile manipulator 33
  - 2.2.1 AQUAROBOT 34
  - 2.2.2 HITACHI-ART Centaur 34
  - 2.2.3 KIST-Centaur 35
  - 2.2.4 Tsuda-Centaur 35
  - 2.2.5 BigDog 36
  - 2.2.6 WorkPartner 37
  - 2.2.7 Robonaut2-Centaur2 38
  - 2.2.8 Momaro 39
  - 2.2.9 Aero 40
  - 2.2.10 Grit 40
  - 2.2.11 TITAN-IX 40
  - 2.2.12 LAURON-V 41
  - 2.2.13 RoboSimian 41

2.2.14 Interact-Centaur 43
2.3 Torque Control 43

3 Robotic Arm Specifications, Design Studies, and Hardware Selection 45
3.1 Robot Specifications 45
3.1.1 Performance Specifications 45
3.1.2 Physical Specifications 46
3.1.3 Design Specifications 47
3.2 System Modeling 48
3.2.1 Kinematics Modeling 48
3.2.1.1 The Mobile Platform Kinematics 48
3.2.1.2 The Manipulator Kinematics 48
3.2.1.3 The Centaur-like Robot Kinematic 50
3.2.2 Dynamics Modeling 51
3.3 Simulation Based Design Study of Dual-arm System for Centaur-like Robot 52
3.3.1 Workspace Analysis of Manipulator(s) 52
3.3.1.1 Overall and Common Workspace of a Dual Arm System 53
3.3.2 Performance Indices Based Analysis of the Workspace 54
3.3.2.1 Manipulability Index 54
3.3.2.2 Dual-arm Manipulability Index 57
3.3.3 Optimization of Shoulder Base Attachment of Centaur-like Robot Based on Workspace Analysis and Performance Index 58
3.3.3.1 The Optimization result for Shoulder Base Attachment 60
3.3.4 Dynamics Simulation for Joints Torque and Speed Estimation . . 60
3.3.4.1 Lifting an Object 61
3.3.4.2 biceps curl 63
3.3.4.3 Pull Up 64
3.3.4.4 Wall Push-up 64
3.3.4.5 Fast Arm Reaction 64
3.3.4.6 Dynamics Simulation Results Analyses 66
3.4 Hardware Selection 67
3.4.1 Actuator Selection 67
3.4.1.1 Robotic Manipulator Joints Actuator Configuration . . 69
3.4.2 Servo Valve 70

4 Robotic Arm Hardware Design and Integration with HyQ 73
4.1 Robotic Arm System Overview 74
4.2 Mechanical design 74
4.2.1 Shoulder Design (3*DoF*) 77
4.2.2 Elbow design (1DoF) 77
4.2.2.1 Kinematics of Elbow Joint's Mechanism 78
4.2.2.2 Elbow Target Design Parameters and Constraints . . . 80
4.2.2.3 Elbow Joint Mechanism Optimization 81
4.2.3 Wrist design (2DoF) 84
4.2.3.1 Wrist Rotation 84
4.2.3.2 Wrist Flexion/Extension 84
4.3 Hydraulic Circuit 89
4.4 Electronics and Control System Layout 89
4.5 Hardware Integration of HyArm with HyQ 90
4.5.1 Single Arm Configuration 91

4.5.1.1 Single Arm Elbow-down Configuration 92
4.5.1.2 Single Arm Elbow-up Configuration 93
4.5.2 Dual Arm Configuration 93

5 Controllers of Robotic Arm and Mobile Platform 97
5.1 Hydraulic Model Based Low-level Torque Control of Robotic Arm . . . 97
5.1.1 Hydraulic dynamics 98
5.1.1.1 Model of the hydraulic rotary motor 98
5.1.1.2 Model of the Hydraulic Cylinder 101
5.1.2 Feedback Linearisation Torque Control 102
5.1.3 Outer Controller 103
5.2 High-level Controllers 103
5.2.1 The Arm Controller 103
5.2.2 Mobile platform controller 105
5.3 Payload estimation 109

6 Experimental Results and Discussion 111
6.1 Fixed Based Manipulator Experimental Results and Discussion 111
6.1.1 Sine Task for Fixed Base Robotic Arm Under Torque Control with and without Payload 111
6.1.2 Static Task Under Torque Control for Fixed Base Robotic Arm . 113
6.2 High-level Controllers Experimental Results and Discussion 113
6.2.1 Static base with moving arm 116
6.2.2 Arm controller tracking 117
6.2.3 Payload estimation 117
6.2.4 Walking tests with arm 117

7 Conclusion and Future Work 121
7.1 Conclusion 121
7.2 Future Work 122

A List of Publications 125

B Kinematics Model of 6-DoF Robotic arm 127
B.1 Forward Kinematic Model of 6-DoF Arm 127

C Video links 131

Bibliography 133

List of Figures

1.1 The centaur is a mythological creature (picture credits to www.scott-eaten.com) . . . 22
1.2 Conceptual tasks for the centaur-like robot (a) Workers have to wear fully enclosed protective suits when handling toxic materials. (b) workers can use robot in tele-operation for disposal purposes . . . 23
1.3 Conceptual tasks for the centaur-like robot (a) Opening a door (b) Body stabilization of the robot . . . 23

2.1 Picture of the WAM arm (Barrett Technology) . . . 28
2.2 Picture of the LWR III (DLR), along with external controller unit. . . . 29
2.3 Picture of (a) LWA4D (*Schunk*), (b) *Jaco*™ (Kinova) and (c) *PowerBall*® (Schunk) . . . 29
2.4 Universal Robots: UR3, UR5 and UR10 . . . 30
2.5 Picture of HDT robotic arm: (a) $MK1$ and (b) $MK2$ Dual arm system 31
2.6 FMC Schilling Robotics . . . 32
2.7 KNR systems: (a) HYDRA-UW Hydraulic Robot Arm - Under Water and (b) HYDRA-MP Hydraulic Robot Arm - Manipulator . . . 33
2.8 HYDRO-LEK . . . 34
2.9 HITACHI-ART . . . 35
2.10 KIST-Centaur . . . 36
2.11 Tsuda-Centaur . . . 36
2.12 BigDog . . . 37
2.13 The WorkPartner robot, picture taken from [Ylonen and Halme, 2002] . 38
2.14 Robonaut2-Centaur2 by NASA . . . 38
2.15 Momaro . . . 39
2.16 Aero . . . 40
2.17 Grit . . . 41
2.18 TITAN-IX demonstrating (a) walking, (b) changing tool and (c) manipulation task capabilities . . . 41
2.19 TITAN-IX, static leg manipulation demonstration . . . 42
2.20 LAURON V . . . 42
2.21 RoboSimian . . . 43
2.22 Interact Centaur . . . 43

3.1 HyQ: Hydraulically actuated Quadruped robot and its kinematic structure 49
3.2 The manipulator kinematic structure . . . 49
3.3 Centaur-like robot kinematic model . . . 51
3.4 Centaur-like robot arms workspace without mechanical joint limits . . . 53
3.5 Common vs overall workspace . . . 54

3.6 Common vs overall workspace relation 55
3.7 Centaur-like robot's workspace normalized manipulability index of each manipulator without mechanical joint limits 56
3.8 Centaur-like robot's workspace normalized manipulability index of each manipulator with mechanical joint limits 56
3.9 (a) Dual-arm Manipulability (DM) and (b) Dual-arm Manipulability Index (DMI). 57
3.10 DMI mountains 58
3.11 The Dual-arm Manipulability Index within common workspace of both manipulator 61
3.12 The dual-arm system of the Centaur-like robot workspace with mechanical joint limits and optimized shoulder base attachment. 62
3.13 Lifting an object required peak torque and velocity 63
3.14 Picture of the Centaur robot performing pull-up and push-up tasks . . . 63
3.15 Pull-up required peak torque and velocity 64
3.16 Wall push-up required peak torque and velocity 65
3.17 Fast arm reaction task 65
3.18 The summary of estimated required joint torque for each "representative" tasks simulated under payload 66
3.19 The summary of estimated required velocity for all simulated tasks. . . 66
3.20 Hydraulic cylinder and rotary actuators 68
3.21 70
3.22 The solid lines are flow-pressure requirements for each joint estimated with simulated data. The dashed line red line is Moog E24 servo-valve flow-pressure curve. 72

4.1 HyArm: A fully torque-controlled **Hy**draulic **A**rm. The labels in the figure show the 6 joint axes with abbreviated names: Shoulder Adduction/Abduction (SAA), Shoulder Flexion/Extension (SFE), Humerus Rotation (HR), Elbow Flexion/Extension (EFE), Wrist Rotation (WR), Wrist Flexion/Extension (WFE). A single spherical rubber ball is shown as end-effector which can be replaced by different grippers. 73
4.2 Shoulder and elbow joints configuration 75
4.3 The shoulder joints, CAD mechanical assembly in exploded view. 76
4.4 The elbow joint CAD mechanical assembly in exploded view. 78
4.5 Schematic of the elbow joint mechanism to map cylinder motion into elbow joint motion, eventually linear cylinder force to elbow joint torque. All the red nodes (e.g, (2),(3),(4),(5),(6),(8) and (R)) are free to rotate along their axis and black nodes (e.g, (1) and (7)) are fixed within mechanical constraints. 78
4.6 Fig. 4.5 schematic close-up. 79
4.7 Schematic close-up ofFig. 4.5 79
4.8 A 3^{rd} order polynomial approximation of required torque profile for elbow joint in red and blue dash line. 81
4.9 The Elbow joint torque profile with optimized design parameters 82
4.10 The elbow cylinder stroke vs joint angle 83
4.11 The real hardware implementation of the elbow joint mechanism 83
4.12 Wrist Rotation,WR 84
4.13 Wrist Flexion/Extension (WFE) 85
4.14 Schematic of WFE mechanism 85

4.15 The WFE joint torque profile with optimized design parameters. 86
4.16 The WFE cylinder stroke vs joint angle 87
4.17 Elbow design required torque profile 88
4.18 Hydraulic circuit schematic for HyArm. The main hydraulic power is supplied through two flexible hoses which can be connect directly to either hydraulic pump or HyQ. 89
4.19 Custom designed compact hydraulic manifolds for HyArm actuators. . . 90
4.20 Electronics and control system layout diagram for HyArm. 91
4.21 Various views of the arm workspace in an elbow-down configuration 1 with the arm base aligned with Z-axis of the mobile base frame: (a) X-Z plane, (b) Y-Z plane, (c) X-Y plan and (d) 3D view. 92
4.22 Various views of the arm workspace in an elbow-down configuration 2 with the arm base rotated 90[deg] w.r.t X-axis of the mobile base frame: (a) X-Z plane, (b) Y-Z plane, (c) X-Y plan and (d) 3D view. 93
4.23 Various views of the arm workspace in an elbow-up configuration with the arm base rotated 180[deg] w.r.t X-axis of the mobile base frame: (a) X-Z plane, (b) Y-Z plane, (c) X-Y plan and (d) 3D view. 94
4.24 Picture of IIT's HyQ robot [Semini et al., 2011] with the new hydraulic manipulator [Rehman et al., 2015] attached to its front creating a multi-legged mobile manipulator. 94
4.25 Centaur-like robot: The dual-arm system in (a) during operation and (b) stowed position 95

5.1 Block diagram of HyQ control framework inner loop is a low level joint torque control with a outer controller [Boaventura et al., 2012a] 97
5.2 Cross section of a single-vane rotary hydraulic actuator illustrating the principle of operation and definition of variables: u_v is control signal, p_a and p_b are the chamber pressures, v_a and v_b are the chamber volumes, q_a and q_b are the fluid flow in and out from chamber A and B, P_s and P_t are the supply and the tank return pressures, θ is vane position, τ is the actuator torque. 99
5.3 Cross section of asymmetric single rod cylinder hydraulic actuator illustrating the principle of operation and definition of variables: u_v is control signal, p_a and p_b are chamber pressures, v_a and v_b are chamber volumes A_a and A_b are piston and annulus areas, q_a and q_b are fluid flow in and out from chamber A and B, P_s and P_t are supply and tank return pressures, x_p piston position and F is actuator force. 100
5.4 Block diagram of feedback linearisation torque control 102
5.5 Summary of the nomenclature used for mobile platform controller. Leg labels: left front (LF), right front (RF), left hind (LH) and right hind (RH). The world frame W, the base frame B (attached to the geometric center of the robot body). Left subscripts indicate the reference frame, for instance $B^{x_{com}}$ is the location of the CoM w.r.t. the base frame. In case of no left subscript, quantities are expressed w.r.t. W. The C_i is i^{th} contact point between ground and i^{th} limb. The f_c is the ground reaction force (GRFs), where c is the number of stance feet. 106
5.6 Block diagram of the control framework. The trajectory generation block compute desired trajectories for robot CoM, the base orientation and joints, high level control computes the reference torques for the low-level controller. For further detail see Section 5.2.1 and 5.2.2. 108

6.1 Experiment 1: sinusoidal reference trajectory for all joints at 0.5Hz without payload. 112
6.2 Experiment 2: sinusoidal reference trajectory for all joints at 1Hz without payload. 113
6.3 Experiment 3: sinusoidal reference trajectory for all joints at 0.5Hz with 5kg payload. 114
6.4 Snapshots of the two experimental trials used to evaluate the performance of our low level control framework. From top to bottom: sinusoidal reference trajectory for all joints at 0.5Hz (first row) and with (second row) sinusoidal reference trajectory for all joints at 1Hz. A youtube video link is given in Chapter C in which HyArm is demonstrating torque controlled capability for both sine and static tasks. 114
6.5 Experiment 4: Static test for HyArm attached a fixed base. The external forces are applied by a user at the end-effector of HyArm to assess inner loop torque controller joint torque tracking performance. 115
6.6 Rejection of arm motion disturbances at $0.7Hz$, on the robot CoM with and without the mobile platform controller. Blue line represent the actual COM $Y[m]$ position. Whereas, the red line represent desired COM $Y[m]$ position. 116
6.7 Snapshots of the two experimental trials used to evaluate the performance of control framework. The robotic arm is mounted in front of HyQ. From left to right: Static tests with moving arm without (first column) and with (second column) mobile platform controller, respectively. 118
6.8 The first three shoulder joints position tracking: the blue dotted line represent the result of time delay controller and the red solid line represent the desired trajectory. 119
6.9 Payload estimation results of a $5kg$ payload added at the end-effector of robotic arm. The blue line represents payload to estimation and red line represents added payload at time $3.75s$. 119
6.10 Snapshots of the walking experimental to evaluate the performance of our framework. 120

B.1 The HyArm kinematics: Shoulder Adduction/Abduction (SAA), Shoulder Flexion/Extension (SFE), Humerus Rotation (HR), Elbow Flexion/Extension (EFE), Wrist Rotation (WR), Wrist Flexion/Extension (WFE), all the joint angles are shown at zero configuration 127

List of Tables

2.1 Summary of the key specifications of *WAM* (second column)and LWR III (third column) 28
2.2 Summary of the key specifications of *LWR4D*, *Jaco* and *PowerBall* . . 29
2.3 Summary of the key specifications Universal Robots 30
2.4 Summary of the key specifications HDT robotic arm 31
2.5 Schilling Robotic manipulator specifications 32
2.6 Summary of the key specifications KNR systems manipulators 33
2.7 HYDRO-LEK manipulator specifications 34

3.1 Summary of desired physical specifications for each arm 47
3.2 HyQ: specification overview and leg segment/part lengths and masses. . 50
3.3 Simulated robotic arm(s): link length and weight 50
3.4 Selected mechanical joint limits based on normalized manipulability index. 57
3.5 Optimized designed parameters for WFE joint 60
3.6 The estimated required joint specification based on simulation results. . 67
3.7 Specifications of small size commercially available hydraulic rotary motors 68
3.8 Specifications of small size commercially available hydraulic cylinders. Where (AC1-2) Asymmetric hydraulic Cylinder type 1 and 2, respectively. 68
3.9 Summary of a comparison between different actuators combination. For a fair comparison between hydraulic cylinder and motor weight, one should also consider the linkage assembly that convert cylinder force into respective joint torque. 69
3.10 Specification of hydraulic cylinder and rotary actuators 71
3.11 Peak Joint Speed and required Flow-Pressure 72

4.1 System Overview of the HyArm 74
4.2 The HyArm joint range-of-motion and torque output. See Fig. 3.2 to see the zero configuration of all the arm joint angles. 75
4.3 List of all the robotic arm segments and components with their weight. The total weight of each segment also includes the hydraulic motor or cylinder, servo valve, manifold torque or force sensor and position encoder. This list also provides hydraulic hoses and on board electronics total weight. 75
4.4 Optimized designed parameters 82
4.5 Optimized designed parameters for WFE joint 88

6.1 root-mean-square (RMS) value of peak to peak oscillation on CoM Y $[m]$ due to arm motion at different frequencies 116

B.1 The HyArm: link lengths 129

Chapter 1

Introduction

Today robots are able to access a wide range of terrain types with different level of difficulty. Wheeled and tracked robots have great maneuvrability in an environment where a terrain is smooth, flat, and with well-structured surfaces (e.g, roads, indoor environment). In recent years, there has been development in wheeled and tracked robots fields that led to success with off-road conditions (e.g, Curiosity Rover developed by JPL and 710 Kobra by iRobot). However, a majority of these robots still have limitations and difficulties to navigate in unstructured and rough terrain. To overcome these limitations in wheeled or tracks robots, along with studying the capabilities of legged animals, led researchers to develop biologically inspired legged robots.

How does a legged robot traverse highly uneven terrain where only a limited number of discrete footholds are possible (disaster sites, forests, etc) or the terrain is challenging (e.g, sand, snow, rubble, rocks, etc.)? And what does it do when it gets to its destination? We will briefly address these questions in the next paragraph.

The main body of the legged robot is decoupled from uneven ground by articulated legs. It allows the main the body of robot to be independent of the roughness of the terrain, where legs provide active suspension within their kinematic limitation, while a walking leg leave contact with the ground and goes from so-called lift-off phase to the swing phase. During the leg swing phase to land back to the ground, the legged robot can decide to land on selective footholds within its kinematic reach to traverse on highly uneven terrains. To this end, quadruped robots have the advantage (over bipeds) of improved balance, while not becoming overly complex (like hexapods). Traditionally quadrupeds have been limited to load carrying or observation tasks, as they have no manipulation ability. This thesis presents a “best-of-both-worlds” approach, by a bespoke arm system which can be mounted on a quadruped robot to create a centaurs-like robot.

The centaur is a mythological creature with the upper body of a human and lower body of a horse, as shown in Fig. 1.1. Similar to the centaur, half-human and half-horse composition in robotics can be exploited to achieve stability and manipulation capabilities.

The next section will try to answer the following questions: What are the motivations for mounting a dual arm system on a quadruped robot? What are its benefits? What are the possible applications for such a machine? And what are the motivations behind building a new robotic arm?

www.scott-eaton.com

Figure 1.1: The centaur is a mythological creature (picture credits to www.scott-eaten.com)

1.1 Motivations

In the field of legged robots, bipeds and quadruped robots are the most popular among researchers. The quadruped robots have the advantage of improved locomotion stability over rough terrain but lack in manipulation capability. Indeed, a combination of quadruped locomotion stability with the ability to perform manipulation tasks could become more crucial in natural disasters scenarios for search and rescue missions.

The Hydraulic Quadruped robot HyQ was developed at IIT to traverse complex and unstructured terrain for search and rescue missions in natural disaster scenarios [Semini et al., 2011]. In its normal standing posture, the body of HyQ is around 1m from the ground, weighs roughly 80kg, and features 12 torque-controlled joints powered by hydraulic actuators. HyQ has already shown a wide range of abilities such as trotting [Barasuol et al., 2013], running [Semini et al., 2015], jumping [Semini et al., 2012], step reflex [Focchi et al., 2013a], and navigation over unstructured terrain [Winkler et al., 2014].

However, similar to other quadruped robots, HyQ lacks manipulation ability. The arm system will add a new dexterous manipulation capability to the already wide range of abilities as mentioned above. HyQ is used as a test bench to attach arm, in a single or bimanual configuration, with the goal to work towards the creation of a centaur-like robot. Such a robot will be able to perform new tasks, including:

- The robot can be used for removal of toxic materials, such as in a nuclear power plant or in research facility during maintenance or regular operations. It can also be used to carry highly toxic or hazard materials for disposal or inactivation purposes (Fig. 1.2).
- The robot arms can be used to remove an obstacle or debris in order to clear the path for a human or robot in disaster areas.

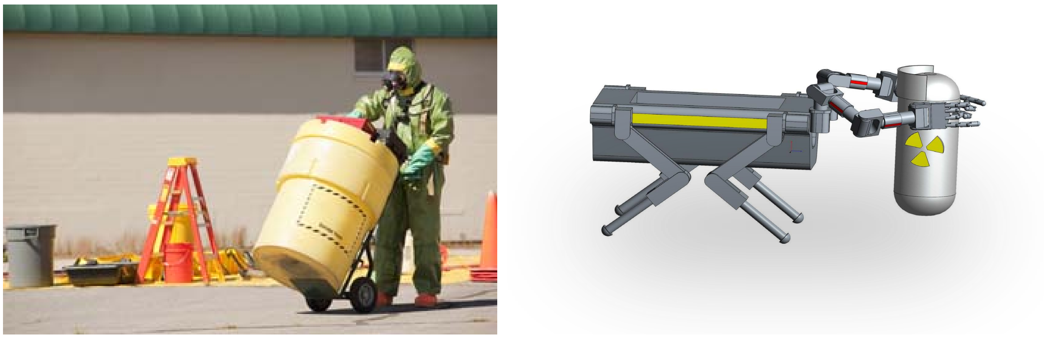

(a) (b)

Figure 1.2: Conceptual tasks for the centaur-like robot (a) Workers have to wear fully enclosed protective suits when handling toxic materials. (b) workers can use robot in tele-operation for disposal purposes

- The arms can be used to open a door or press a button to call a lift or close a valve to cut off the flow of fluid in disaster scenarios (Fig. 1.3a).
- The robot can use arms and legs to reach different locations, using front legs against walls to reach higher objects, or arms to provide assistance to robot while manipulating an object as shown in Fig. 1.3b.

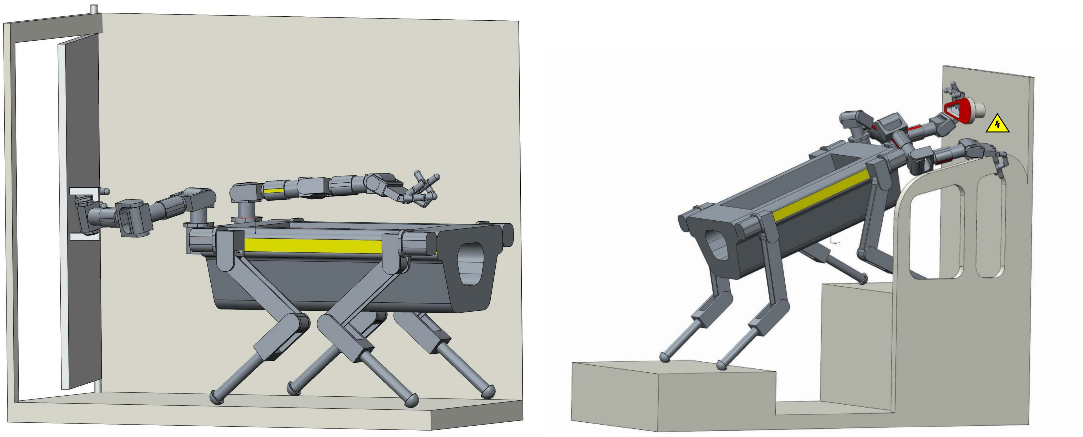

(a) Opening a door (b) Body stabilization of the robot

Figure 1.3: Conceptual tasks for the centaur-like robot (a) Opening a door (b) Body stabilization of the robot

The centaur-like robot can be used for the following potential applications:

1. For nuclear power plant maintenance, decommissioning or waste disposal.
2. In search and rescue missions, after disasters such as earthquakes in collapsed buildings.
3. As a fire fighting robot to provide visual information inside burning buildings, forests, to put down fire, or as an assistant for victims.

4. In forestry or the agriculture industry, for planting or harvesting.
5. Construction sites to transport bricks or to help build roads in highly remote and dangerous mountains.

Today, a huge variety of robotic arms are commercially available. Most of them suffer from limitations: Some are very heavy and allow only position control (e.g, the hydraulically actuated arms *Hydra-MP* by KNR and *ATLAS-7R* or *CONAN-7P* by Schilling Robotics (see section 2.1.2)). Others are torque controlled but need a bulky external control unit (*LWR*3 by DLR [Rainer et al., 2010]), are limited in joint-speed (*MK*1 by [HDT, 2013]), have low payload lifting capacity (Schunk's *LWA*3) or, like *WAM* sold by Barrett Technology [Townsend and Salisbury, 1993, WAM, 2013], have a heavy base ($27kg$) (sec section 2.1.1). The limitations of these existing manipulators reduce the number of potential application scenarios as mentioned earlier and the possibility to be integrated into an agile mobile robot such as HyQ.

The integration of the arms opens new challenges such as: What is the optimal mounting position of the arm on the mobile platform? How to maintain the mobility of the quadruped robot? When the integrated arm interacts with the environment or carries an unknown payload, a fundamental issue arises because the Center of Mass (CoM) of the whole robot can be dramatically shifted and the overall robot stability can be affected.

1.2 Project Objectives

The above mentioned reasons led to the design and development of a dual arm system for a quadruped to create a centaur-like robot. The objectives of the dissertation can be summarized as follows:

- To design and develop of a robotic arm which addresses all the above-mentioned limitations present in off-the-shelf manipulators;
- To investigate and analyse robot kinematics to estimate joint range-of-motion, propose various mounting positions for robotic arm(s) and select an optimal mounting position suitable for required applications;
- To design and develop a dynamic simulation of representative tasks in order to estimate design parameters such as joint velocity and torque for actuators selection;
- To study and address challenges involved in the development of new control algorithms for centaur-like robots; and
- To develop a novel research platform within Advanced Robotics Department (ADVR) in Istituto Italiano di Tecnologia (IIT).

1.3 Contributions

The contribution of this dissertation are:

- A survey on commercially available fixed based manipulators with potential to attach to quadruped robot to create a centaur-like robots and existing multi-legged mobile manipulators with focus on quadruped robots with single or dual manipulator(s).

- The design and development of a novel compact hydraulic manipulator for quadruped robots named “HyArm,” which address all the limitations present in off-the-shelf manipulators [Rehman et al., 2015]. It is fully torque-controlled, hydraulically actuated, light-weight, compact, and without any heavy external control unit. The robotic arm is designed in a systematic manner. First we developed a simulation of a centaur-like robot to acquire design parameters for the arm, such as joint range-of-motion, torque, and speed by simulating a number of dynamic “representative” tasks. I investigate and used simulation results to search for suitable commercially available hydraulic actuators and servo valve.
- A design of a special four-bar linkage mechanism (inspired by an excavator bucket joint) for elbow design of the robotic arm (see Chapter 4). I optimized each link length of linkage mechanism to acquire the required torque profile for the robotic arm elbow and wrist joint.
- An integration of HyArm with HyQ to create a multi-legged mobile Platform and implemented the high-level arm controller [Rehman et al., 2016]. Whereas, the mobile platform controller is proposed and implemented by [Focchi et al., 2015].

1.4 Outline

This document describes in details the design and development of a dual arm system for a quadruped to create a centaur-like robot. It is intended to serve as a base for development of future similar robots. To this end, this thesis is organized in logical and sequential chapters as follows:

- Chapter 2 first introduces the state of the art summarizing the commercially available fixed base manipulators with potential to attach to quadruped robots to create centaur-like robots. Then, existing multi-legged mobile manipulators with focus on quadruped robots (four-legged) with single or dual manipulator(s). It also includes hybrid mobile manipulator which use legs and wheels for locomotion. Also, it presents a literature overview of actuator and mechanical components, sizing and selection. This chapter will end with a brief literature overview of model based torque control.
- Chapter 3 starts by defining performance, physical, and design specifications of a robotic arm to develop a centaur-like robot. Then, it presents system modelling of the robot in terms of kinematics and dynamics. This chapter continues with workspace analysis of a dual arm system for selection of design parameters (e.g, the distance between shoulder base links and the orientation with respect to base robot torso) for attachment manipulators with a quadruped robot, And joint range-of-motion of each joint based on task specifications and performance indices. It also examines the dynamic simulation of representative tasks to estimate design parameters such as required joint velocity and torque for selection actuators and mechanical components. This chapter ends with (1) a case study on suitable commercially available hydraulic actuators and their selection, (2) mapping simulation results to actuators; and (3) required flow estimation for servo valve selection.
- Chapter 4 describes the mechanical design of a hydraulically actuated arm for a quadruped robot [Rehman et al., 2015]. I named the robot HyArm, which is the

abbreviation for **Hy**draulic **Arm** and pronounced [hai-a:m]. This chapter starts with a system overview, presenting key specification of designed robotic arm. Then, it continuous with the mechanical design of HyArm which is divided into shoulder, elbow and wrist joints design. It ends with description of the hydraulic circuit, electronics and control system layout for designed robot and the hardware system integration of the manipulator and mobile platform.

- Chapter 5 presents a model based torque control approach. This chapter will explain why we adopted and how we extended HyQ low-level control framework for hydraulically actuated robotic arm with $6DoF$ in series. I will present a control framework which will integrate the two controllers: (a) the arm controller that estimates and compensates external/internal disturbances; and (b) the mobile platform controller which optimizes the ground reaction forces to balance the decentralized load added by the weight of the attached robotic arm.
- Chapter 6 shows the experimental results to assess the low-level torque control and high-level arm and mobile platform controller.
- Chapter 7 will concludes and give future directions.

Chapter 2

State of the Art

This dissertation describes the design and control of a fully-torque-controlled, compact hydraulically actuated robotic arm for quadruped robots to create a centaur-like robot. The centaur-like robot belongs to the class of multi-legged mobile manipulator robots. A mobile manipulator robot is not rigidly attached to the ground but can freely move anywhere in the space and interact with the environment. When interacting with environment, it requires to sense the interaction and to be able to apply certain forces to perform different tasks. The interaction with environment is better dealt with in the torque domain rather than in position control. To this end, this chapter continues with State-of-the-Art (SoA) in the field of fixed and mobile manipulators.

First, we will present SoA of fixed based manipulators. Today, a vast variety of fixed manipulator are commercially available. It would not be possible to report every single one of them. Therefore, SoA is limited to only torque controlled manipulators with potential to attach to a multi-legged mobile platform such as HyQ. On other hand, position controlled manipulators cannot be completely neglected. Most existing hydraulically actuated manipulators are position controlled and cannot be mounted on mobile platform.

Second, this chapter will continue to present related work on mobile manipulators. Today there exists a vast variety of mobile manipulators. They can be categorized based on their: (a) locomotion system that allows motion by legs only, or as combination of legs and wheels (hybrid), or by wheels only, (b) their actuation system; and (c) target mobility environment such as ground, water or space. The SoA of mobile manipulator focuses on quadruped robots with single or dual manipulator(s). It also includes hybrid mobile manipulators which use legs and wheels for locomotion.

Third, since the designed robotic arm is fully torque controlled, I also present a literature overview of model based torque control.

2.1 Fixed-based manipulators

A robotic manipulator is generally mounted on a fixed platform (rigidly attached to ground) to reach different locations and to perform various tasks. Today, a vast variety of fixed base robotic manipulators are available. The SoA is limited to manipulator with potential to attach with a multi-legged mobile platform such as HyQ. The fixed-based manipulator can be characterised on the basis of their actuation system. Currently, the majority of commercially available fixed-based manipulators are electrically actuated, however hydraulically manipulators are also available. Based on different actuation types, SoA for fixed-based manipulators are presented as next.

2.1.1 Electrically actuated manipulators

A brief description of today commercially available electrically actuated robotic arms are given below, along with their key specifications.

2.1.1.1 Barrett Technology

The WAM (Fig. 2.1) was developed by $BarrettTechnology$ [Townsend and Salisbury, 1993, WAM, 2013]. It is a fully torque controlled $7DoF$ robotic arm. The WAM has $3kg$ payload lifting capacity and weighs of $32.8kg$ including heavy base. Table. 2.1 summarize the key specifications of WAM.

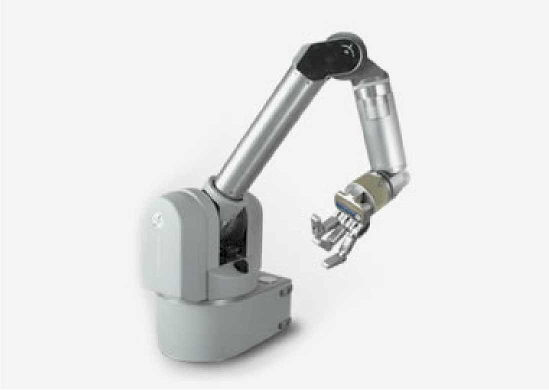

Figure 2.1: Picture of the WAM arm (Barrett Technology)

Manufacturer/reseller	Barrett Technology	DLR
Model name	WAM	LWR III
Arm extension	$1.0m$	$0.936m$
Weight	$32.8kg$	$14kg$ (without external unit)
Maximum payload at full reach	$3kg$	$14kg$
Degree of freedom	$7Dof$	$7Dof$
Control mode	Position/torque	Position/torque

Table 2.1: Summary of the key specifications of WAM (second column)and LWR III (third column)

2.1.1.2 DLR

DLR developed the Light Weight Robotic arm (LWR III) (Fig. 2.2)) [Bischoff et al., 2010]. The LWR III weighs $14kg$ (without control unit) and $14kg$ payload lifting capacity. Table. 2.1 summarize the key specifications of LWR III. It has $7DoF$ which enable to achieve human-like dexterity. The LWR III has maximum reach up-to $936mm$ and actuated by electric motors. Each joint contains two position and a torque sensor which enables to be in position or torque/impedance control. The LWR III comes with a heavy external control unit.

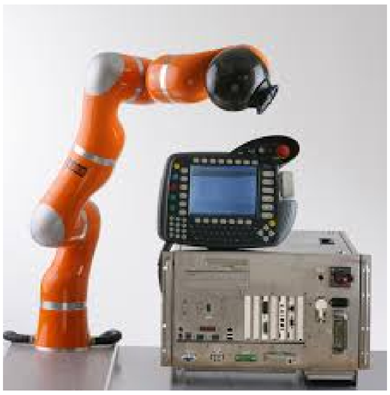

Figure 2.2: Picture of the LWR III (DLR), along with external controller unit.

2.1.1.3 Robotnik

The Robotnik is the reseller of robotic arms which provides *LWA4D*, *Jaco*, and *PowerBall* arms. Table. 2.2 summarizes the key specifications of each robotic arm.

The *LWR4D* is actuated by *Schunk* electric motor modules. Each module includes power stage, controller and motor-gear that result in an arm without an external control unit (Fig. 2.3a). It has $7DoF$, payload capacity of $10kg$, and weighs $18kg$ [LWR-4D, 2013].

The *Jaco* (Fig. 2.3b) robotic arm is developed by Kinova. It is light weight ($5kg$) with $6DoF$ which allow a high dexterity with compact size. This arm is made of carbon fibre structure and has ability to carry only $1.5kg$ payload at full extension $900mm$ [Jaco, 2013]. The *PowerBall* (Fig. 2.3d) is $6DoF$ robotic arm. It can carry $6kg$ payload and weighs $12.5kg$.

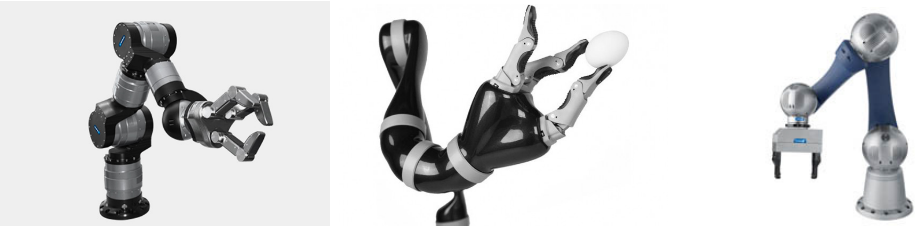

(a) LWA4D (b) *Jaco*™ (c) *PowerBall*®

Figure 2.3: Picture of (a) LWA4D (*Schunk*), (b) *Jaco*™ (Kinova) and (c) *PowerBall*® (Schunk)

Manufacturer	Schunk	Kinova	Schunk
Model name	*LWR4D*	*Jaco*	*PowerBall*
Arm extension	$1.11m$	$0.9m$	$0.610m$
Weight	$18kg$	$5kg$	$12.5kg$
Maximum payload at full reach	$10kg$	1.5	$6kg$
Degree of freedom	$7Dof$	$6Dof$	$6DoF$
Control mode	Position/torque	Position	Position/torque

Table 2.2: Summary of the key specifications of *LWR4D*, *Jaco* and *PowerBall*

2.1.1.4 Universal Robots

The main target market for Universal robots is the industrial automation. The $UR3$, $UR5$ and $UR10$ are their flagship robots (for key specifications see Table. 2.3). The $UR3$, $UR5$ and $UR10$ can carry payload of ($3kg$, $5kg$ and $10kg$) and weigh ($11kg$, $18.4kg$ and $28.9kg$) [UR, 2013], respectively. Similar to the LWR III, Universal Robots manipulators also come with heavy control unit as shown in Fig. 2.4.

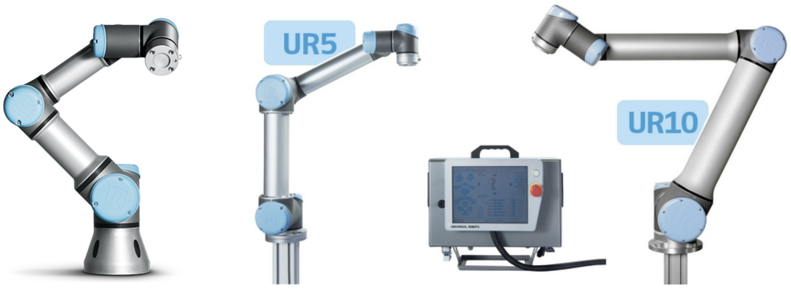

(a) UR3 (b) $UR5$ and $UR10$ with control unit

Figure 2.4: Universal Robots: UR3, UR5 and UR10

Manufacturer/reseller	Universal Robots		
Model name	$UR3$	$UR5$	$UR10$
Arm extension	$0.5m$	$0.850m$	$1.3m$
Weight	$11kg$	$18.4kg$	$28.9kg$
Maximum payload at full reach	$3kg$	5	$10kg$
Degree of freedom	$6Dof$	$6Dof$	$6DoF$
Control mode	Position/torque	Position	Position/torque

Table 2.3: Summary of the key specifications Universal Robots

2.1.1.5 HDT

The $MK1$ and $MK2$ robotic arms are designed by HDT (See Table 2.4 for specifications [HDT, 2013]). The $MK1$ can carry payload over $13.6kg$, $7DoF$ with ability to move $120degs/s$ for each joint and weighs only $6.6kg$. The $MK2$ is a dual arm system, it weighs $23kg$ and can lift a $50kg$ payload. Both robotic manipulators can be used either in position or torque control modes.

2.1.2 Hydraulically actuated manipulators

A brief description of today commercially available hydraulically actuated robotic arms is given below, along with their key specifications.

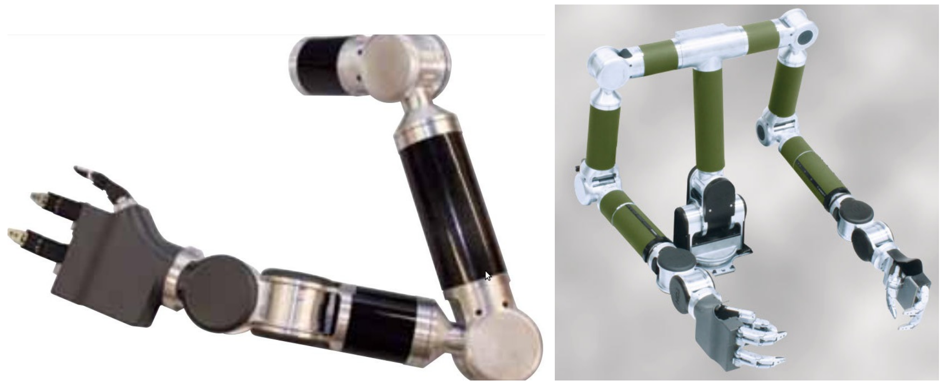
(a) (b)

Figure 2.5: Picture of HDT robotic arm: (a) $MK1$ and (b) $MK2$ Dual arm system

Manufacturer/reseller	HDT	HDT
Model name	$MK1$	$MK2$
Arm extenuation	$1.27m$	$1.27m$
Weight	$6.6kg$	$23kg$ (without external unit)
Maximum payload at full reach	$13.6kg$	$50kg$
Degree of freedom	$7Dof$	$7Dof$
Maximum joint speed	$120degs/s$	$120degs/s$
Control mode	Position/torque	Position/torque

Table 2.4: Summary of the key specifications HDT robotic arm

2.1.2.1 FMC Schilling Robotics

FMC Schilling Robotics provides a wide rang of underwater hydraulically actuated manipulators [FMC, 2015]. The Schilling manipulators are actuated with a combination of hydraulic cylinder and rotary motor at $300[bar]$ working pressure. The electronics are integrated within the manipulators structure. The TITAN series (Fig. 2.6(a)) have $7DoF$, payload capacity $112kg$ (full extension), weighs $100kg$ and position controlled. The mechanical structure is made of Titanium. The ATLAS 7R is a heavy-duty series of FMC robotics with lifting capacity of $250kg$ (full extension), $6Dof$ weighs $73kg$ and velocity controlled. The CONAN series has lifting capacity $159kg$ and weighs $107kg$ in the air. It has $7DoF$ and position control. The ORION series has $7DoF$, with payload lifting capacity of $68kg$, weighs $54kg$ and can be controlled in position or velocity control mode. A brief comparison of these manipulator is given in Table 2.5 and they are shown in Fig. 2.6.

2.1.2.2 KNR systems

The KNR system develops hydraulically actuated manipulator for under water (HYDRA-UW) and ground (HYDRA-MP) industries. The HYDRA-UW (Hydraulic Robot Arm - Underwater) series (Fig. 2.7(a)) has $6DoF$ with $50kg$ payload lifting capacity at $210[bar]$ pressure and position controlled. It is actuated by a combination of hydraulic cylinders and motors [HYDRA-UW, 2015]. The HYDRA-MP (Hydraulic Robot Arm - Manipulator) Fig. 2.7(b) is their latest manipulator. It has $6DoF$, weighs $90kg$

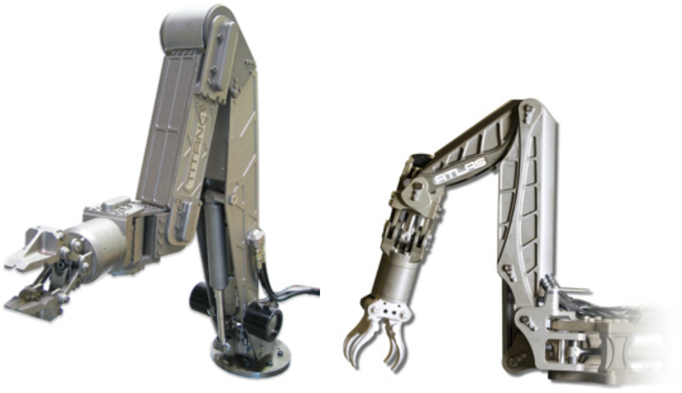

(a) TITAN 4 (b) ATLAS 7R

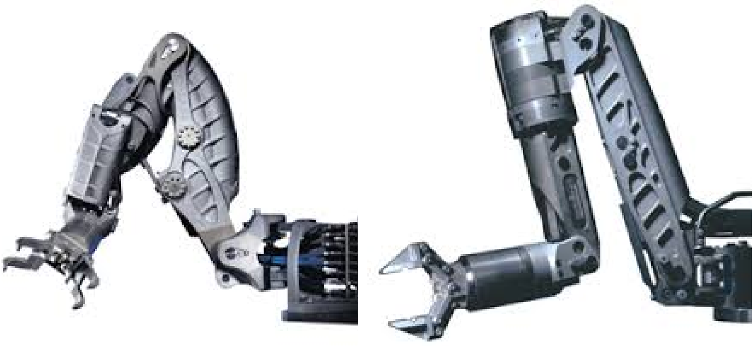

(c) CONAN 7P (d) ORION 7P/7R

Figure 2.6: FMC Schilling Robotics

Model	$TITAN4$	$ATLAS7R$	$CONAN7R$	$ORION7P/7R$
Arm extenuation	$1.922m$	$1.664m$	$1.806m$	$1.850m$
Weight in air	100 kg	73 kg	107 kg	54 kg
Weight in sea water	78 kg	50 kg	73 kg	38 kg
Maximum payload at full reach	122 kg	250 kg	159 kg	68 kg
DoF	7	6	7	7
Control mode	Position	Velocity	position	position/Velocity

Table 2.5: Schilling Robotic manipulator specifications

and can carry $70kg$. Each joint is actuated by similar hydraulic motor that provides $300Nm$ output torque at $210[bar]$. Recently, in one of their youtube videos, they have shown torque controlled capability for 1DoF hydraulic motor using pressure sensors [HYDRA-MP, 2015b]. Table. 2.6, summarizes the key specifications of KNR systems manipulators [HYDRA-MP, 2015a].

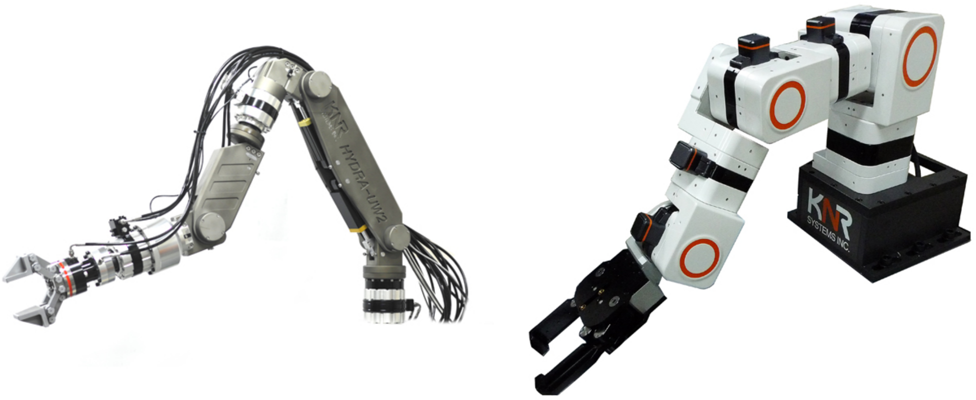

(a) HYDRA-UW2 (b) HYDRA-MP3

Figure 2.7: KNR systems: (a) HYDRA-UW Hydraulic Robot Arm - Under Water and (b) HYDRA-MP Hydraulic Robot Arm - Manipulator

Manufacturer/reseller	KNR Systems	
Model name	$HYDRA-UW2$	$HYDRA-MP3$
Arm extenuation	N/A	N/A
Weight	N/A	$90kg$
Maximum payload at full reach	$50kg$	$70kg$
Degree of freedom	$6Dof$	$6Dof$
Control mode	Position	Position/torque

Table 2.6: Summary of the key specifications KNR systems manipulators

2.1.2.3 HYDRO-LEK

The HYDRO-LEK system hydraulically actuated manipulator for under water and nuclear decommissioning industries. The CRA6 weighs $28kg$ with payload lifting capacity of $30kg$ at $140[bar]$ (Fig. 2.8(a)). It has $6DoF$ with maximum reach of $1.5m$ and only position controlled. The CRA6 is actuated by hydraulic cylinders [HLK-CRA6, 2015]. The HD6W manipulator arm has $6DoF$ actuated by a combination of hydraulic cylinder and rotary motor. It weighs $29kg$ and can carry $40kg$ payload at $140[bar]$ [HLK-HD6W, 2015]. Another manipulator developed by HYDRO-LEK is called $40500R$. It has $7DoF$ and was created to meet requirements of the medium range class RoVs. It can lift $150kg$ payload and weighs only $59kg$. It is only positioned controlled [HLK-40500R, 2015]. All manipulator by HYDRO-LEK are equipped with position sensors and all electronics is embedded inside manipulator body.

2.2 Multi-legged Mobile manipulator

The mobile manipulator belong to the floating base robotic family. Today, a vast variety of mobile manipulators exists. These robots are further categorized based on

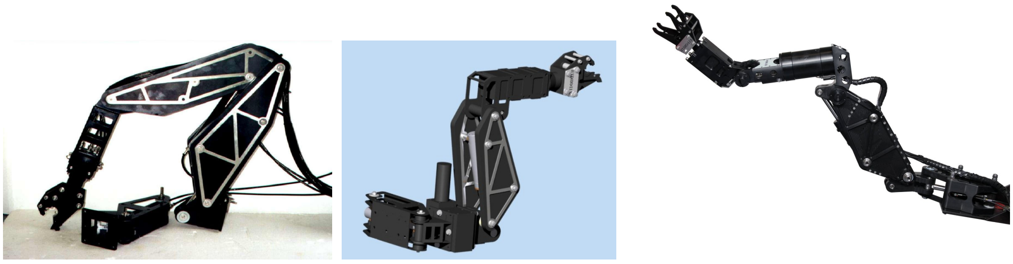
(a) HLK-CRA6 (b) HLK-HD6W (c) HLK-40500R

Figure 2.8: HYDRO-LEK

Table 2.7: HYDRO-LEK manipulator specifications

Model (HLK)	$CRA6$	$HD6W$	$40500R$
Arm extenuation	$1.5m$	$1.010m$	$1.5m$
Weight in Air	$28kg$	$29kg$	$59kg$
Weight in Seawater	$14.5kg$	$21kg$	$40kg$
Maximum payload at full reach	$32kg$	$40kg$	$150kg$
DoF	6	6	7
Control mode	Position	Position	position

their actuation system, mobile platform (wheels, tracks, or legs) and target mobility environment (ground, water, or space). The state-of-the-art of mobile manipulator will be limited to only multi-legged or centaur-like robots developed for the off-ground applications.

2.2.1 AQUAROBOT

The first known multi-legged mobile manipulator was AQUAROBOT. It was developed by a Japanese consortium of industry and universities starting from 1984 to 1993 as part of Advanced Robotics Technology research association (ART) project. The project was focus on development of robots for nuclear plants, undersea oil rigs and disaster prevention in refineries [HITACHI-ART, 2014]. The first field test of AQUAROBOT robot for underwater inspection was done in 1990 [Junichi et al., 1990]. This robot was developed to carry out underwater inspecting works. The AQUAROBOT has six legs to walk underwater at $50m$ depth. Each leg had $3DoF$ and they were electrically actuated by DC-motors. It was equipped with a TV camera and ultrasonic ranging device at the end of a manipulator mounted on the mobile platform as shown in Fig. 2.9(a).

2.2.2 HITACHI-ART Centaur

The first centaur-like robot was developed by HITACHI and ART as part of a same project mentioned above. They developed an electric centaur-like robot as shown in Fig. 2.9(b) [HITACHI-ART-CENTAUR, 1990]. This robot was developed to perform nuclear plants inspection and maintenance. There is no published work about robot design or specifications or tasks capabilities. It had four legs, two arms with hands, upper human-like torso and on board camera system.

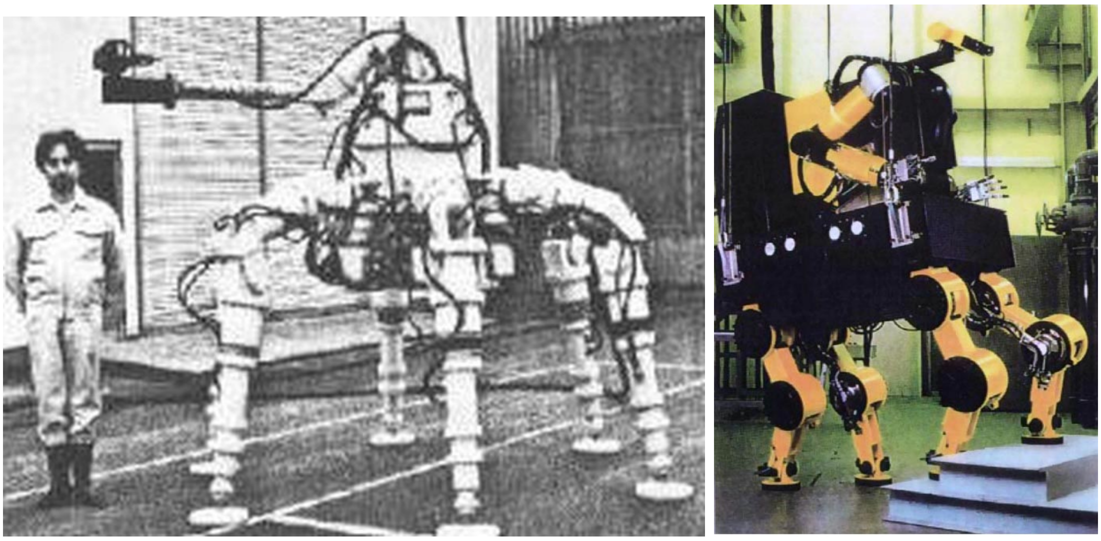

(a) AQUAROBOT (b) HITACHI-ART Centaur

Figure 2.9: HITACHI-ART

2.2.3 KIST-Centaur

A few years later after ART project, a similar robot developed by the Humanoid Robot Research Center and KIST Korea called it Centaur [Munsang et al., 1999]. This robot stood $1.8m$ tall and weighed $150kg$. The KIST-Centaur had overall 37 DoF. It had four $3DoF$ hydraulically actuated legs. Upper-body was electrically actuated by DC servo motors with reduction gear trains including harmonic drives. The upper-body looked alike half human with $25DoF$. It had a $2DoF$ torso, a neck with $2DoF$, two $7DoF$ of arms with two $3DoF$ hands and $1DoF$ mouth. It has an on board Li-Ion battery with 20 minutes of operation time. The KIST-Centaur equipped with force sensors at each wrist and head with stereo vision camera. On-board microphone enabled robot for voice recognition. All the servo control, wireless communication and power supply was embedded on to robot body. The robot was controlled either in teleoperation or autonomous mode. For teleoperation an exoskeleton of master arms was designed to control dual arm system.

2.2.4 Tsuda-Centaur

Tsuda et al. developed a centaur-like robot based on the humanoid robot [Tsuda et al., 2007]. They used two robots, one used as front body, legs and arm. From another robot, they only used lower body (legs) as a back of the centaur body attached with plastic plate as shown in Fig. 2.11. Tusda-Centaur overall consists of $34DoF$. It has four legs with $6DoF$, two arms with $4DoF$, $1DoF$ in its waist and $1DoF$ for head. All joints were actuated by electric RC servo motors. Tsuda et al. developed update software architecture and controller based on humanoid robot. They showed that upper and lower body motions can be controlled separately. They carried out experiments to evaluate their centaur-like robot motion capabilities. They showed that robot can walk smoothly by moving diagonal legs (similar to trotting). They tried different human-like motion developed for their humanoid robots. They concluded that human-like motion cannot directly apply to centaur-like robots and opened interesting future research [Tsuda et al., 2010].

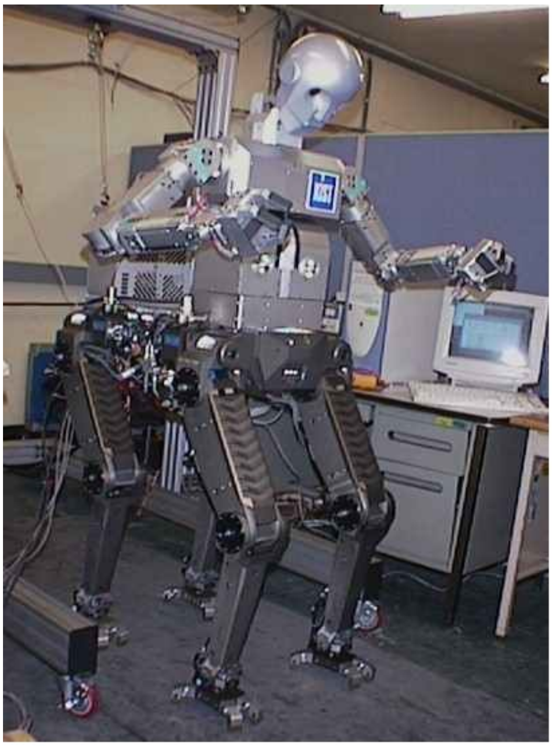

Figure 2.10: KIST-Centaur

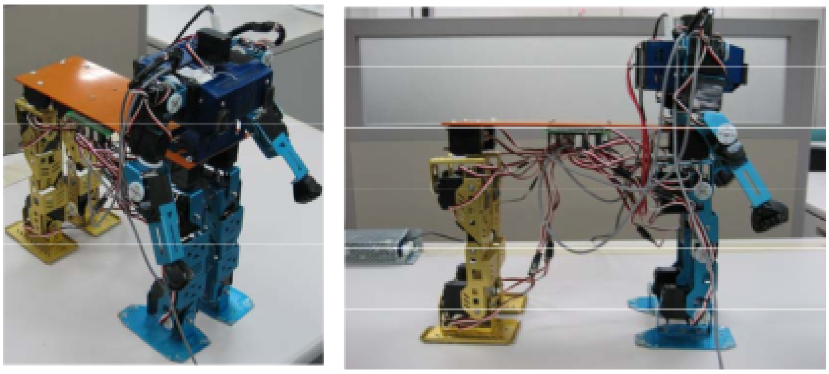

Figure 2.11: Tsuda-Centaur

2.2.5 BigDog

Recently, Boston Dynamics attached a custom build hydraulically actuated manipulator to BigDog, creating a multi-legged mobile manipulator. The designed manipulator consists of overall $8DoF$ including gripper as shown in Fig. 2.12a. The kinematic morphology and scale is similar to human arm. It has $3DoF$ in shoulder, $1DoF$ in elbow and $3DoF$ for wrist [Abe et al., 2013]. The manipulator is mounted in front of BigDog (Fig. 2.12b). It allows a workspace in front, laterally, below and above the robot. There is no published data available for manipulator weight, joint range-of-motion or torque. But, BigDog with arm have shown throwing $16.5kg$ cinder block in one of their youtube video (Fig. 2.12c). The goal of their work is to enable BigDog interact with objects in man-made environment and to use it for military applications. They have shown that using robot whole-body, legs and arm result in improved strength, velocity and

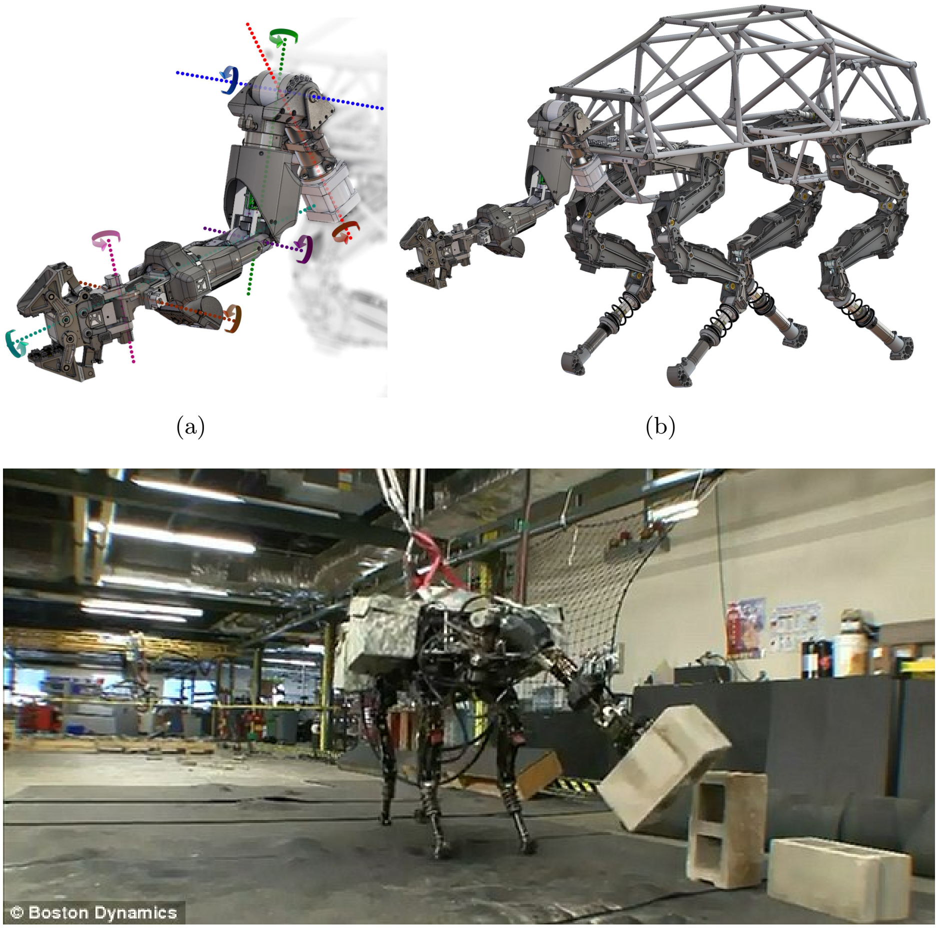

(a) (b)

(c) (replace with better picture!!)

Figure 2.12: BigDog

the workspace for the manipulator. For cinder block throwing task [Abe et al., 2013] provided off-line planned trajectories to the on-board trot and arm controllers for the execution the throwing task. The off-line trajectory generator plans the foot location and body forces while satisfying physical constraints. (Specifically, the center of pressure location, joint torques, speed and kinematic limits). The result is similar to a human athlete maximizes distance in the discus event by performing a precise sequence of choreographed steps.

2.2.6 WorkPartner

WorkPartner is the prototype of a service robot to work with humans in outdoor environment [Ylonen and Halme, 2002]. The mobile platform is based on a hybrid system. It combines legs and wheels locomotion to traverse over uneven terrain (Fig. 2.13). It has four legs equipped with wheels. Each leg has $3DoF$ joints and an active wheel. The upper-body consists of a $2DoF$ torso, two $3DoF$ arms and a camera & distance measuring laser pointer head with $2DoF$. The upper-body is mounted into the front of the robot mobile base that look like a centaur. It is electrically actuated and has an on-board power system a hybrid with batteries and 3Kw combustion engine. it weighs about $250kg$, including all mechanical components, actuation, power and computing

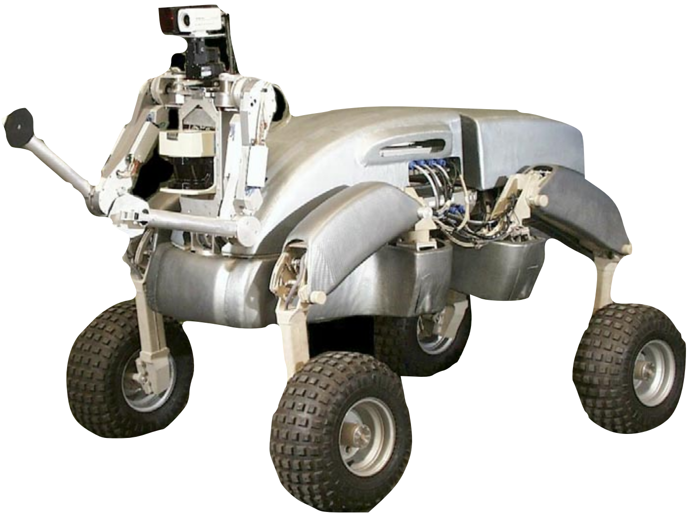

Figure 2.13: The WorkPartner robot, picture taken from [Ylonen and Halme, 2002]

systems. The target applications and work tasks for WorkPartner: garden work, cutting down of the forest, picking trashes, transferring of lightweight obstacles, environment mapping.

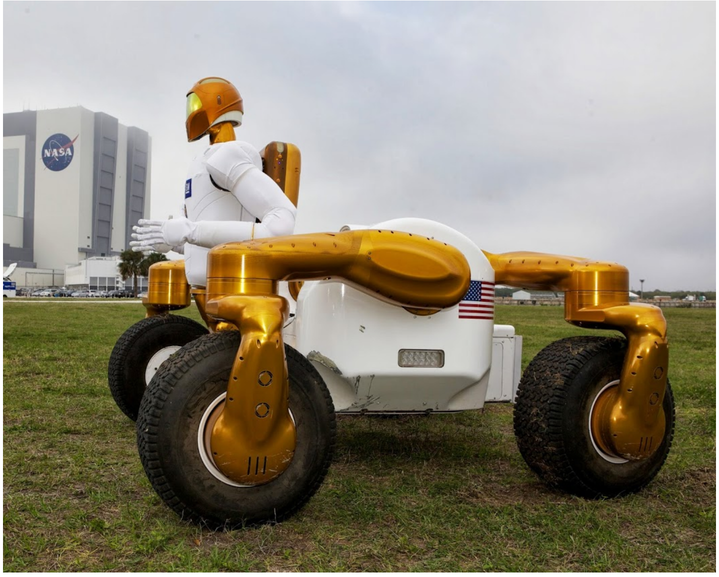

Figure 2.14: Robonaut2-Centaur2 by NASA

2.2.7 Robonaut2-Centaur2

Robonaut2 is extension of early designed called Robonaut1 [Bluethmann et al., 2003] by NASA. Later NASA and General Motors teamed up to develop Robonaut2 [iftler et al., 2011]. Robonaut 2, uses brushless DC motors, harmonic drive gear reductions, and electromagnetic fail-safe brakes and series elastic actuators as the building blocks. It has two torque controlled $7DoF$ robotic arms with $9kg$ payload lifting capacity at full extension and two hands with $12DoF$. Each arm joint actuator is integrated with custom planar torsion spring and 9 bit absolute angular position sensors to measure spring deflection. All arm joints and wrist are equipped Force/torque sensors. All the electronics is integrated into the upper-arm. The Robonaut2 has $3DoF$ head equipped with camera. The upper body is made of aluminum with steel and weighs $150kg$. The total height from waist to head is 1m and shoulder width is 0.8m. The Robonaut2 torso is attached to a rover with four legs and wheels as feet called Centaur-2 as shown in Fig. 2.14. The target applications and work tasks for this robot is to provide assistance to astronauts in space and perform exploration tasks.

2.2.8 Momaro

Momaro is an electrically actuated robot developed by Autonomous Intelligent Systems Group at the Computer Science Institute of University of Bonn, Germany. It has four legs with steerable wheels as feet. The wheels allow omnidirectional drive and legs adjust the height of the upper body. It has two $7DoF$ arms and two grippers. Each gripper has four individually controllable fingers with two joints each. Its upper body can rotate with respect to its base. It is equipped with on-board vision system and battery. Strictly speaking Momaro is not a multi-legged robot but an hybrid of legs and wheels mobile manipulator. During DARPA Robotics Challenge (DRC) in 2015, Memaro performed mobile manipulation task but never used legs for locomotion, it rather used only wheels as main source of mobility. It showed that using legs to change robot height results in enhanced workspace. Memaro teamed up with European universities including IIT to start a new European project called CENTAURO to build a centaur like robot for search and rescue missions.

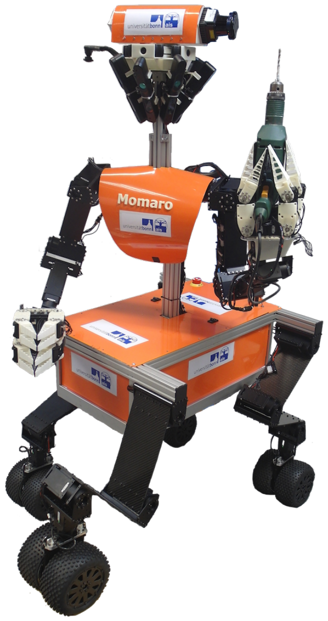

Figure 2.15: Momaro

2.2.9 Aero

Another centaur-like robot participated in DRC called Aero build by RT engineer from Japan [Aero, 2015]. It consists of a total $38DoF$. It has two arm with $7DoF$, 2 hands with $2DoF$, four $4DoF$ legs with wheels as feet and a torso with $3DoF$. Aero has on-board vision system located in neck with $3DoF$. It is electrically actuated powered by SEED solution actuators. Its total weight is $50kg$ and height is about $1.6m$. During DRC, it just used its wheels to traversed over rough terrain and couldn't finished the task.

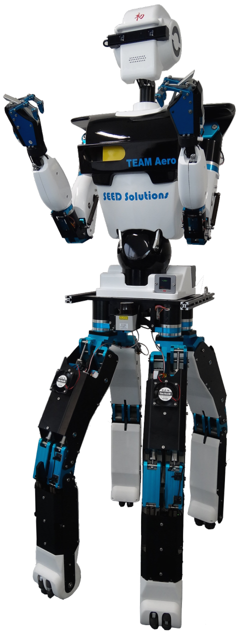

Figure 2.16: Aero

2.2.10 Grit

Grit also participated in DRC, it developed by small self-founded team of students, professors and professional engineers. It has four legs with wheels as feet, two arms and a torso resembles to centaur-like robot. It weighs $27kg$ and height is about $1.2m$. Grid is an electrically actuated robot. There is not published information about joint range-of-motion, speed, torque, and degrees of freedom.

2.2.11 TITAN-IX

[Hirose et al., 2005], developed a quadruped called TITAN-IX for demining missions. Each leg has three degree of freedom with specialized mechanism for their respective feet. The foot mechanism [Suganuma et al., 2003] allows each leg to change their end-effector tool e.g. gripper, sensor, or mower. TITAN-IX, has demonstrated three tasks at a time such as walking, exchanging the end-effector tool and ready for manipulation as shown in Fig. 2.18. The manipulation task is done remotely using a master gripper which teleo-perates the slave gripper on quadruped side. They have exhibited tool attachment/detachment, grasping and digging on single static leg teleoperated by a master gripper as shown in Fig. 2.19.

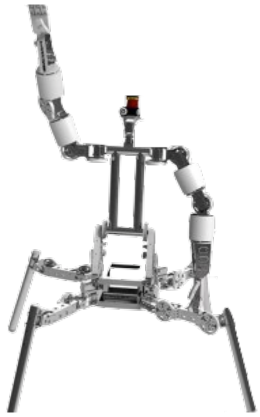

Figure 2.17: Grit

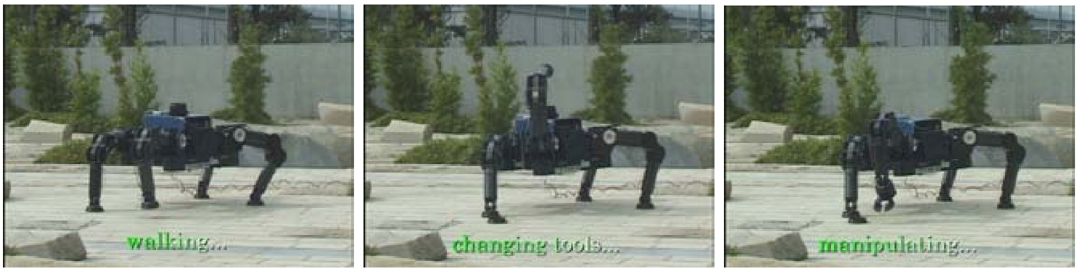

(a) (b) (c)

Figure 2.18: TITAN-IX demonstrating (a) walking, (b) changing tool and (c) manipulation task capabilities

2.2.12 LAURON-V

The LAURON-V is a hexapod robot designed by FZI Research Center for Information Technology, Germany. It has six electrically actuated legs with $4DoF$ in each leg. The LAURON-V designed to participate in search and rescue missions. It has weighs $42kg$ which includes on-board battery, computers, sensors and electronics and has $10kg$ payload capacity [Roennau et al., 2014]. It can stand on hind four legs by shifting CoM location between support polygon, leaving front two legs to use for single or dual manipulation task as shown in Fig. 2.20. Each front leg can carry a payload less then $1kg$. It only shows static manipulation without moving while holding an object. Recently, it has been upgraded with retractable gripper which allows to manipulate different objects with single leg.

2.2.13 RoboSimian

RoboSimian was develop by Jet Propulsion Laboratory JPL to participate in the DARPA Robotics Challenge (DRC) [Hebert et al., 2015]. The goal of RoboSimian development is to operate in a degraded human environment and perform tasks normally executed by a human. RoboSimian is one of its kind, it uses four limbs and hands to perform both mobility and manipulation. It has two active wheels on its body and two passive caster wheels on its limb to achieve passively stable posture. It has four identical limbs and each joint uses identical electric actuator. The actuator design consists of DC brushless motor directly drives a 160:1 harmonic drive, cross-roller bearings

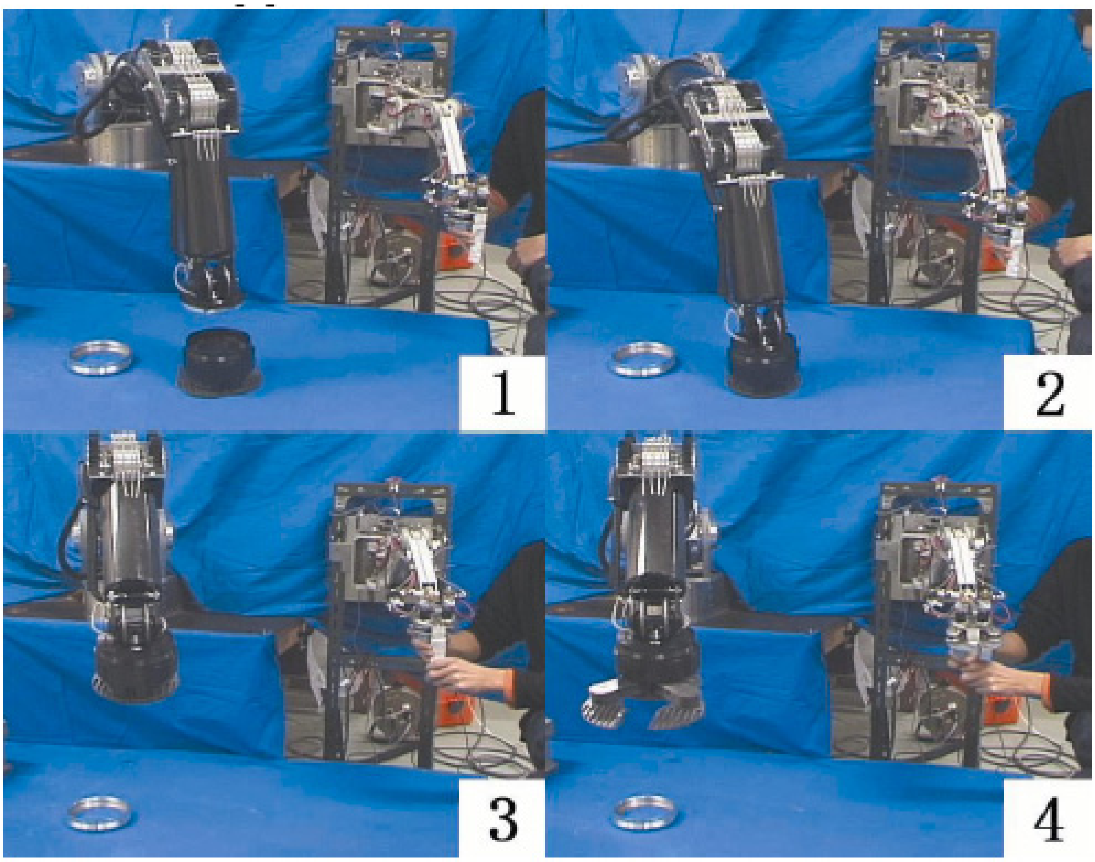

Figure 2.19: TITAN-IX, static leg manipulation demonstration

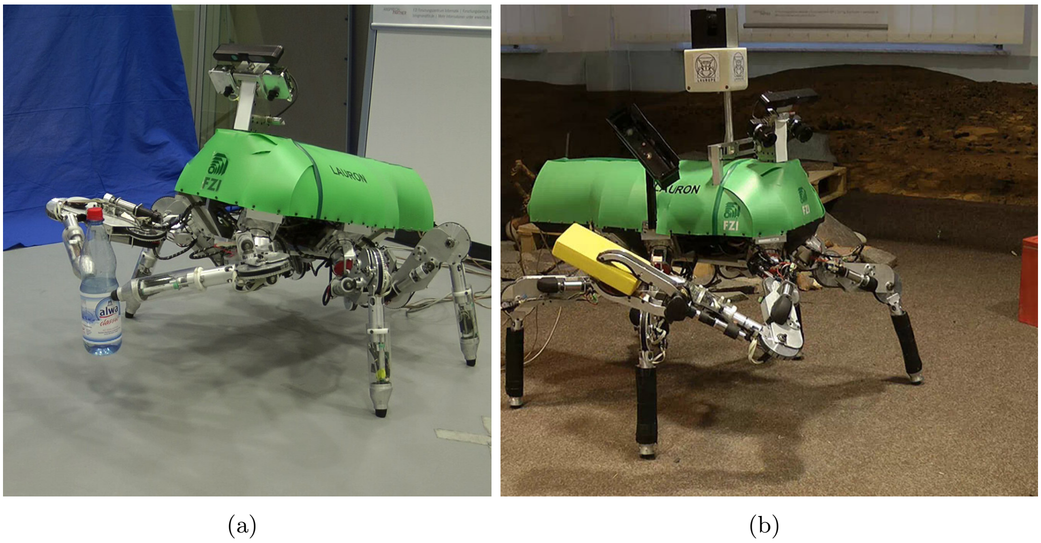

(a) (b)

Figure 2.20: LAURON V

and magnetic safety brake. It has two position sensors (a) an optical incremental encoder on the motor rotor and (b) a capacitive absolute position sensor on the actuator output. All the electronics, including safety, communication and microcontroller are integrated within actuator units. Each limb has $7DoF$ which is divided into 3 identical sub-assemblies so called elbow assembly and azimuth assembly actuator is connected to the body. An elbow assembly consists of two actuators integrated orthogonally with connecting structure. Repairing and field support during testing are easier as only a single actuator unit to swap out. End of each limb is equipped with a 6-axis force/torque sensor to detect the interaction with environment and serve as interface to end-effector.

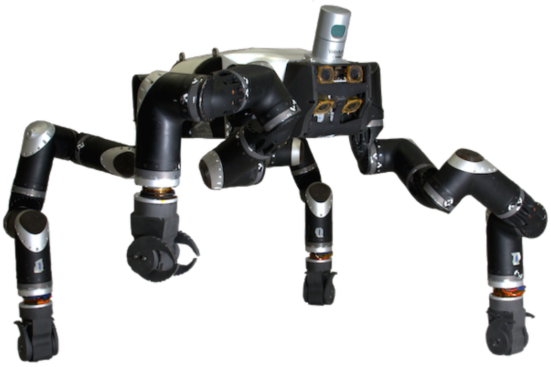

Figure 2.21: RoboSimian

2.2.14 Interact-Centaur

The Interact robot also called Interact-Centaur (Fig. 2.22) is developed by ESA's Telerobotics & Haptics Laboratory collaboration with TU Delft Robotics Institute. The robot consists of a four wheeled mobile platform to traverse over ground. To interact with environment or manipulate object, two $7DoF$ robotic LWR III with gripper are mounted in front of robot. To provide the visual information the robot has on-board camera system equipped with $6DoF$ pan-title unit and laser scanners.

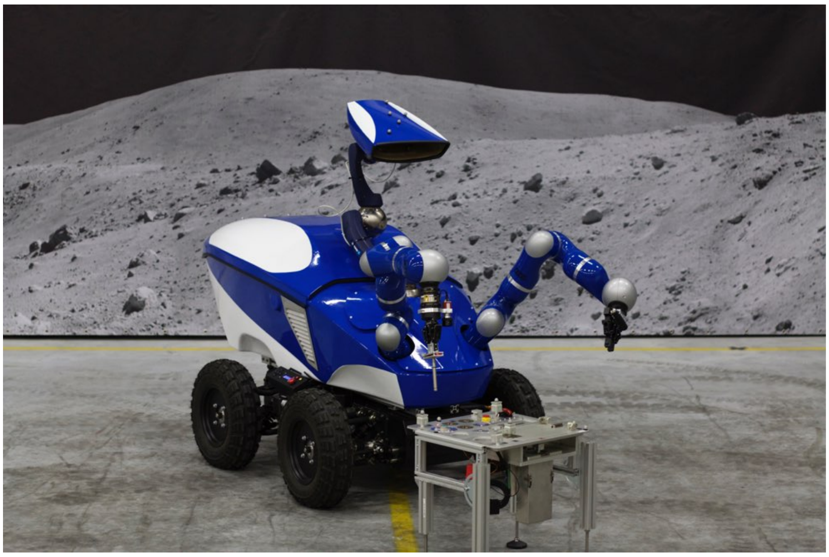

Figure 2.22: Interact Centaur

2.3 Torque Control

A fundamental requirement for the success of any robotic limb, which is designed to interact with its environment, is the ability to handle physical contact with its surrounding or the target objects. The pure position/velocity control is not sufficient for such application, where a robotic manipulator has to interact with objects or an environment without causing excessive forces, especially in the presence of a rigid environment. The interaction with environment or different objects is better dealt within the torque/force domain rather than only position control [Craig, 1989, Spong et al., 2006, Siciliano and Khatib, 2008].

Using torque control for each joint of any robotic limb has many advantages. The torque control allows to design various form of control framework, such as active compliance controller [Boaventura et al., 2013], active impedance controller [Boaventura et al., 2015], control of optimized contact forces [Rehman et al., 2016], or force-based virtual model control for robotic limb contact planning [Winkler et al., 2014]. Many other forms of model based control framework have torque as output. for instance, balancing the control frameworks of fully torque controlled mobile robots [Orin et al., 2013, Barasuol et al., 2013, Stephens and Atkeson, 2010].

Since the early days of such robotic limbs, torque control has been a subject of research and development [Whitney, 1987]. [Raibert and Craig, 1981]; first proposed was a hybrid position and force control approach for a robotic manipulator. They divided the task space into position-controlled and force-controlled subspaces. This hybrid control approach ignores the dynamic interaction between manipulator and the environment and results in poor tracking of position or force.

To address this issue, [Hogan, 1985] proposed impedance control. He highlighted that two physical systems must complement each other during dynamic interactions. For example, if one system is the robotic manipulator, then it must regulate its mechanical impedance to complement an admittance by the target environment and vice versa. The impedance controller establishes a dynamic relationship between the manipulator force at Cartesian space and motion constraints imposed by the environment. It generates required joint torques to achieve desired mass, damper and spring dynamic behaviour. An admittance controller performs opposite of impedance control. The impedance control has stable behaviour when a manipulator is interacting with a rigid environment but have poor performance in non contact tasks. On the other hand the admittance controlled manipulator have better performance when moving in free-space and is unstable if the manipulator is in contact with the environment.

[Ott et al., 2010] addressed this limitation and proposed a control framework to unify both impedance and admittance in order to exploit the complementary nature of each other. Their control framework constantly switched between impedance and admittance controllers. They analysed their control framework performance based on a single degree-of-freedom for a fixed based manipulator.

However, the performance of the impedance controller can be improved by using an inner torque control loop and direct-drive actuators. The cascade impedance and inner loop torque control have been implemented for a dual arm system with $3DoF$ torso fixed on ground by DLR [Ott et al., 2006]. Also in the field of mobile robots which are actuated by hydraulic (direct-drive) actuators such as the Sarcos humanoid [Cheng et al., 2007] and the hydraulically actuated quadruped robot HyQ [Boaventura et al., 2013, Focchi et al., 2013b, Boaventura et al., 2015]. In Chapter 5, we will present a model based inner torque loop cascade with outer compliance control loop control framework used in HyQ.

Chapter 3

Robotic Arm Specifications, Design Studies, and Hardware Selection

3.1 Robot Specifications

The first crucial step in the design process of any kind of robot or machine is to define target objectives and design prerequisites. It is not straight-forward to define initial physical specifications for a first prototype of a robot. Usually, the initial specifications are rather vague but follow logical reasoning based on the desired application or tasks. A strongly influenced parameter is the commercial availability of components. In the case of any robot, not only its performance specifications but also its physical and design specifications have to be defined.
The performance specifications of a robot can be defined based on the desired task and application. The physical specifications of a robot are difficult to specify but are essential in beginning the design process. A physical design of a robotic arm can be specified in terms of sufficient number of degrees of freedom (DoF), workspace, weights, actuation and expected payloads. It is important to define design specification as a rational guide line for the sizing of actuators, total weight and payload of a robot.

The rest of the section will define performance, physical and design specifications of the robot. Each specification is numbered with a tag **[SPx.x]** to refer to later in this chapter. The objectives and possible future applications of the robot are described in Chapter 1 (see Section 1.1 and 1.2).

3.1.1 Performance Specifications

The performance specifications are measured based on the tasks and applications that we desire to perform and achieve. In terms of performance I defined the following specifications:

- [**SP1.1**] Ability to open a door and walk through it. Its requires a robot to approach a door handle and manipulate it in order to open it and walk through.
- [**SP1.2**] Ability to push or pull an object, such as removal of an obstacle to clear a path for a human or robot itself, press a button to call a lift, or close a valve

to cut off the flow of a fluid in a disaster scenario (for further details see Section 1.1).

- **[SP1.3]** Ability to carry or grasp an object while walking or jumping (see Fig. 1.2).
- **[SP1.4]** Ability to provide assistance to the mobile platform, grab a railing or support bar while performing a manipulation task (Fig. 1.3(b)), or use side walls as extra contact points to walk on a slope or groove.
- **[SP1.5]** Ability to apply desired force while interacting with the environment or objects.
- **[SP1.6]** Ability to place the arms in a stowed position. This allows the mobile platform to pass through narrow passages without limiting locomotion ability (see Fig. **??**).

3.1.2 Physical Specifications

One of the crucial steps in the designing process is to define the physical specifications. Based on desired tasks specification, I defined the physical specifications as followed:

- **[SP2.1]** Each arm needs to have $6DoF$, which is the minimum requirement to define end-effector position and orientation in a 3D workspace.
- **[SP2.2]** Each arm has to be compact, light weight, fast and able to carry a heavy object.
- **[SP2.3]** Each arm should be fully integrated without an external control unit.
- **[SP2.4]** The dual arm system should be modular in design, e.g, easy mount-dismount without or having a slight modification to exit the mobile robot.
- **[SP2.5]** The dual arm system should not make it difficult for the quadruped robot to navigate through narrow spaces.
- **[SP2.6]** The robotic arm(s) joint range-of-motion and link lengths should be able to reach targeted objects in front, below, or above the robot torso and be able to manipulate. The should roughly equal maximum leg length of the base robot.
- **[SP2.7]** The robotic arms needs to be equipped with position and force/torque sensors. These sensors will enable the robot to be force/torque controlled, which is an important feature as mentioned earlier in Section 2.3.
- **[SP2.8]** The design of an arm should be flexible to mirror left and right arm configurations.

Table 3.1 summarizes the above-mentioned physical specifications required for the design of a robotic arm.

The physical dimension, total weight, and power-to-weight ratio of any robot is strongly influenced by the commercial availability of actuators and mechanical components. I chose to have each joint hydraulically actuated and torque-controlled. Hydraulic actuators are well known for their higher power-to-weight ratio and robustness when

Specification	**Description**	**Tag**
Degree of freedom	$6Dof$	**[SP2.1]**
Arm full extension	$0.6 - 0.7m$	**[SP2.2]**, **[SP2.6]**
Maximum payload	$10kg$	**[SP2.2]**
Weight	$10kg$	**[SP2.2]**
Actuation system	Hydraulics	**[SP2.2]**,**[SP2.4]**
Sensors on each DoF	position and force/torque	**[SP2.7]**
Control mode	Position/torque	**[SP2.7]**

Table 3.1: Summary of desired physical specifications for each arm

coping with high force peak impacts. This feature becomes-essential while interacting with the environment ([**SP1.2**], [**SP1.3**], [**SP1.4**]). Another advantage of using hydraulics is that HyQ already has an hydraulic supply ([**SP2.4**]). Along the same lines, it is essential to have a torque controlled robot because due to the physical nature of the impacts, they are better dealt with in the torque domain [Boaventura et al., 2012b].

Next, I will set a design guide line to estimate required joint range-of-motion, velocity, and torque to select actuator and mechanical components.

3.1.3 Design Specifications

As mentioned earlier, the commercial availability of actuators is a strong parameter which affects robot total size, weight, and lifting capacity. The sizing of an actuator is the challenge for a designer. Selecting under-sized actuators can lead to serious limitations of robot performance which the could increase the cost and time of the design process. Usually the sizing of actuators is done by (1) design optimization based on earlier experience with similar robots [Tsagarakis et al., 2013, Khan et al., 2013, Parmiggiani et al., 2012]; (2) availability of specifically designed actuators for the target robot; (3) static torque calculation; (4) based on specific dynamic performance or loading criteria [Bowling and Khatib, 2002, Thomas et al., 1985]; (5) simulating a simplified robot model and tasks
[Chatzakos and Papadopoulos, 2008, Semini et al., 2012]; (6) simulating one or several representative task with a full robot dynamic model (using rigid body dynamics) [Kaneko et al., 2002, Lohmeier et al., 2006a, Lohmeier et al., 2006b, Dallali et al., 2013]. For the sizing of actuators and selection of mechanical components for dual arm system design, we performed simulations of several representative tasks with a full robot dynamic model. The representative tasks are designed to overlap with tasks specified in Section 3.1.1. The simulation results provide an estimation of required joint range-of-motion, velocity, and torque. Although these simulations give an initial estimate for the required design parameters, there are some limitations in this method, which are discussed in Section 3.4.

The next section continue to explain system modeling to a simulate robot. First, I defined the kinematic structure and dynamic model of a centaur-like robot. Second, simulated representative tasks for workspace analysis and design parameter estimation results. Finally, I selected hardware and translated the simulation results to actuator space.

3.2 System Modeling

The system modeling is required to develop a mathematical model that describes the kinematics and dynamics of the system. It is useful to estimate design parameters such as joint range-of-motion, velocity and torque. System modeling is also useful for implementation of model-based control strategies, motions and trajectories planning. In order to simulate centaur-like robot kinematic and dynamic simulation, the system modeling procedure is divided into the following steps:

1. Develop the kinematic structure of a dual arm system with a mobile platform to simulate a centaur-like robot.

2. Develop the dynamic model to simulate a centaur-like robot.

3.2.1 Kinematics Modeling

The kinematic model is required to describe the motion of the robot without considering how forces and torque affect the motion. This section presents an overview of the mobile platform (e.g, HyQ) and kinematic model of the manipulator based on specifications defined above, and shows how they are integrated.

3.2.1.1 The Mobile Platform Kinematics

HyQ is a fully torque-controlled hydraulically actuated quadruped robot (3.1(a)) [Semini et al., 2011]. It has 12 Degree-of-Freedom. HyQ weighs $80kg$, is roughly $1m$ long, and has a leg length of $0.78m$ (fully stretched). Each leg has three degrees of freedom: the hip abduction/adduction (HAA), and flexion/extension (HFE), and the knee flexion/extension (KFE). The legs are actuated by a combination of hydraulic motors and cylinders. In addition, HyQ has an on-board *inertial measurement unit* (IMU), position, torque/force sensors, and an on-board 4-core computer. HyQ kinematic structure is shown in Fig. 3.1(b). Table. 3.2 summarizes the specifications of HyQ and each leg's segment length and weight, along with overall robot dimension and total weight [Semini, 2010, Semini et al., 2011].

3.2.1.2 The Manipulator Kinematics

According to [**SP2.1**], the kinematic structure of each arm is defined as a chain of six revolute joints. I chose to have six DoF in the arm, which is a minimum requirement to define the position/orientation in a 3D space. This choice also have an advantage of less mechanical and computational complexity, at a cost of reduced manipulator dexterity. Each joint is grouped as $3DoF$ for the shoulder, $1DoF$ for the elbow (upper arm) and $2DoF$ at the wrist (lower arm). Inspired by human arm anatomy, each actuated joint is label as follows: Shoulder Adduction/Abduction (SAA), Shoulder Flexion/Extension (SFE), Humerus Rotation (HR), Elbow Flexion/Extension (EFE), Wrist Rotation (WR), and Wrist Flexion/Extension (WFE), as shown in Fig. 3.2. The lack of a kinematic redundancy reduces the mechanical complexity, cost, and weight of the robotic arms at the expense of a reduction in arm dexterity. Based on the specification [**SP2.6**], I assumed that the overall manipulator length is roughly equal to maximum leg length of the mobile platform. For the initial simulation, I considered that each link has a

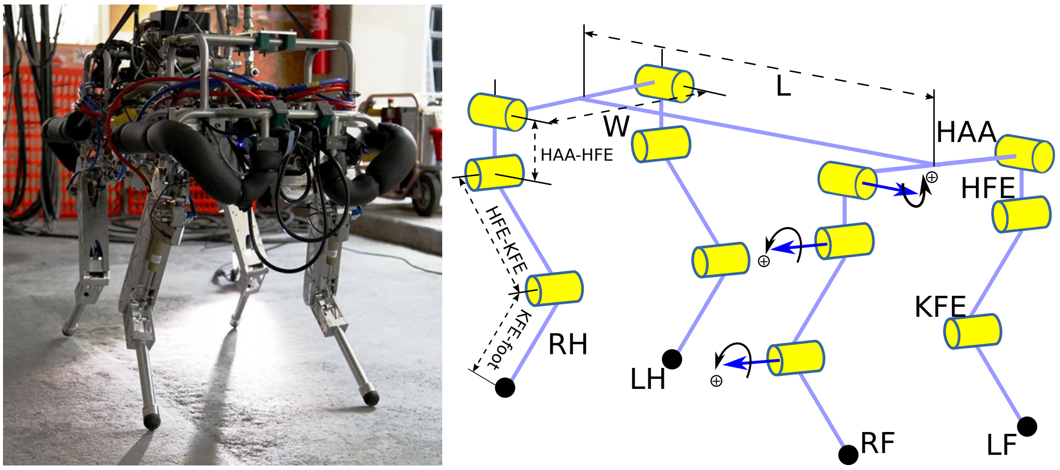
L
W
HAA-HFE
HFE-KFE
KFE-foot
HAA
HFE
KFE
RH
LH
RF
LF

(a) HyQ: Hydraulically actuated Quadruped (picture credit: A. Abrusci (IIT)).

(b) HyQ kinematic structure

Figure 3.1: (a) HyQ: Hydraulically actuated Quadruped robot (b) HyQ kinematic structure: hip Adduction/Abduction (HAA), Hip Flexion/Extension (HFE) and Knee Flexion/Extension (KFE), all the leg joint angles are shown in default standing position. Where, Left Front (LF), Right Front (RF), Left Hind (LH), Right Hind (RH). The L is the distance between the HFE axis of the hind legs and the front legs and W is the HAA to HAA distance on left and right side of HyQ.

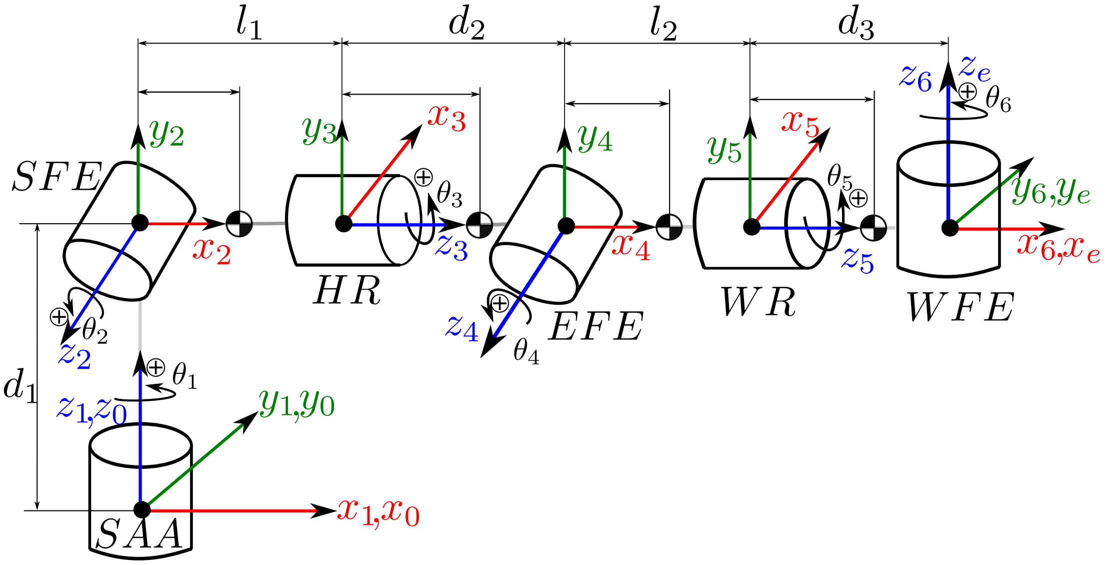
l_1
d_2
l_2
d_3
SFE
y_2
x_2
z_2
θ_2
HR
y_3
x_3
z_3
θ_3
EFE
y_4
x_4
z_4
θ_4
WR
y_5
x_5
z_5
θ_5
WFE
z_6,z_e
θ_6
y_6,y_e
x_6,x_e
d_1
θ_1
z_1,z_0
y_1,y_0
x_1,x_0
SAA

Figure 3.2: The manipulator kinematic structure: Shoulder Adduction/Abduction (SAA), Shoulder Flexion/Extension (SFE), Humerus Rotation (HR), Elbow Flexion/Extension (EFE), Wrist Rotation (WR), Wrist Flexion/Extension (WFE), all the arm joint angles are shown at zero configuration. Where d_1,l_1,d_2,l_2 and d_3 are link lengths

length of $0.175[m]$ and weighs $2kg$. Table. 3.3, summarizes each assumed manipulator link's length and weight, along with overall simulated robot dimension and total weight.

Specification Overview	Description
DoF	12
HAA actuators	double-vane rotary hydraulic actuators
HFE/KFE actuators	asymmetric hydraulic cylinders
HAA joint torque (max)	120Nm at 200[bar]
HFE/KFE joints torque	181Nm (peak torque) at 200[bar]
joint motion range	90° (HAA), 120° (HFE, KFE)
position sensors	position 80000cpr in all joints
torque sensors	custom torque (HAA), loadcell (HFE, KFE)
onboard computer	Pentium i5 with real-time Linux
controller rate	1kHz

leg segment/part	link length	mass
HAA-HFE	0.08m	2.9kg
HFE-KFE	0.35m	2.6kg
KFE-foot	0.35m	0.8kg
Total leg	0.78m	6.3kg
overall dimension	1.0mx0.5mx0.98 (LxWxH)	
total weight	80kg	

Table 3.2: HyQ: specification overview and leg segment/part lengths and masses.

Arm segment/part	link length	mass
SAA-SFE (d_1)	0.175m	2kg
SFE-HR (l_1)	0.175m	2kg
HR-EFE (d_2)	0.175m	2kg
EFE-WR (l_2)	0.175m	2kg
WR-WFE (d_3)	0.175m	2kg
overall dimension	0.7 X 0.075 X 0.175 (LxWxH) [m]	
total weight	10kg	

Table 3.3: Simulated robotic arm(s): link length and weight, along with the overall robotic arm dimension and total weight

3.2.1.3 The Centaur-like Robot Kinematic

The centaur-like robot has 6 kinematic branches: 4 legs and 2 arms, thus $n_r = n_{legs} + n_{arms}$. In the total, it has $(n_r + n_b)DoF$, where n_r is total number of active or actuated DoF and $n_b = 6$ floating-base DoF as shown in Fig. 3.3. Where the position and orientation of both arm base links are unknown design parameters, such as the distance between HyQ body frame B and manipulators, base links are defined by (d_x) and $(d_y = L_{oy} + R_{oy})$, along (x_o, y_o)-axis, as shown in Fig. 3.3(a) and (b). Also, the angle between (x_o, y_o)-axis of body frame B and manipulator base links are defined as θ_1 and θ_2, respectively, as shown in Fig. 3.3 (b) and (c). In Section 3.3.1 I will explains in details, how I selected these shoulder attachment parameters (SDP) to create a centaur-like robot, defined as:

$$SDP = [\theta_1, \theta_2, d_x, d_y] \tag{3.1}$$

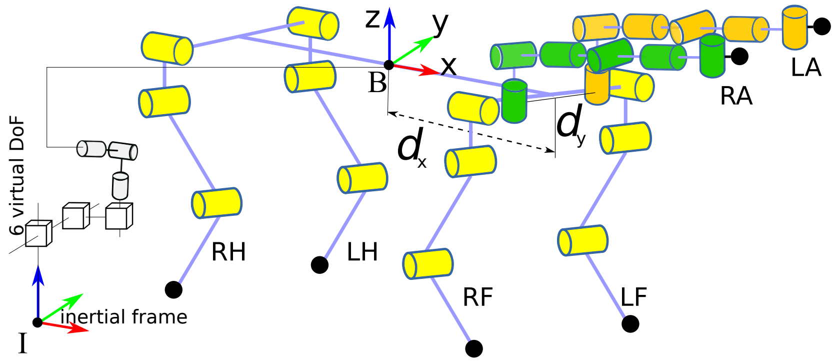

(a) Centur-like robot kinematic structure

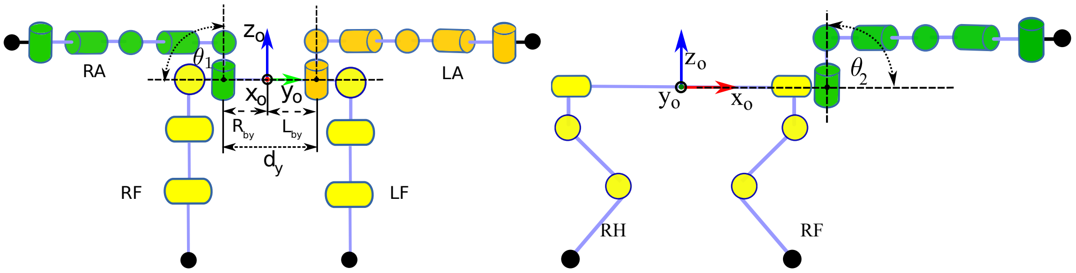

(b) Centur-like robot front view: arms base joints 90 degree rotated with respect to configuration shown in Fig. 3.3a and rest of the joints in default position

(c) Centur-like robot Side view

Figure 3.3: Centaur-like robot kinematic model: right arm (RA), left arm (LA), left front leg (RF), right front leg (RF), left hind leg (LH), right hind leg (RH)

3.2.2 Dynamics Modeling

The centaur-like robot belongs to the class of floating base robots. The robot is not rigidly attached to the ground but can freely move anywhere in the space. It is necessary to describe the complete dynamics of the system with respect to an inertial frame. To this end, system joint configuration is described as:

$$q = \begin{pmatrix} x_{n_b} \\ q_{n_r} \end{pmatrix} \tag{3.2}$$

where $q_{n_r} \in \mathbb{R}^{n_r}$, is joint configuration of the centaur-like robot with n_r actuated joints, x_b is the position ($\in \mathbb{R}^3$) and orientation ($\in SE(3)$) of the coordinate system attached to robot body B and measured with respect to an inertial frame I. The equation of motion with respect to an inertial frame is given by:

$$M(q)\ddot{q} + h(q, \dot{q}) = S^T \tau \tag{3.3}$$

where $M(q) \in \mathbb{R}^{n_r+n_b \times n_r+n_b}$, it the mass matrix including floating base, $h(q, \dot{q}) \in \mathbb{R}^{n_r+n_b}$, force vector as sum of its centripetal, Coriolis, and gravity terms, $S = [0_{n_r \times n_b}\ I_{n_r \times n_r}]$, joint selection matrix separate the actuated joint from un-actuated floating base, and $\tau \in \mathbb{R}^{n_r}$ is the actuated joint torques vector.

3.3 Simulation Based Design Study of Dual-arm System for Centaur-like Robot

To build and simulate the kinematic model of the centaur-like robot, I used Matlab and ROS[1]. The goal of kinematic simulation is to analyse the shared vs overall workspace based on performance index to select optimized attachment of dual arm system with quadruped, joint range-of-motion etc. On the other hand, the dynamical model of the centaur-like robot, I used *RobCoGen* [Frigerio et al., 2012], a model based code generator to provide kinematics and dynamics of articulated robots based on [Featherstone, 2007]. Given the kinematic tree of the robot (see Section 3.2) and its inertia properties, RobCoGen automatically generates an optimized C++ implementation of forward/inverse dynamics and forward kinematic transforms targeting different software platforms (e.g. C++, Matlab). The parameter for HyQ are taken from the CAD model as summarized in Table. 3.2. To calculate inertia properties for the robotic arms simulation (considering the design specifications given in Section 3.1.3), I selected each link as represented by an aluminium cylindrical link of mass $2kg$, length $0.175[m]$, diameter $0.075[m]$, with material density of $2700[kg/m^3]$ as summarized in Table. 3.3. To simulate dynamical tasks, I used *SL*. The *SL* is a robotic simulation engine and real time motor control package by Stefan Schaal [Schaal, 2006]. It provides a possibility to implement the robot behaviour and motor control in two different blocks. These two blocks interacts with two real time processes via shared memory called task servo and motor servo, respectively. The motor servo takes I/O information from the robot which can be used in two modes (a) simulator or (b) real hardware. On other hand, the task servo is unaware of the current mode of execution in motor servo. This feature allows to simulate the robot behaviours in a simulation environment and then later on the real robot, without any modification in task servo.

In next section I will present kinematic analysis of a dual-arm system based on physical specifications, workspace analysis, and performance indices to select design parameters such as shoulder attachment parameters (3.1) and mechanical limits for each arm joint range-of-motion.

3.3.1 Workspace Analysis of Manipulator(s)

A workspace of a robotic arm is defined as the set of points in space reached by an end-effector. The workspace shape depends upon kinematic structure, number of DoF, link length, and joint range-of-motion. A full workspace of a robotic arm with a spherical shoulder joint is a sphere. Similarly, the workspace of a dual arm system results in two spheres, whose centres are apart with distance d_y:

$$d_y = L_{by} + R_{by} \tag{3.4}$$

where L_{by} and R_{by} are the distance of the left and right shoulders, attachment along y-axis of a mobile platform body frame, respectively as shown in Fig. 3.3(b). Whereas in Fig. 3.4, I provide a 3D representation of a dual arm system workspace (under the assumption that $d_x = \frac{L}{2}$, $d_y = W$, $\theta_1 = 0[deg]$ and $\theta_2 = 0[deg]$), and where L is the distance between the HFE axis of the hind legs and the front legs and W is the HAA to HAA distance on left and right side of the base robot as shown in Fig 3.1(b). Using a random generator, I randomly generated joint angles (without mechanical limits) as input to the dual arm forward kinematics to calculate end-effector Cartesian position.

---

[1] http://www.ros.org/

The red and blue point clouds represent, right and left arm end-effector Cartesian positions. It is essential for the design process to determine the overall and the common workspace of the dual arm system, its boundaries, and singularity values.

In the next section I will describe the relation between overall and common workspace of the dual-arm system, and how distance between both shoulders d_y, and orientation e.g. θ_1 and θ_2 affects overall and common workspace. For sake of simplicity, I will consider that $\theta_1 = 0$ and $\theta_2 = 0$ until otherwise specified.

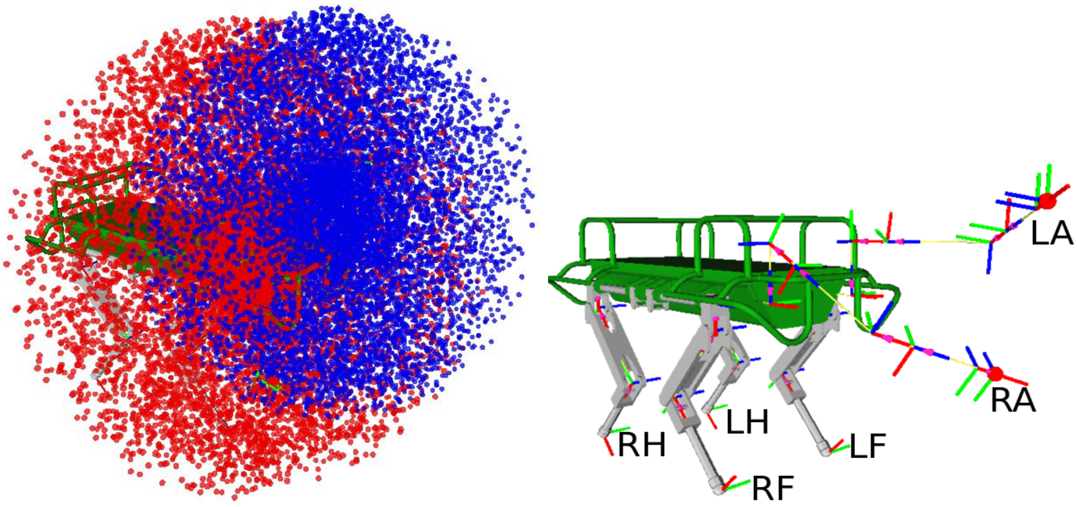

(a) Static view with end-effector position as point clouds.

(b) Static view without end-effector position's point cloud.

Figure 3.4: The 3D representation of Centaur-like robot arms workspace without mechanical joint limits, under assumption that $d_x = \frac{L}{2}$, $d_y = W$, $\theta_1 = 0[deg]$ and $\theta_2 = 0[deg]$. Where L is the distance between the HFE axis of the hind legs and the front legs and W is the HAA to HAA distance on left and right side of base robot. Each manipulator end-effector position is calculated using forward kinematics. The red and blue point cloud represent right and left arms end-effector position within their workspace, using randomly generated joint angles without mechanical limits. The workspace obviously contains also all the white spaces between the points.

3.3.1.1 Overall and Common Workspace of a Dual Arm System

To determine overall and common workspace, consider Fig. 3.5, where a blue (sold-line) and a red (dashed-line) circle represent the left and the right spherical workspace shown as a cut through in the xy-plane of the mobile platform body frame B. Where, L_1 and L_2 are the upper and lower links length of each manipulator, r is the radius of each circle, h is the distance between the intersection of each circle and the line connecting the origin of both manipulator base links. The left and right manipulator base links are located at O_l and O_r, respectively. The distance d_y between the origin of both manipulators is an important design parameter as it maximizes or minimizes the common and the overall workspace. As shown in Fig. 3.6, if $d_y = 0$ shared workspace will be maximized at the cost of minimized overall workspace. Similarly, if $d_y \geq 2r$, then overall workspace will be maximized without common workspace between both manipulators. The shared versus overall workspace of two given examples in Fig. 3.5, where if $d_y = W$ and $d_y = W/2$, is also shown in Fig. 3.6. Therefore, I have to select

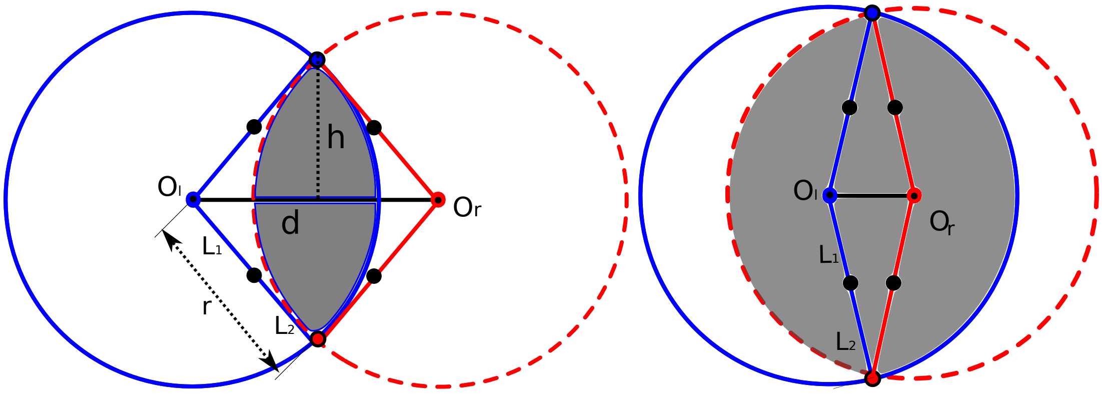

(a) If $d_y = W$ (b) If $d_y = \frac{W}{2}$

Figure 3.5: Common vs overall workspace: Blue (solid) and red (dashed) circles representation of left and right spherical workspace cut through in xy-plan of the mobile platform body frame B. The grey shaded area represents common workspace for both manipulators. Where, L_1 and L_2 are upper and lower links length of each manipulator, r is radius of each circle, h is distance between intersection of each circle and line connecting origin on each manipulator base link. O_l and O_r are origin of left and right manipulator base link with respect to mobile platform body frame B.

optimized value of the design parameter "d_y" in order to achieve the optimal common and overall workspace. For sake of simplicity, I will use $d_x = 0.5[m]$ unless otherwise specified.

3.3.2 Performance Indices Based Analysis of the Workspace

The performance indices are metrics that measure and assess the different performance characteristics of a robotic arm within its workspace. In the past, performance indices for the robotic arm have been classified based on their scope (local or global), performance of the robotic arm in terms of kinematic and dynamics, or application [Patel and Sobh, 2014].

The local indices are performance metrics of a manipulator which is limited to a particular posture or position of manipulator within its workspace. The value of local indices varies from point to point or posture to posture. The global indices are used to compare the performance of two manipulator that perform same tasks. The global indices have been formulated based in local indices and gives a single value for a given workspace. Higher local indices valve do not guarantee a higher global indices value and the contrary is also true [Kucuk and Bingul, 2005]. In the remaining sections, I will consider both local and global performance indices for workspace analysis of both manipulators. First, a local performance index (considering both individual robotic arms as decoupled from each other) that is called Manipulability Index. Second, a global performance index which couples together both individual arms, called Dual-arm Manipulability.

3.3.2.1 Manipulability Index

[Yoshikawa, 1985] proposed a manipulability index number as kinematic performance for a robotic arm. The Yoshikawa manipulability index is the most widely accepted and used measure for kinematic manipulability. It based on the Jacobian matrix. In case

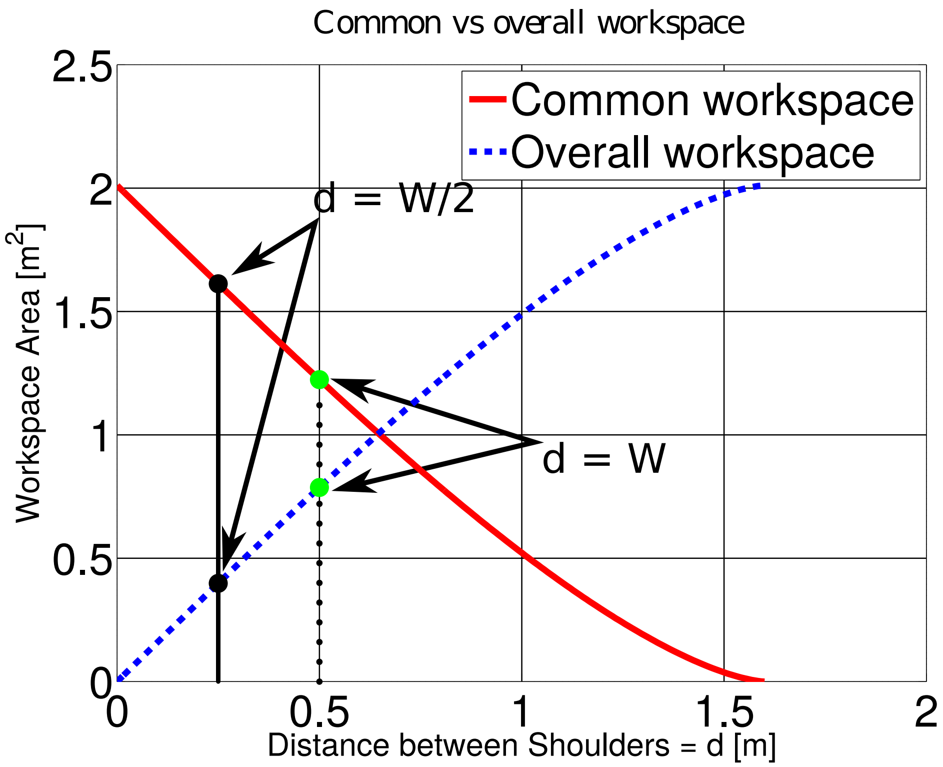

Figure 3.6: Common vs overall workspace relation: Common vs Overall workspace based on d varying between range $(0-2r)$. Where W is width of mobile robot, in case of HyQ, $W = 0.5[m]$. The solid red line represents common overlapped area and the blue dash line represents overall workspace.

of non-redundant manipulators the Jacobian is a square matrix and the manipulability index is equal to the absolute of the determinant of the Jacobian.

$$\xi = |det(J)| \tag{3.5}$$

The manipulability index based on the Jacobian matrix results strongly depend on the choice of physical units used for calculation. It is important to know the maximum manipulability index in the workspace in order to appreciate the manipulability index at different points. [Lenarčič and Thomas, 2002], introduced a concept of the normalized manipulability index in order to make the manipulability index a bounded parameter (independent of physical scale and units) and defined as,

$$\xi_n = \frac{\xi_i}{max(\xi_1\xi_2\xi_3..\xi_n)} \tag{3.6}$$

where ξ_i is manipulability index at a given point and $max(\xi_1\xi_2\xi_3..\xi_n)$ is maximum manipulability index for the whole workspace. I calculated the normalized manipulability index ξ_n for the each manipulator (described and developed in this thesis) in full 3D workspace without mechanical joint limits as shown in Fig. 3.7(a). The ξ_n value is represented as red ($\xi_{n_i} > 0.66$), green ($0.66 \leq \xi_{n_i} > 0.33$), blue ($0.33 \leq \xi_{n_i} > 0.001$) and black ($\xi_{n_i} \leq 0.001$) at i^{th} point in workspace. The cluster of black points on the top, middle and bottom of manipulators base links represents singularity positions.

I used normalized manipulator index to select mechanical joint limits for the individual arm, I excluded all end-effector positions which are at the singularity and overlapped with base robot legs and torso by taking into account [**SP1.6**]. Figure 3.8 shows the normalized manipulability index within mechanical joint limits, which are summarized in Table. 3.4.

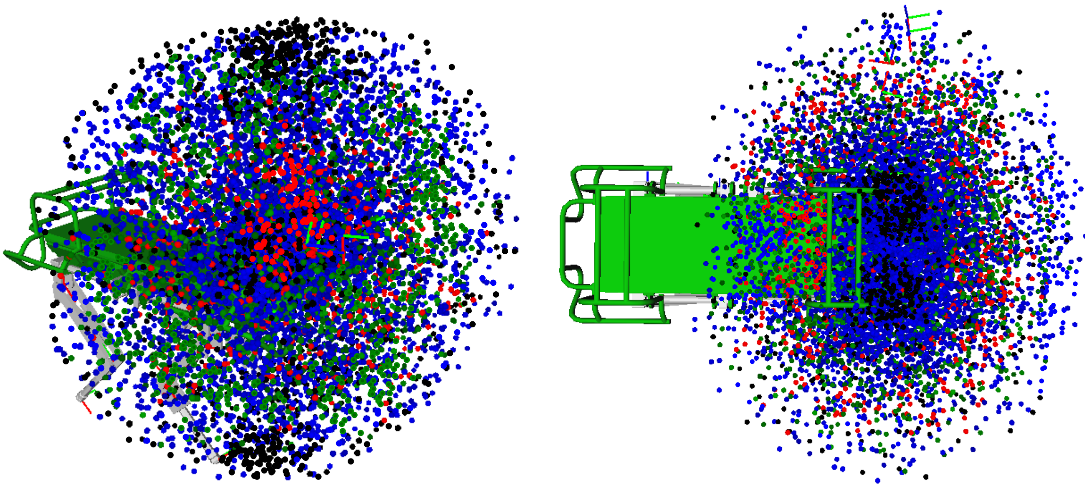

(a) Full workspace without mechanical joint limits. (b) Cut through x-y plane of coordinate frame B (top view): without mechanical joint limits

Figure 3.7: Centaur-like robot's workspace normalized manipulability index of each manipulator without mechanical joint limits: ($red > 0.66$), ($0.66 \leq green > 0.33$), ($0.33 \leq blue > 0.001$), ($black \leq 0.001$).

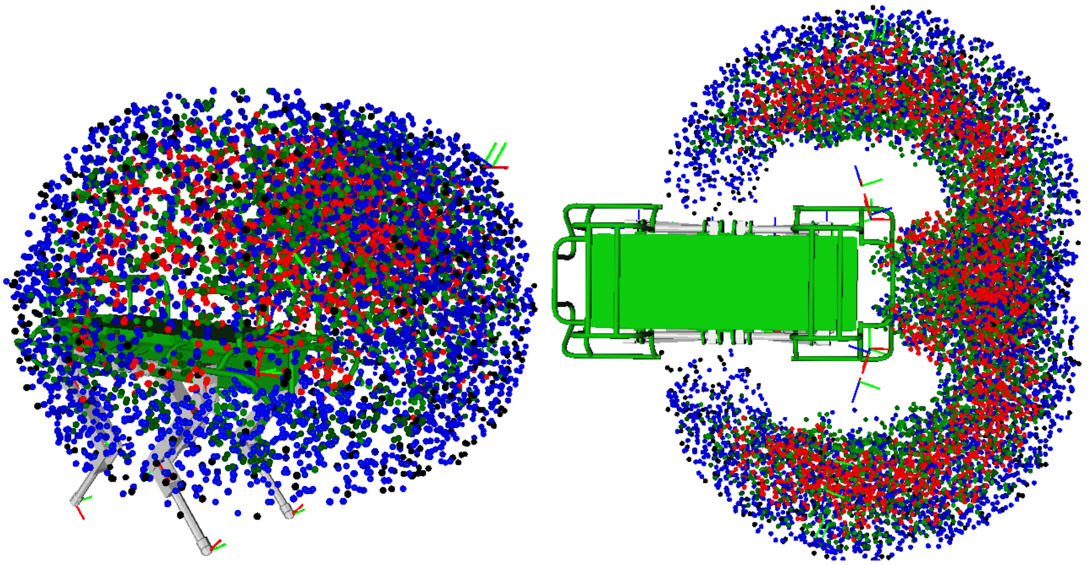

(a) Full workspace with mechanical joint limits. (b) Cut through x-y plane of coordinate frame B (top view): with mechanical joint limits.

Figure 3.8: Centaur-like robot's workspace normalized manipulability index of each manipulator with mechanical joint limits: ($red > 0.66$), ($0.66 \leq green > 0.33$), ($0.33 \leq blue > 0.001$), ($black \leq 0.001$).

Joint	**Range-of-motion of Right arm** $[rad]$	**Range-of-motion of Left arm** $[rad]$
SAA	-1.57 to 0.52	-0.52 to 1.57
SFE	-0.74 to 0.83	-0.74 to 0.83
HR	-1.598 to 0.068	-0.068 to 1.598
EFE	0 to 2.21	0 to 2.21
WR	-2.08 to 1.57	-1.57 to 2.08
WFE	-0.52 to 1.57	-0.52 to 1.57

Table 3.4: Selected mechanical joint limits based on normalized manipulability index.

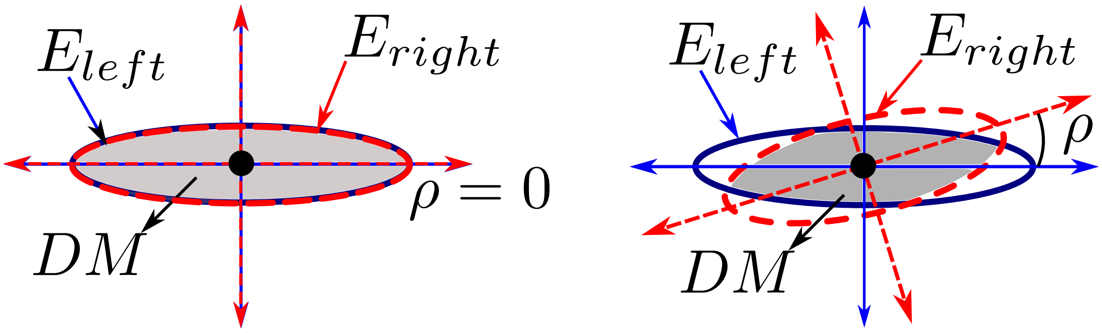

(a) Dual-arm Manipulability (DM)

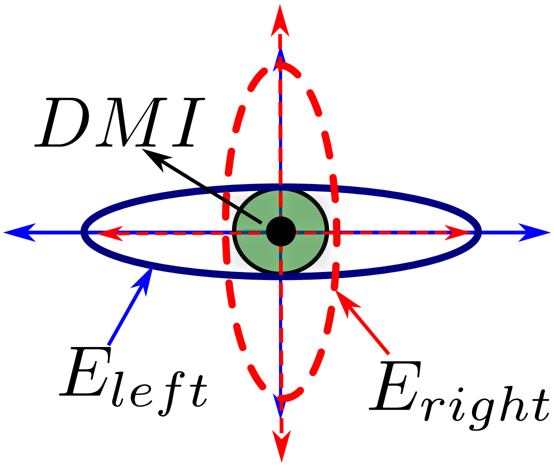

(b) Dual-arm Manipulability Index (DMI)

Figure 3.9: (a) Dual-arm Manipulability is defined as the volume of the intersection between the manipulability ellipsoids for the individual arms, where blue sold-line and red dash-line ellipse are 2D presentation of left and right ellipsoid with their major and miner principle axis, respectively. The ρ is angle between left and right ellipse major axis and the gray shaded area represent DM. (b) Dual-arm Manipulability Index is the minimum intersection volume, when both the individual arms ellipsoids are perpendicular to each other

3.3.2.2 Dual-arm Manipulability Index

[Lee and Lee, 1988] defined the dual-arm manipulability (DM) as the volume of the intersection between the manipulability ellipsoids for the individual arms as shown in

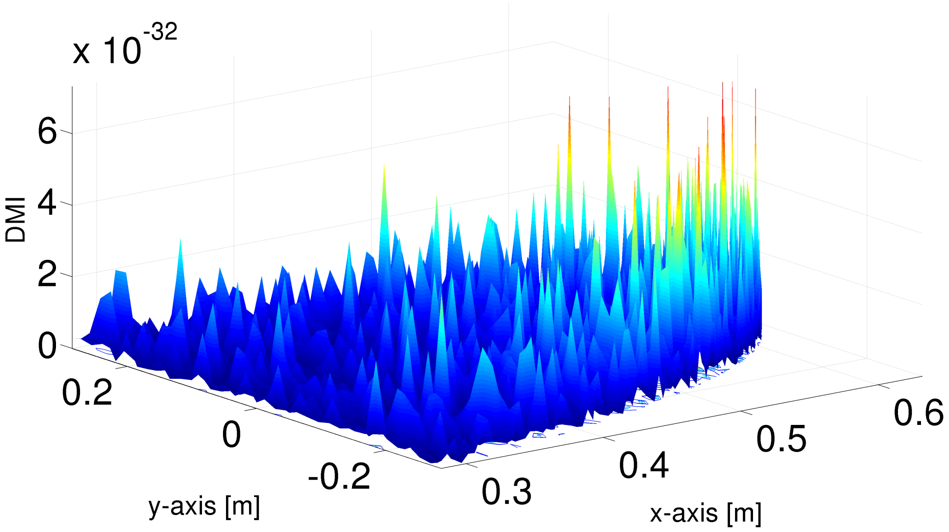

Figure 3.10: Dual-arm Manipulability Index within common workspace of both manipulator shown on in x-y plan of mobile. Where shoulder attachment parameters are $\theta_1 = 0$, $\theta_2 = 0$, $d_x = L/2$ $d_y = W$ (for further detail see Section. 3.2.1.3).

Fig. 3.9(a). The dual-arm manipulability has maximum value (maximum overlapped volume) within common workspace when both the individual arms, ellipsoids are perfectly overlapped. Furthermore, the intersection volume of both the individual arms, ellipsoids will always greater than or equal to $(\pi\lambda_{l_{min}}\lambda_{r_{min}})$. Therefore, the minimum intersection volume within common workspace will be equal to $(\pi\lambda_{l_{min}}\lambda_{r_{min}})$ only if both the individual arms, ellipsoids are perpendicular to each other as shown in Fig. 3.9(b). This minimum intersection volume is called Dual-arm Manipulability Index (DMI) [Bagheri et al., 2015] and defined as:

$$DMI = \pi\lambda_{l_{min}}\lambda_{r_{min}} \tag{3.7}$$

I used (3.7) to calculate the minimum dual-arm manipulability at each Cartesian position within the whole common workspace of both manipulator. Figure. 3.10 shows the DMI value of each Cartesian position within the common workspace of the both arms in x-y plane of a mobile robot (HyQ), when shoulder attachment parameters are $\theta_1 = 0$, $\theta_2 = 0$, $d_x = L/2$ and $d_y = W$ (for detail see Section. 3.2.1.3). Certainly changing shoulder attachment parameters will result in different DM value within common workspace and x-y plan of mobile robot. Therefore, I have to find a set shoulder attachment parameters which maximize the minimum DM value for each Cartesian position within common workspace.

3.3.3 Optimization of Shoulder Base Attachment of Centaur-like Robot Based on Workspace Analysis and Performance Index

The target design parameters for shoulder base attachment are defined in (3.1), I am re-writing for convenience:

$$x_{SDP} = [\theta_1, \theta_2, d_x, d_y] \tag{3.8}$$

These parameters are the unknown parameters that directly relate to (a) overall and common workspace, and (b) dual-arm manipulability index. The objective function is defined as:

$$\text{maximize} f(DMI_{volume}) = \sum_{x_c=x_{min_c}}^{x_{max_c}} \sum_{y_c=y_{min_c}}^{y_{max_c}} \left(DMI(x_c, y_c, \theta_1, \theta_2, d_x, d_y)\right) x_c y_c \tag{3.9}$$

$$\text{subject to the inequality constraints} \begin{cases} 0 \leq \theta_1 \leq 1.0472[rad] \\ 0 \leq \theta_2 \leq 1.0472[rad] \\ \frac{W}{2} = 0.25[m] \leq d_y \leq W = 0.5[m] \end{cases} \tag{3.10}$$

subject to the equality constraints:

$$x_{max_c} = \begin{cases} 0.6563 & \text{if } 0.50[m] \geq d_y > 0.45[m]; \\ 0.6667 & \text{if } 0.45[m] \geq d_y > 0.40[m]; \\ 0.6687 & \text{if } 0.40[m] \geq d_y > 0.35[m]; \\ 0.6789 & \text{if } 0.35[m] \geq d_y > 0.30[m]; \\ 0.6872 & \text{if } 0.30[m] \geq d_y > 0.25[m]; \\ 0.6882 & \text{if } 0.30[m] \geq d_y > 0.25[m]; \end{cases}$$

$$x_{min_c} = \begin{cases} 0.3120 & \text{if } 0.50[m] \geq d_y > 0.45[m]; \\ 0.3100 & \text{if } 0.45[m] \geq d_y > 0.40[m]; \\ 0.3050 & \text{if } 0.40[m] \geq d_y > 0.35[m]; \\ 0.3001 & \text{if } 0.35[m] \geq d_y > 0.30[m]; \\ 0.2910 & \text{if } 0.30[m] \geq d_y > 0.25[m]; \\ 0.2890 & \text{if } 0.30[m] \geq d_y > 0.25[m]; \end{cases} \tag{3.11}$$

$$y_{max_c} = \begin{cases} 0.2442 & \text{if } 0.50[m] \geq d_y > 0.45[m]; \\ 0.2528 & \text{if } 0.45[m] \geq d_y > 0.40[m]; \\ 0.2377 & \text{if } 0.40[m] \geq d_y > 0.35[m]; \\ 0.3306 & \text{if } 0.35[m] \geq d_y > 0.30[m]; \\ 0.3416 & \text{if } 0.30[m] \geq d_y > 0.25[m]; \\ 0.3552 & \text{if } 0.30[m] \geq d_y > 0.25[m]; \end{cases}$$

$$y_{min_c} = \begin{cases} -0.2442 & \text{if } 0.50[m] \geq d_y > 0.45[m]; \\ -0.2528 & \text{if } 0.45[m] \geq d_y > 0.40[m]; \\ -0.2377 & \text{if } 0.40[m] \geq d_y > 0.35[m]; \\ -0.3306 & \text{if } 0.35[m] \geq d_y > 0.30[m]; \\ -0.3416 & \text{if } 0.30[m] \geq d_y > 0.25[m]; \\ -0.3552 & \text{if } 0.30[m] \geq d_y > 0.25[m]; \end{cases} \tag{3.12}$$

$$d_x = \frac{L}{2} \tag{3.13}$$

Where DMI_{volume} is volume of DMI over entire common workspace and objective function (3.9) that I want to maximize given inequality (3.10) and equality constraints (3.11-3.13). In (3.9), x_c and y_c are Cartesian positions within a common workspace.

I implement an algorithm which calculates the minimum and the maximum values of x_c and y_c from manipulator(s) base link frame given the mechanical joint limits (see Table. 3.4), the d_x and d_y. The d_x is a fixed values 3.13 and d_y varies from the upper limit W to the lower limit $\frac{W}{2}$ with decremental of $0.05[m]$ per callback.

3.3.3.1 The Optimization result for Shoulder Base Attachment

The main goal of this optimization problem is to maximize the minimum values of DMI in entire common workspace and find optimized design parameters. I defined a numerical function called DMI_{volume} as our objective function (3.9). It define a relationship between dual-arm manipulability (DM) and design parameters. I selected the x-y plane of mobile platform base frame B in which I wanted to maximize the DMI value to find the optimized design parameters. To avoid local maxima, I tried various initial guess values for target design. Figure. 3.10 show the DMI values in the x-y plane of the mobile robot base frame B with "one of the initial guess" target design parameters as given in Table. 3.5. Whereas, Fig. 3.11 shows the dual-arm manipulability index within common workspace of both manipulator with optimized shoulder base attachment parameters for x-y plan of mobile platform (HyQ). The optimized parameters are listed in Table. 3.5, θ_1 is smaller then θ_2, which matches with our object goal to maximize DM within common workspace, if θ_1 is bigger then θ_2, then overall workspace will be bigger then common workspace. The optimized value of d_y is also less then the initially guessed values which is guarantee common and overall workspace within design constraints. Finally, after calculating all design parameters such as shoulder base attachment and mechanical joint limits of each actuated joint of the dual-arm system, the optimized workspace is shown in Fig. 3.12.

Design parameter	Initial guess	Optimized values
θ_1	$0[rad]$	$0.0832[rad]$
θ_2	$0[rad]$	$0.2655[rad]$
d_x	$0.5[m]$	$0.5[m]$ (Fixed)
d_y	$0.5[m]$	$0.3003[m]$

Table 3.5: Optimized designed parameters for WFE joint

3.3.4 Dynamics Simulation for Joints Torque and Speed Estimation

This section presents the simulation results for a set of "representative" tasks allowing the estimation of torque and velocity profiles. We used *SL* [Schaal, 2006] tasks servo to implement these desired tasks [2]. We designed the "representative" task to be demanding in terms of torque or velocity, for a single or a combination of joints. We developed minimum jerk trajectories for the end-effector of the arm in the Cartesian space (unless otherwise specified). These then resulted in the motion of the arm joints. The remaining joints are kept in a default configuration.

An impedance control law defined both for position and orientation sets the virtual forces/torques (F,T) at the end-effector and mapped into the arm joint torques τ_{arm}

---

[2] A brief introduction to SL architecture is given in Section 3.3.

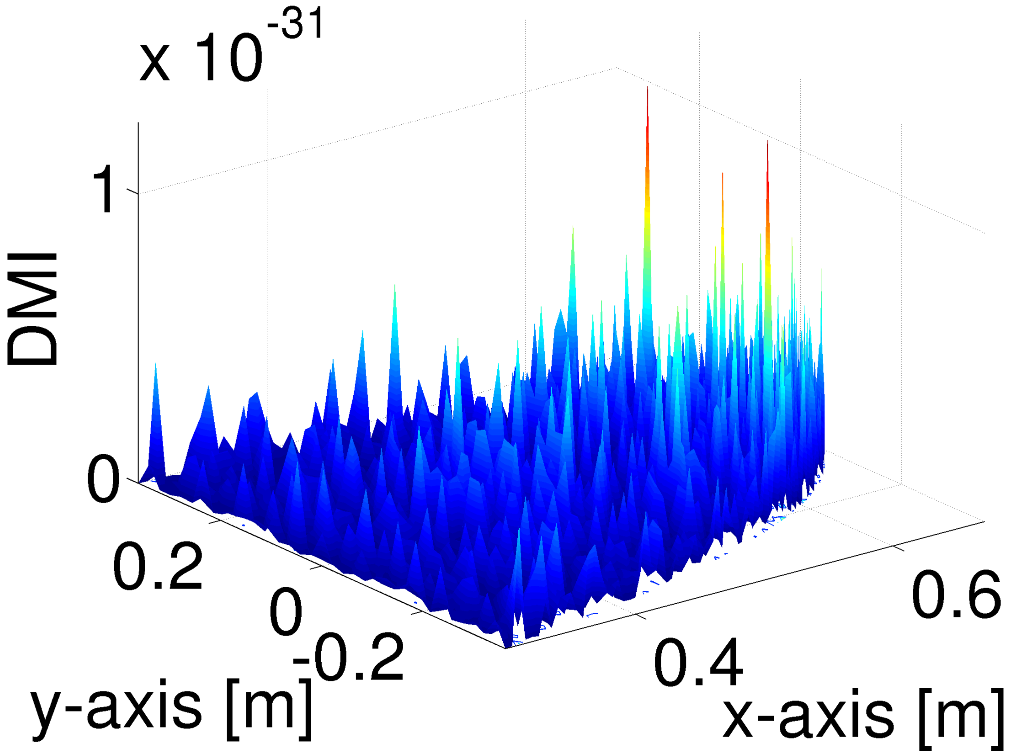

Figure 3.11: The Dual-arm Manipulability Index within common workspace of both manipulator shown on in x-y plan of mobile with optimized shoulder base attachment parameters.

through the Jacobian J as follows:

$$
\begin{aligned}
F &= P_x(x^d - x) + D_x(\dot{x}^d - \dot{x}) \\
T &= P_\theta e(R^d R^\top) + D_\theta(\omega^d - \omega) \\
\tau_{arm} &= J^T \begin{bmatrix} F \\ T \end{bmatrix}
\end{aligned}
$$

where $x^d, x, \dot{x}^d, \dot{x} \in \mathbb{R}^3$ are the desired/actual position/velocity of the end-effector, while $R_b, R_b^d \in \mathbb{R}^{3\times3}$ are coordinate rotation matrices representing its actual and desired orientation w.r.t. the robot base frame. $e(.) : \mathbb{R}^{3\times3} \rightarrow \mathbb{R}^3$ is a mapping from a rotation matrix to the associated rotation vector, $\omega \in \mathbb{R}^3$ is the angular velocity of the end-effector. Whereas $P_x, D_x, P_\theta, D_\theta \in \mathbb{R}^{3\times3}$ are positive-definite diagonal matrices of the impedance gains. An inverse dynamics algorithm [Featherstone, 2007] is compensating for the arm dynamics.
The explanation of each simulated task is presented as follows:

3.3.4.1 Lifting an Object

This task simulates the centaur robot lifting an object located at the end-effector when the arm is fully extended. It demands high torque for shoulder and elbow joints. We set three different kinds of trajectories for shoulder joints: *horizontal* (SAA), *vertical* (SFE), and *humerus rotation* (HR). Each scenario has been simulated *with* and

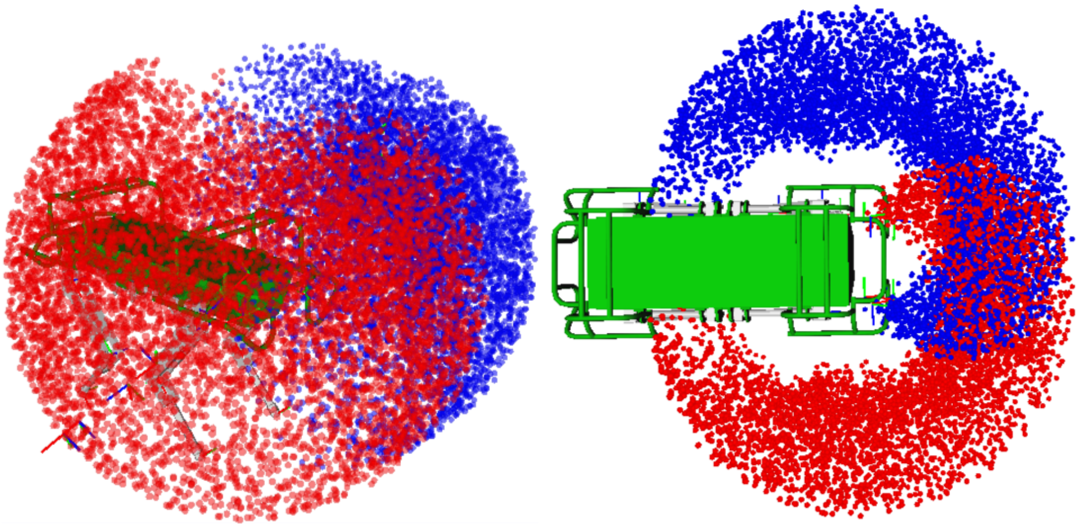

(a) Dual arm full workspace 3D view

(b) Dual arm full workspace, cut through x,y plane, when z=0.

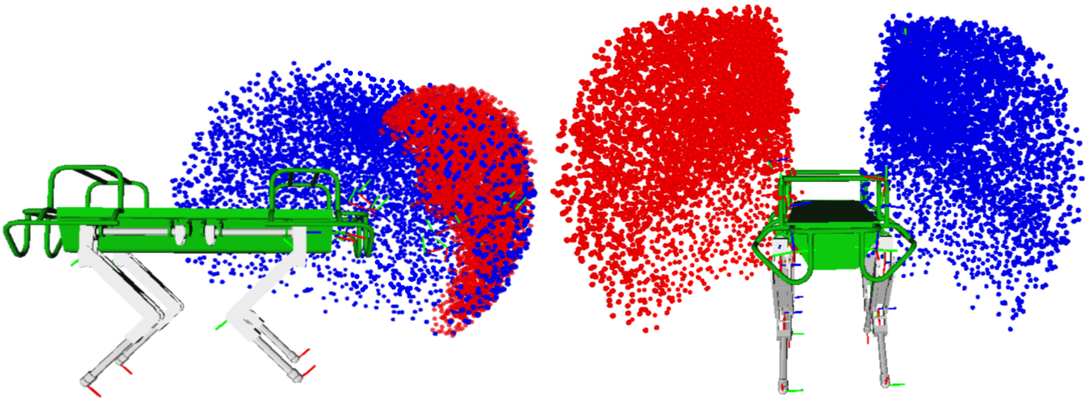

(c) Dual arm full workspace, cut through x,z plane, when y=0.

(d) Dual arm full workspace, cut through y,z plane, when x=0.5m.

Figure 3.12: The dual-arm system of the Centaur-like robot workspace with mechanical joint limits and optimized shoulder base attachment. Each manipulator end-effector position is calculated using forward kinematics. The red and blue point cloud represent right and left arms end-effector position within their workspace, using randomly generated joint angles with mechanical limits. The workspace obviously contains also all the white spaces between the points.

without a payload, which are two different estimations for maximum joint *torque* and *velocity*, respectively. We set a conservative payload of $5kg$ at end-effector moving at a speed of about $1.5m/s$ for the shoulder joints. These trajectories were also simulated without payload at a speed of $4m/s$ (three times faster than the robot falling time, which is explained in see Section 3.3.4.5). The Fig. 3.13 (first 3 rows), presents the estimated torque (with payload) and velocity (without payload) of lifting an object tasks for $3DoF$ the shoulder. These tasks resemble ([**SP1.3**]).

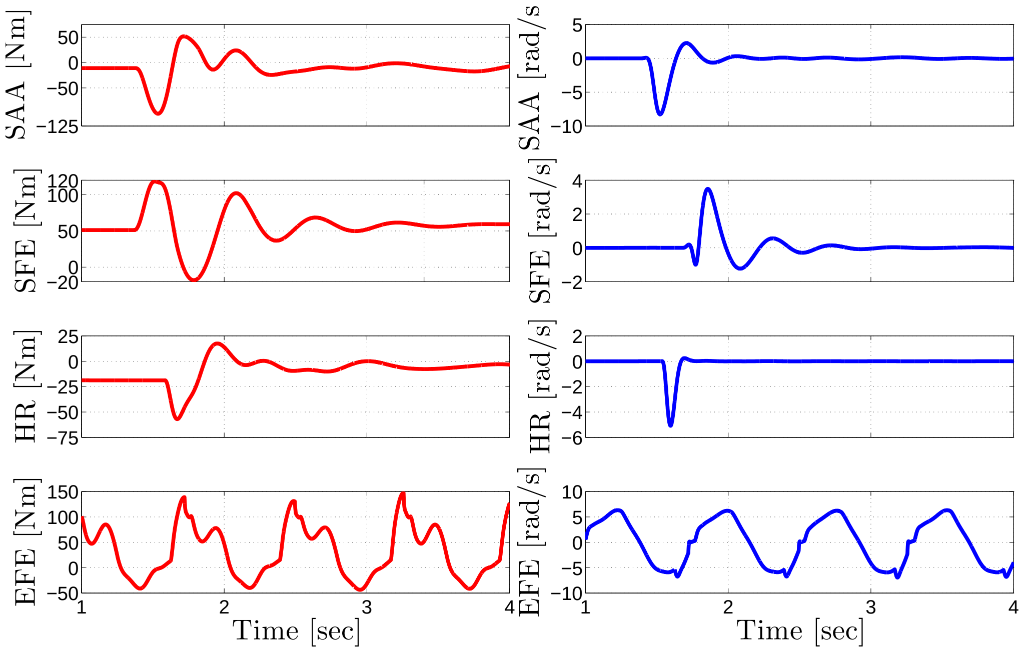

Figure 3.13: Lifting an object. The first three rows refer to the horizontal, vertical and humerus rotation task while the last row refers to the biceps curl task. First column: required peak torque $[Nm]$ with payload (red line), $SAA_{peak} = 101$, $SFE_{peak} = 118$, $HR_{peak} = 54$ and $EFE_{peak} = 150$. Second column: required velocity $[\frac{rad}{s}]$ without payload (blue line), $SAA_{peak} = 8.25$, $SFE_{peak} = 3.48$, $HR_{peak} = 5$, $EFE_{peak} = 7$.

3.3.4.2 biceps curl

In the case of the *biceps curl* task, we performed a single experiment setting a sine reference trajectory (frequency $1.3Hz$, amplitude $0.6[rad/s]$) only for EFE joint with $10kg$ payload, achieving a joint speed of $6rad/s$. Figure 3.13 (last row), presents the estimated torque (with payload) and velocity (without payload) for the elbow joint.

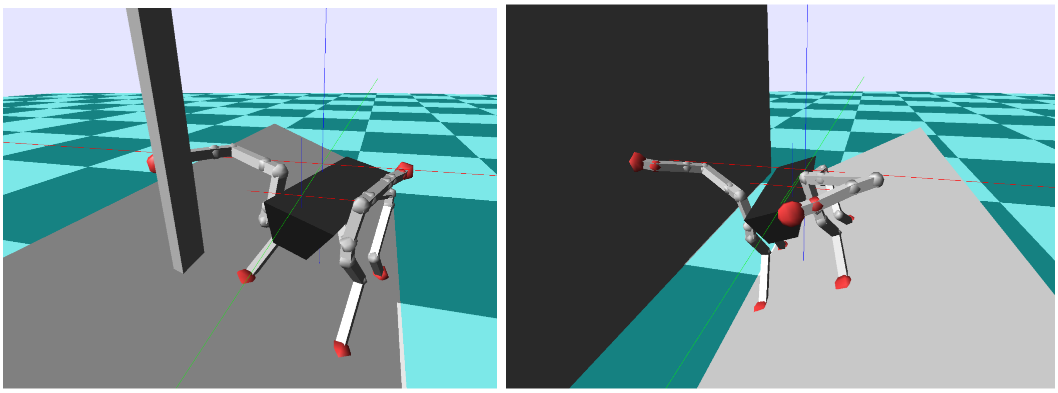

Figure 3.14: Picture of the Centaur simulation during the pull-up (left) and push-up (right) tasks.

3.3.4.3 Pull Up

This task demands a high torque output for the shoulder and elbow joints. In this task an arm is holding a vertical beam and pulling the robot torso (up to $0.3m$) towards the beam while standing on a slope of 0.5 rad inclination (Fig. 3.14 (left)). This task resembles opening a door (**[SP1.1]**) or pulling an object (**[SP1.2]**). Fig 3.15 presents the required torques and velocities.

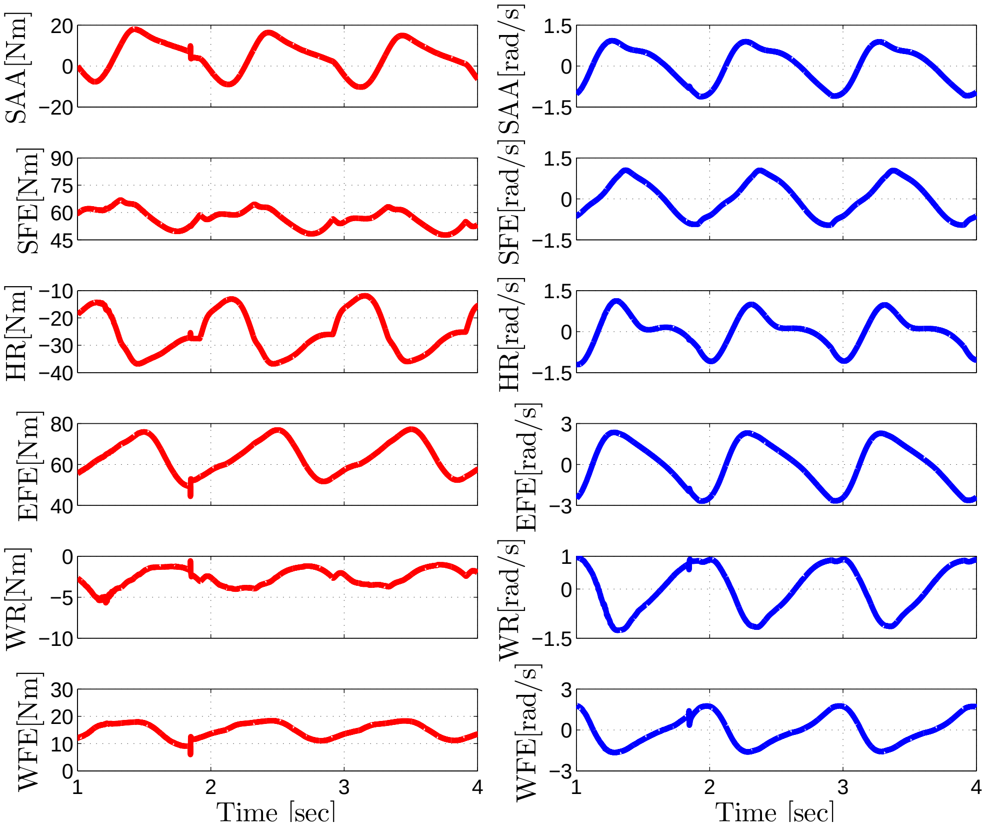

Figure 3.15: Pull Up. First column: Required peak torque $[Nm]$ (red line) $SAA_{peak} = 19$, $SFE_{peak} = 69.5$, $HR_{peak} = 38.5$, $EFE_{peak} = 75$ $WR_{peak} = 6$ and $WFE_{peak} = 18$. Second column: Required velocity $[\frac{rad}{s}]$ (blue line) $SAA_{peak} = 0.1$, $SFE_{peak} = 1.05$, $HR_{peak} = 1.18$, $EFE_{peak} = 2.4$ $WR_{peak} = 1.0$ and $WFE_{peak} = 2.0$.

3.3.4.4 Wall Push-up

The wall push-up task (Fig. 3.14(right)) demands high torque for shoulder and elbow joints. For this task the robot is standing on a 0.5 rad inclined slope and performing a push-up motion against a wall. This task resembles to providing assistance to the robot while climbing stairs or to balance (**[SP1.4]**,**[SP1.5]**). Fig 3.16 presents the required torques and velocities.

3.3.4.5 Fast Arm Reaction

This task corresponds to a scenario where the legs are unable to balance the robot against external disturbance and a fast arm reaction can help to recover the balance of the robot (**[SP1.4]**, **[SP1.5]**). A simulation of the centaur robot falling (on one

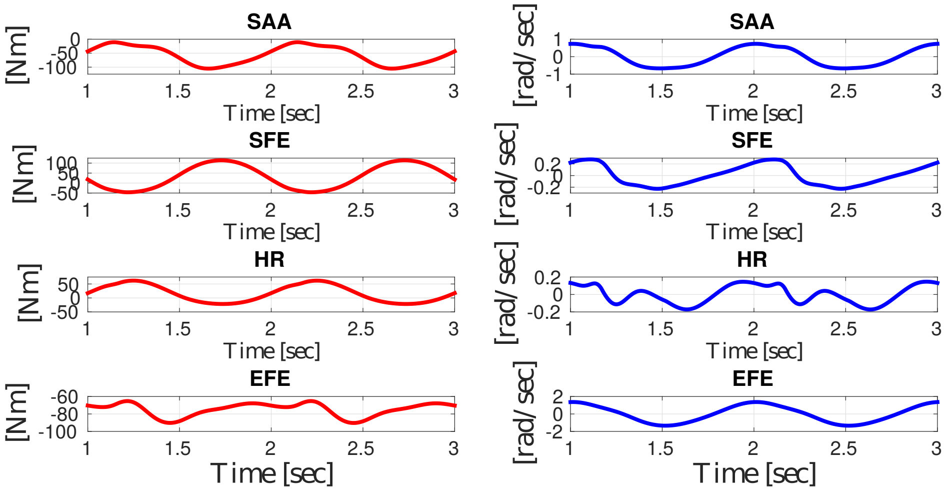

Figure 3.16: Wall push-up. First column: Required peak torque $[Nm]$ (red line) $SAA_{peak} = 105.2$, $SFE_{peak} = 113.92$, $HR_{peak} = 62$, $EFE_{peak} = 90.37$ $WR_{peak} = 4.8$ and $WFE_{peak} = 6.8$. Second column: Required velocity $[\frac{rad}{s}]$ (blue line) $SAA_{peak} = 0.73$, $SFE_{peak} = 0.27$, $HR_{peak} = 0.17$, $EFE_{peak} = 1.36$ $WR_{peak} = 0.57$ and $WFE_{peak} = 0.88$.

side) from a 0.5 rad inclined slope results in a falling time of 0.5s. According to this, the end-effector trajectory is generated, in order to have an effective reaction within this time interval (retraction time 0.12s, max speed 2.5m/s). Figure 3.17 shows the required torque and speed for the affected joints.

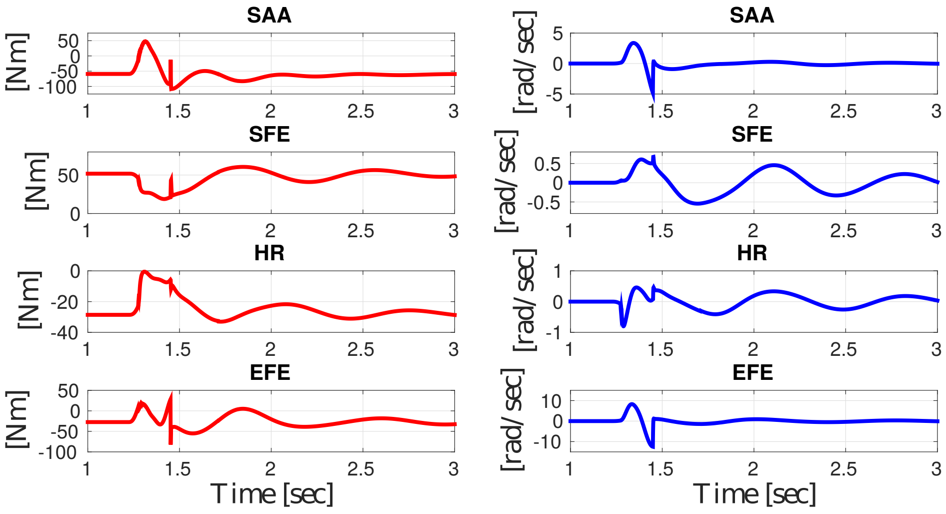

Figure 3.17: Fast arm reaction task, first column: required peak torque $[Nm]$ (red line). Second column: required velocity $[\frac{rad}{s}]$ (green line) $SAA_{peak} = 4.9$, $SFE_{peak} = 0.5$, $HR_{peak} = 0.7$ and $EFE_{peak} = 12.5$.

3.3.4.6 Dynamics Simulation Results Analyses

The simulation results provide a rich data set in terms of joint range-of-motion, velocity, and torque output. The Fig. 3.18, summarizes the peak estimated required torque for each representative task. Whereas the Fig. 3.19 describes the required velocity/speed for each joint for all the simulated tasks. In the next section, I will use the simulation results to select commercially available hydraulic actuators and servo valve.

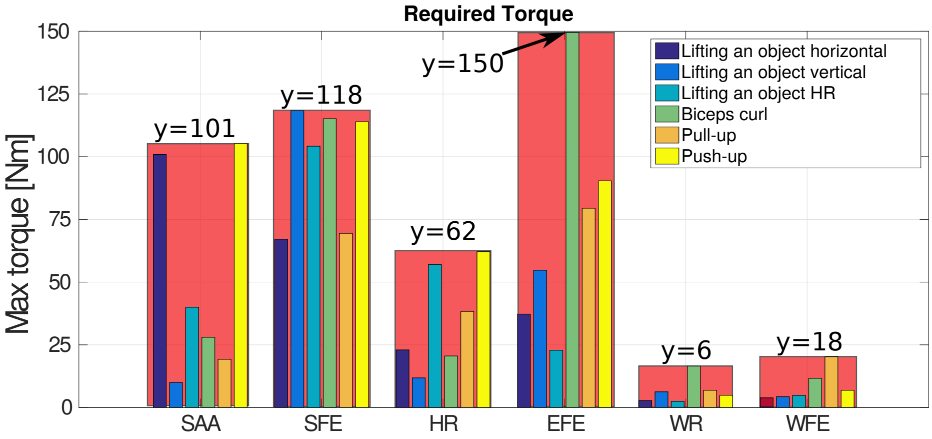

Figure 3.18: The summary of estimated required torque for all the 6 arm joints based on simulated results of each "representative" tasks under payload.

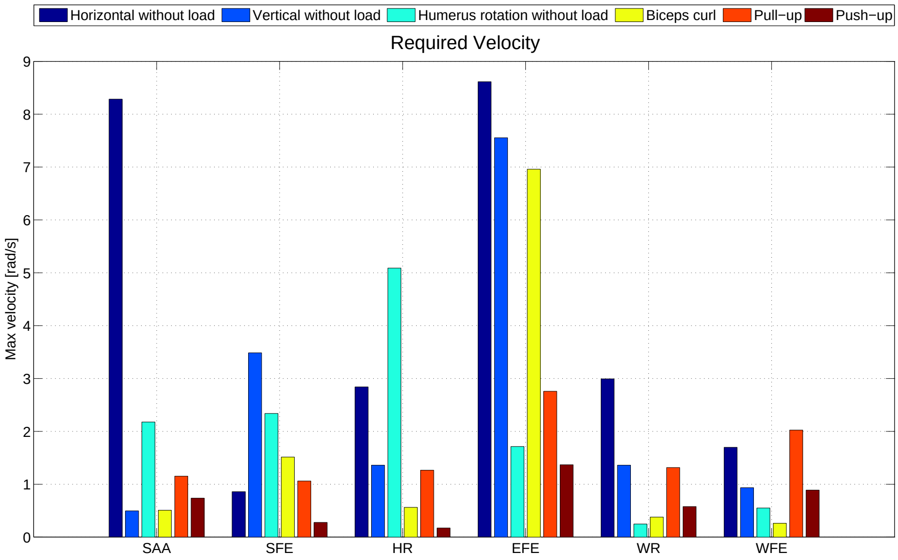

Figure 3.19: The estimated required velocity for lifting an object, biceps curl, pull-up, push-up and fast arm reaction tasks for all 6 arm joints.

Joint	Range of motion $[rad]$	Simulation Task maximum demanding	Torque $[Nm]$	Speed $[rad/s]$
SAA	-1.57 to 0.52	Lifting object (H)	101	8.255
SFE	-0.74 to 0.83	Lifting object (V)	118	3.486
HR	1.598 to 0.068	Lifting object (HR)	62	25
EFE	0 to 2.21	Biceps curl	150	7
WR	-2.08 to 1.57	Pull up	6	1.0
WFE	-0.52 to 1.57	Pull up	18	2.0

Table 3.6: The estimated required joint specification based on simulation results.

3.4 Hardware Selection

In this section, I will analyse the estimated joint range-of-motion, velocity, and torque output profiles of each task to select robot joint actuators and servo valves. To ensure design specifications ([**SP2.2, SP2.4, SP2.6**]), provided simulation results. The commercial availability of light-weight and compact hydraulic actuators are very limited. The hardware selection process is organized as follows: (1) a case study on the commercial availability of suitable hydraulic actuators type and selection, (2) mapping simulation results to actuators, and (3) required flow estimation for servo valve.

3.4.1 Actuator Selection

Traditionally, an electro-hydraulic actuator unit is formed by an electric servo valve and a linear cylinder to produce forces as shown in Fig. 3.20a. An intermediate element (linkage) is necessary to transform the linear motion into rotational motion (for a rotational joint). An alternative exists, which is to use hydraulic rotary motors to directly produce constant torques over an entire range-of-motion as shown in Fig. 3.20b. The main advantage of this type of actuators is its constant torque output and compactness. The hydraulic motors comes in two different configurations, single or double vane. A single vane provides a larger range of motion and half torque output compared to a double vane configuration. Normally a single vane motor is used where a wide range-of-motion is required, where as a double vane design is used where high torque output is a primary requirement.

On the other hand, a conventional hydraulic cylinder has a much higher power-to-weight ratio than rotary actuators. A carefully designed of a mechanism (linkage) is needed to convert the linear cylinder force to torque, that provides a close approximation to the required torque profile. Based on simulation results, I performed an intensive survey to find suitable hydraulic actuators. The key features were light-weight, compact, and closer to estimated required torque. To this end, I selected hydraulic rotary motor and cylinders. Table. 3.7 and 3.8 summarize the key features of the most suitable rotary motors and cylinder, respectively.

Due to high power-to-weight ratio, hydraulic cylinders are preferable over rotary motors. However, it is challenging to acquire a wide range-of-motion using hydraulic cylinders. Using linkage mechanisms to convert the cylinder output force to torque results in a non-linear profile. Designing specialized mechanism for all of the joints will result in bulky and complex mechanical structures. On other hand, using rotary motors will ensure compact, wide rang-of-motion and constant torque output. Designing an arm actuated by just using rotary motors will results in compact but heavy design. Table. 3.9, summarize a comparison between different combination of hydraulic actu-

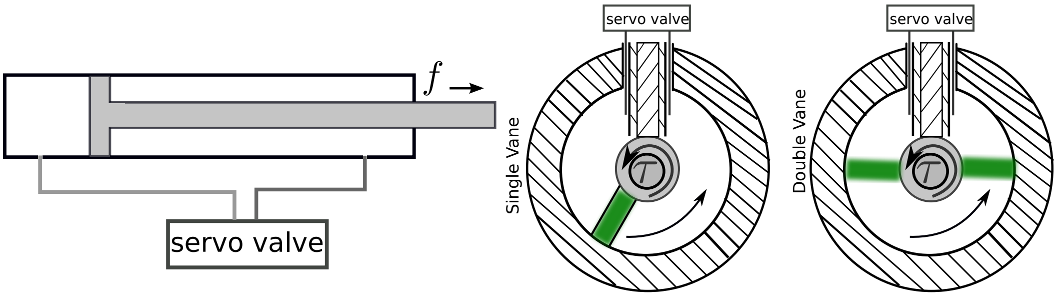

(a) (b)

Figure 3.20: Hydraulic (a) asymmetric cylinder and (b)single and double rotary actuators

ators. This comparison is based on commercially available small size actuator torque output and total actuator weight for all six joints.

Type of actuator	Dimension [L x W x H]	Range of motion [Degree]	Torque [Nm] at 20[MPa]	Weight [kg]
Single vane (RMSV1)	83 x 59 x 59	280	60	0.95
Double vane (RMDV1)	83 x 59 x 59	100	120	0.98
Single vane (RMSV2)	96 x 80 x 80	280	126	1.8
Double vane (RMDV2)	96 x 80 x 80	100	252	2.0

Table 3.7: Specifications of Small size commercially available and customized hydraulic rotary motors. Where (RMSV1-2) Rotary Motor Single Vane actuator type 1 and 2, (RMDV1-2) Rotary Motor Double Vane actuator type 1 and 2, respectively.

Type of cylinder	Asymmetric cylinder 1 (AC1)	Asymmetric cylinder 2 (AC2)
Bore/rod diameter$[m]$	0.016/0.008	0.016/0.008
Piston/annulus area $[m^2]$	0.022/0.015	0.022/0.015
Stroke length $[m]$	0.40	0.70
Weight kg	0.135	0.166
Force at 20$[MPa]$	$F_{ext} = 4021$ $F_{ret} = 3014$	$F_{ext} = 4021$ $F_{ret} = 3014$

Table 3.8: Specifications of small size commercially available hydraulic cylinders. Where (AC1-2) Asymmetric hydraulic Cylinder type 1 and 2, respectively.

The combination 1, provides wide range-of-motion but the total weight is about $7.48kg$, which is too heavy for required design specifications [**SP2.2**] and EFE joint motor torque is less than the estimated required torque. The combination 2 total weight is $1kg$ lighter but still the EFE joint torque is not enough (see Fig. 3.18). The combination 3 is $2kg$ less but the WFE joint is oversized in terms of required joint torque and range-of-motion (see Fig. 3.18 and Table. 3.6). Clearly, the combination 4 is best in terms of overall actuator weight and torque output. But How to ensure that the hydraulic cylinder can provide required joint torque and range-of-motion? In the next section, I will address this question and explain the hydraulically actuated arm (HyArm) actuator configuration.

No.	SAA	SFE	HR	EFE	WR	WFE	total
1	RMSV2 126 Nm 1.8kg 280[deg]	RMDV1 120 Nm 0.98kg 100[deg]	RMDV1 120 Nm 0.98kg 100[deg]	RMSV2 126 Nm 1.8kg 280[deg]	RMSV1, 60 Nm 0.95kg 280[deg]	RMSV1 60 Nm 0.95kg 280[deg]	7.46 kg
2	RMSV2 126 Nm 1.8kg 280[deg]	RMDV1 120 Nm 0.98kg 100[deg]	RMDV1 120 Nm 0.98kg 100[deg]	RMSV2 60 Nm 0.95kg 280[deg]	RMSV1, 60 Nm 0.95kg 280[deg]	RMSV1 60 Nm 0.95kg 280[deg]	6.61kg
3	RMSV2 126 Nm 1.8kg 280[deg]	RMDV1 120 Nm 0.98kg 100[deg]	RMDV1 120 Nm 0.98kg 100[deg]	AC2 $F_{ext} = 4021N$ 0.166kg 280[deg]	RMSV1, 60 Nm 0.95kg 280[deg]	RMSV1 60 Nm 0.95kg 280[deg]	5.82kg
4	RMSV2 126 Nm 1.8kg 280[deg]	RMDV1 120 Nm 0.98kg 100[deg]	RMDV1 120 Nm 0.98kg 100[deg]	AC2 $F_{ext} = 4021N$ 0.166kg	RMSV1, 60 Nm 0.95kg 280[deg]	AC2 $F_{ext} = 4021N$ 0.135kg 280[deg]	5.01kg

Table 3.9: Summary of a comparison between different actuators combination. For a fair comparison between hydraulic cylinder and motor weight, one should also consider the linkage assembly that convert cylinder force into respective joint torque.

3.4.1.1 Robotic Manipulator Joints Actuator Configuration

Robotic manipulator joints actuators are selected as a combination of rotary and linear hydraulic actuators. The benefit of using this combination is to achieve large joint ranges while still ensuring both a compact and light-weight design. The manipulator shoulder joints ($3DoF$) are equipped with rotary motors to improve compactness and achieve a wider range of motion. All the rotational axes of the shoulder joints cross through the same point. Another advantage of this choice is that the actuator masses are located closer to the arm base which reduces the arm inertia. The first row in Fig. 3.21, presents results of each representative task in terms of required torque and range-of-motion. The super-imposed red and blue dash lines represent selected actuator torque output limits. The selected actuators for shoulder joints provide required torque and joint range-of-motion, hence suitable for shoulder joints.

The elbow joint (EFE) is actuated by a hydraulic cylinder. This has the advantage that the whole elbow assembly is part of the upper arm. This provides structural rigidity and distributes the mass of the elbow joint across the link, achieving a lower inertia. The selected actuator is six times lighter then a rotary motor. To create the rotational motion a specialized linkage mechanism is designed to achieve the required range-of-motion and torque. Using a linkage mechanism to convert the cylinder output force to torque results in a non-linear profile and can be approximate as a polynomial as shown in Fig. 3.21 (Section 4.2.2 provides a detailed explanation). Normally a hinge mechanism can be used to convert cylinder linear force into torque. We designed an

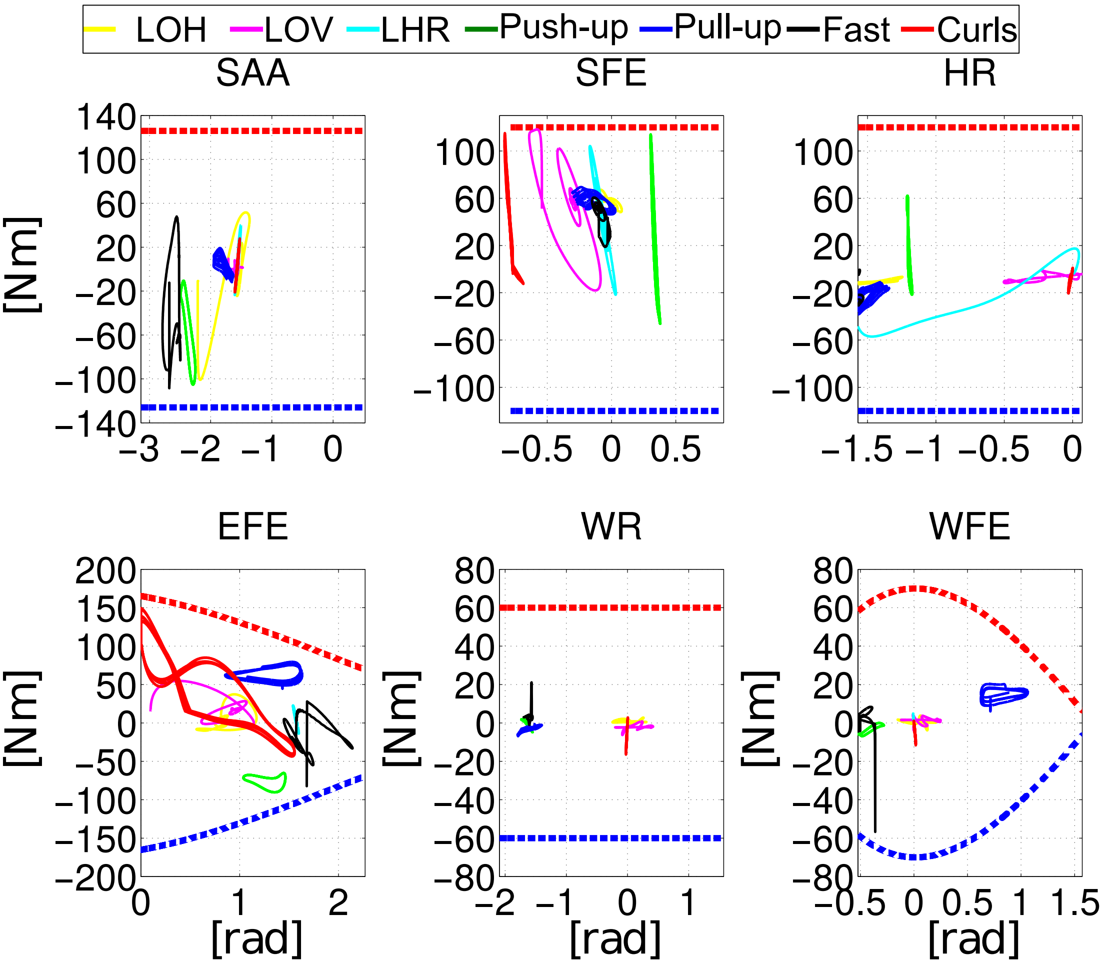

Figure 3.21: The results of each representative task in terms of required torque and rang-of-motion. The super-imposed red and blue dash lines represent selected actuator torque output limits. Where LOH stands for lifting an object horizontally, the lifting an object vertically is named as LOV and lifting an object with humerus rotation is called LHR.

optimized four bar linkage mechanism based on torque profile provided by polynomial shown in red and blue in Fig. 3.21.

The wrist joints play an important role in determining end-effector position and orientation. For the WR joint we selected a rotary actuator to achieve required range-of-motion and torque, while the WFE joint is actuated by a cylinder. A standard lever mechanism is designed to satisfy required joint torque output profile and range-of-motion. The mechanisms design for both EFE and WFE is explained in Chapter 4. Table 3.10 summarizes the main characteristics of the selected hydraulic cylinders and rotary actuators.

3.4.2 Servo Valve

In this section I investigate the flow requirement from our actuator. The purpose is two-fold: 1) sizing of the servo-valve (in this section) and 2) sizing of the hydraulic lines and

Table 3.10: Specification of hydraulic cylinder and rotary actuators

Cylinder specifications	**Value**
Bore and rod diameter$[m]$	0.016, 0.008
Piston and annulus area $[m^2]$	0.022, 0.015
Stroke length $[m]$	EFE = 0.07, WFE=0.04
Weight $[kg]$	EFE = 0.166, WFE=0.135
Max. operating pressure $[MPa]$	20
Force $[N]$	$F_{ext} = 4021$ $F_{ret} = 3014$

Single Vane rotary motor specs.	**Value**
Total range-of-motion$[rad]$	SAA=4.71 WR = 4.88
Volumetric displacement $[m^3/rad]$	SAA=7.3x10^{-6} WR= 3.38x10^{-6}
Weight $[kg]$	SAA=1.83, WR=0.95
Max. operating pressure $[MPa]$	20
Torque $[Nm]$	SAA=126, WR=60

Double Vane rotary motor specs.	**Value**
Total range-of-motion $[rad]$	SFE=HR=1.74
Volumetric displacement $[m^3/rad]$	SFE=HR=6.76x10^{-6}
Weight $[kg]$	SFE=HR=0.98
Max. operating pressure $[MPa]$	20
Torque $[Nm]$	SFE=HR=120

Total weight of actuators $[kg]$	5.01

manifold design (Section 4.3). The servo valve regulates hydraulic flow between pressure lines and actuator chambers and must be able to provide the pressure/flow required by desired task. To this extent, I used simulated data from the each representative tasks which involved fast motion (e.g, without payload motion; see Section 3.3). We estimated the required load pressure p_l and effect flow Q_e. The load pressure for the hydraulic motor and cylinder are defined in (3.14) and (3.15), respectively.

$$p_l = \frac{\tau_m}{V_d} \tag{3.14}$$

$$p_l = \frac{F_{cyl}}{A_p} \tag{3.15}$$

where V_d is the volumetric displacement, τ_m is motor torque output and A_p is the cylinder piston area, F_{cyl} is cylinder force. The required (effective) flow Q_e is computed by the joint velocity and defined in (3.16) and (3.17) for the hydraulic motor and cylinder, respectively.

$$Q_{e_m} = V_d \dot{\theta}_m \tag{3.16}$$

$$Q_{e_{cyl}} = A_p \dot{x}_{cyl}. \tag{3.17}$$

Where $\dot{\theta}_m$ is the rotary motor angular and $\dot{x}_{cyl}$ are the cylinder liner velocities[3]. Figure 3.22 show the estimated required flow and load pressure required for each joint during the performing of simulated tasks. For the valve selection, weight, flow leakage and

---

[3] The relation between joint angular velocity (θ_{EFE} and θ_{WFE}) and cylinder linear velocity $\dot{x}_{cyl}$ for respective joints are defined in Chapter 4

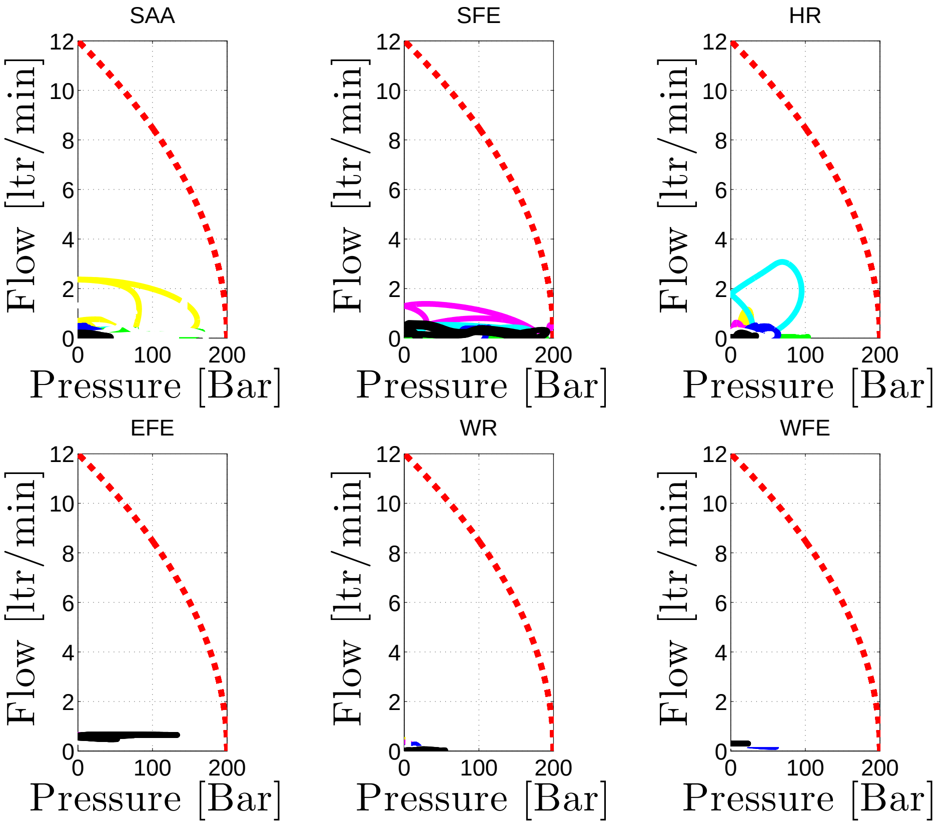

Figure 3.22: The solid lines are flow-pressure requirements for each joint estimated with simulated data. The dashed line red line is Moog E24 servo-valve flow-pressure curve.

control bandwidth are the most critical parameters. I selected a Moog E24 servo valve because of the high bandwidth ($250Hz$) characteristics and its light weight ($92g$). The valve high bandwidth is a critical feature for developing a high performance torque controller [Boaventura et al., 2012b]. On top of each plot in Fig. 3.22, I super-imposed the servo valve model pressure-flow characteristic curve, which is suitable to cover the maximum required flow for all joints. The selecting the same servo valve type for all joints is not the optimal selection, e.g it would be better to use smaller flow rate servo valves, especially for the last three joints for last three joints. Table 3.11 summarizes peak joint speed and maximum required flow-pressure for the simulated tasks.

Joint	**Task Description** maximum demanding	**Speed** [rad/s]	**Flow** [ltr/min]	**Pressure** [bar]
SAA	Lifting an object (H)	8.255	2.114	159.8
SFE	Lifting an object (V)	3.486	1.384	195.9
HR	Lifting an object (HR)	5	3.052	103
EFE	Biceps curl	6.75	0.66	133.1
WR	Pull up	1	0.26	23
WFE	Pull up	2	0.25	60.88

Table 3.11: Peak Joint Speed and required Flow-Pressure

Chapter 4

Robotic Arm Hardware Design and Integration with HyQ

This chapter describes the mechanical design of the robotic arm and integration with multi-legged mobile platform HyQ. I named the robotic arm "HyArm," which is the abbrevation of **Hy**draulic **Arm** and is pronounced [hai-arm] [Rehman et al., 2015] as shown in Fig. 4.1. This chapter is organized in the following manner: Section 4.1 provides the summary of designed robotic arm and key specifications. Section 4.2 presents in detail the mechanical design of HyArm. This section is divided into shoulder, elbow, and wrist joint design sections in a sequential manner. Section 4.3, describes the

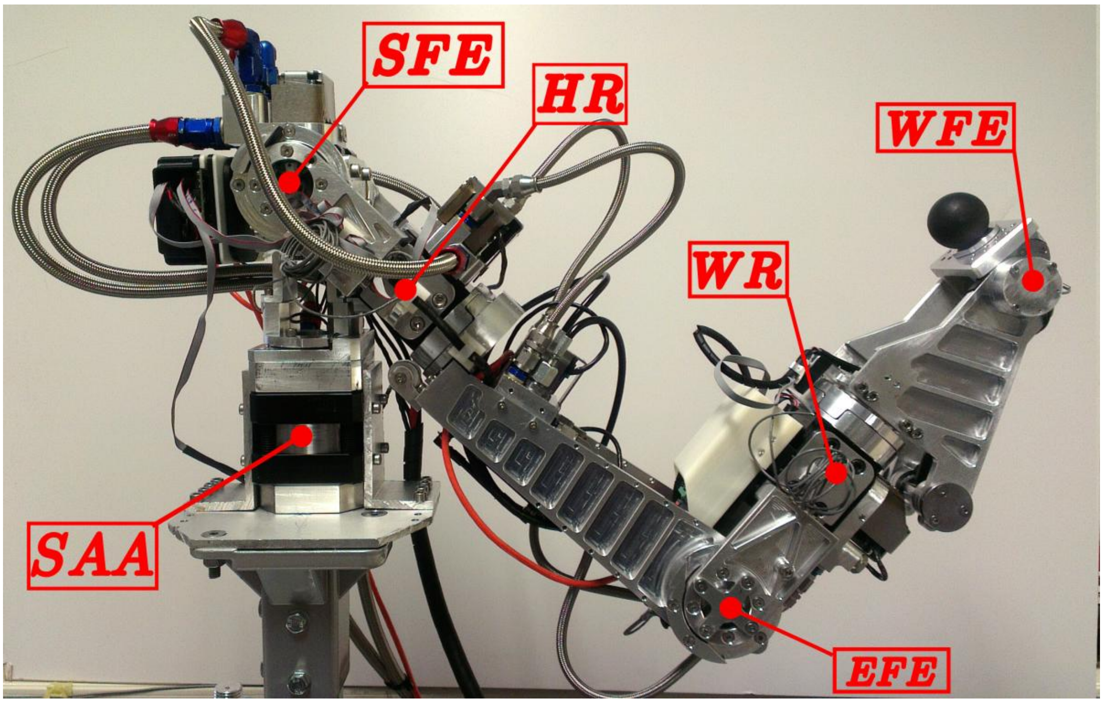

Figure 4.1: HyArm: A fully torque-controlled **Hy**draulic **A**rm. The labels in the figure show the 6 joint axes with abbreviated names: Shoulder Adduction/Abduction (SAA), Shoulder Flexion/Extension (SFE), Humerus Rotation (HR), Elbow Flexion/Extension (EFE), Wrist Rotation (WR), Wrist Flexion/Extension (WFE). A single spherical rubber ball is shown as end-effector which can be replaced by different grippers.

hydraulic manifold and Section 4.4 presents the electronics and control system layout for robotic arm. Section 4.5 presents the hardware integration of the robotic arm with HyQ in single and dual-arm configurations.

4.1 Robotic Arm System Overview

The HyArm is a fully torque-controlled and hydraulically actuated (see Fig. 4.1), tailored for an $80kg$ quadruped robot HyQ (see Section 3.2.1.1 for further details). The arm is designed to be compact, light-weight and able to carry a heavy payload. As mentioned earlier (see Section 3.4.1.1), the HyArm has six DoFs actuated with a combination of hydraulic motors and cylinders. Its shoulder joints, adduction/abduction (SAA), flexion/extension (SFE), and humerus rotation (HR) are actuated by hydraulic motors. The elbow flexion/extension (EFE) joint is actuated by a hydraulic cylinder. The wrist rotation WR joint is actuated by a hydraulic motor to achieve a wide range-of-motion. Finally, the last joint wrist flexion/extension WFE is actuated by a cylinder. Each joint is equipped with position encoders and torque/force sensors to achieve torque control. Tables. 4.1 and 4.2, presents an overall system review and joint specifications. Table. 4.3 provides a list of robotic arm link segments and components with their respective weight. The total weight of each segment also includes the hydraulic motor or cylinder, servo valve, manifold, torque or force sensor, position encoder and the linkage parts for EFE and WFE. This list also summaries the total weight of all hydraulic hoses and on board electronics. In the next section, I will discuss the mechanical design of each robotic arm joint.

Maximum arm extension	$0.743m$
Weight	$12.5kg$
Maximum payload	$10kg$
Actuation system	Hydraulics
Degree of freedom	$6Dof$ (3+1+2)
Control mode	Position/torque
Controller rate	1kHz (torque and position all joints)
Position sensors	19 bit absolute encoder
Torque sensors	custom-designed strain-gage torque sensors
Force sensors	load cell

Table 4.1: System Overview of the HyArm

4.2 Mechanical design

The simulated tasks in Chapter. 3 provided the required joint range-of-motion, torque, and velocity. Based on these results (see Section 3.4), I selected the components such as actuators, servo valve and bearings. The robotic arm is designed to be modular, so

Joint	**Range of motion**$[rad]$	**Torque**$[Nm]$
SAA	-1.57 to 0.52	126
SFE	-0.74 to 0.83	120
HR	1.598 to 0.068	120
EFE	0 to 2.21	225$[Nm_{peak}]$
WR	2.04 to 1.57	60
WFE	-0.52 to 1.57	100$[Nm_{peak}]$

Table 4.2: The HyArm joint range-of-motion and torque output. See Fig. 3.2 to see the zero configuration of all the arm joint angles.

Robot parts/components	**Weight**
SAA assembly	3.10[kg]
SFE assembly	2.14[kg]
HR assembly	1.48[kg]
EFE assembly	1.95[kg]
WR assembly	1.58[kg]
WFE assembly	1.54[kg]
Hydraulic hoses, adaptors and connectors	0.45[kg]
On board electronics	0.26[kg]
Total weight	12.50[kg]

Table 4.3: List of all the robotic arm segments and components with their weight. The total weight of each segment also includes the hydraulic motor or cylinder, servo valve, manifold torque or force sensor and position encoder. This list also provides hydraulic hoses and on board electronics total weight.

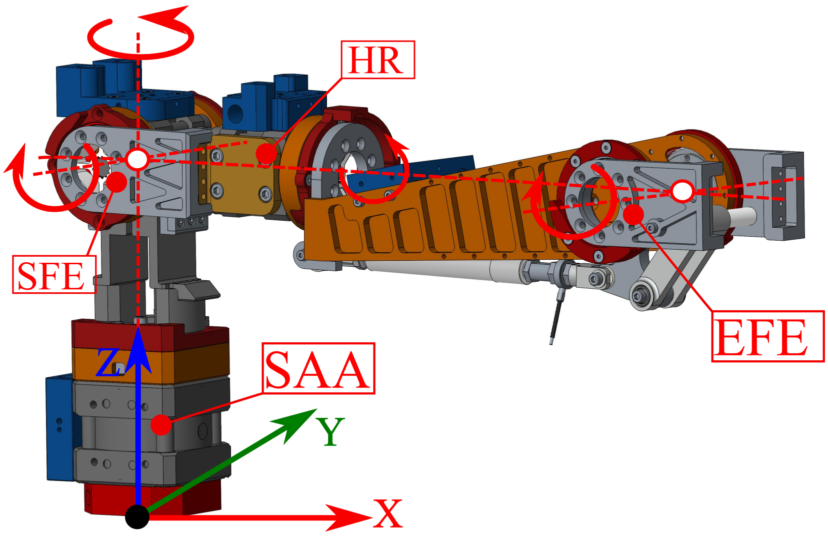

Figure 4.2: Shoulder and elbow joints configuration

it can be easily assembled and disassembled for maintenance. Each part is designed with the consideration that only a few of them are required to be modified in order to get left or right arm configurations.

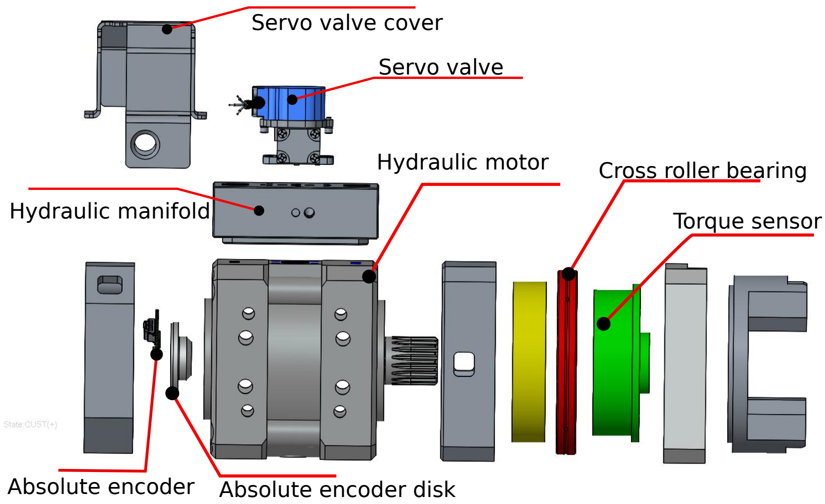
Servo valve cover
Servo valve
Hydraulic motor
Cross roller bearing
Hydraulic manifold
Torque sensor
Absolute encoder
Absolute encoder disk

(a) Shoulder Adduction/Abduction (SAA) joint's CAD mechanical assembly in exploded view.

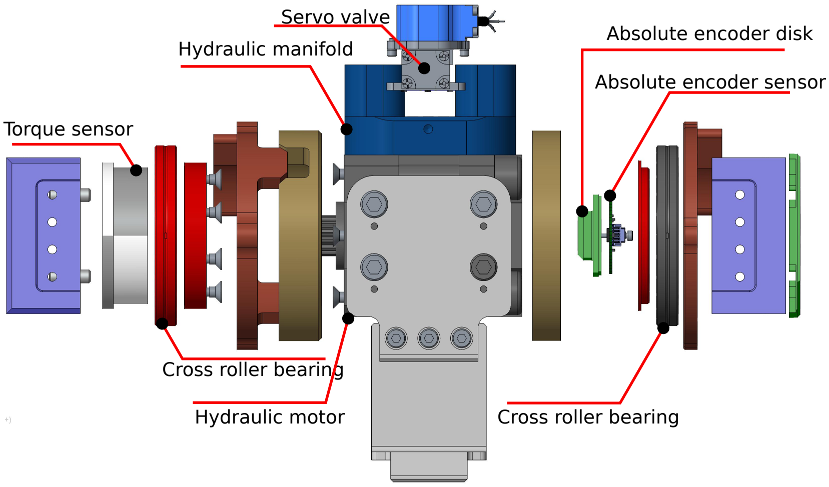
Servo valve
Hydraulic manifold
Absolute encoder disk
Absolute encoder sensor
Torque sensor
Cross roller bearing
Hydraulic motor
Cross roller bearing

(b) Shoulder Flexion/Extension (SFE) joint's CAD mechanical assembly in exploded view.

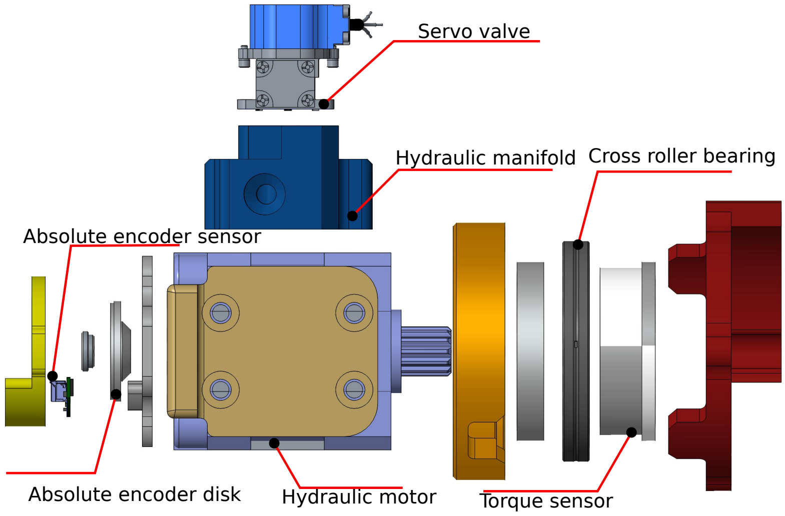
Servo valve
Hydraulic manifold
Cross roller bearing
Absolute encoder sensor
Absolute encoder disk
Hydraulic motor
Torque sensor

(c) Humerus Rotation (HR) joint's CAD mechanical assembly in exploded view.

Figure 4.3: The shoulder joints, CAD mechanical assembly in exploded view.

4.2.1 Shoulder Design ($3DoF$)

The $3DoF$ shoulder joint is of particular interest since it defines reachability in 3D work space and connects with the torso of a quadruped robot. The shoulder joints shown in Fig. 4.2 are actuated by hydraulic motors composing a spherical joint with axes intersecting through the same point. The benefit of using hydraulic motors for the shoulder joint is to ensure compact design and achieve the required joint range-of-motion and torque. Another advantage of this design is to keep the actuator masses closer to the robotic arm base link. This results in lower inertia introduced by shoulder links.

The SAA joint is the first joint in the chain. It moves the robotic arm in a horizontal or the x-y plane of the robotic arm base link (see Fig. 4.2). The second joint is SFE which is responsible to move the robotic arm in the z-x plan of with respect to its base link. Meanwhile, the third joint HR rotates in the y-z plan (when SFE and SAA joint angles are zero). The mechanical components of the (a) SAA, (b)SFE, and (c)HR are shown in Fig. 4.3. The SAA joint is actuated by a single vane hydraulic motor. It provides a constant torque of $126Nm$ at $20[MPa]$ and range-of-motion $270[deg]$ (See Table. 4.2). The SFE and HR joints are actuated by similar double vane hydraulic motor. Its provides a constant torque $120Nm$ at $20[MPa]$ and $100[deg]$ range-of-motion.

The hydraulic flow is controlled by a servo valve and custom-designed manifold is used to route oil to each chamber of the hydraulic motor. Each designed manifold is compact, light-weight and modular (see Section 4.3 for further detailss). Each shoulder joint is equipped with a custom-designed torque sensor and a 19-bits absolute position sensor to measure each joint position.

4.2.2 Elbow design (1DoF)

This section describes the elbow design called Elbow Flexion/Extension (EFE). This joint is the forth in the chain. It is actuated by an asymmetric hydraulic cylinder that provide $F_{4,ext} = 4021N$ and $F_{4,ret} = 3014N$ forces at $20[MPa]$. The F_{ext} and F_{ret} are the forces produced by the cylinder when extending or retracting:

$$\begin{aligned} F_{4,ext} &= PA_p, \\ F_{4,ret} &= PA_a \end{aligned} \tag{4.1}$$

where P is working pressure, A_p is piston area and A_a is annulus area.

A specialized mechanism is designed to convert cylinder linear velocity/forces to angular velocity/torque. The mechanism link lengths are selected by performing an optimisation process to match the required torque profiles given the constraint over minimum and maximum joint range-of-motion and cylinder length. In order to acquire optimized link lengths, I have to drive a kinematic relation between elbow cylinder linear and joint angular velocities,

$$\left(\frac{\partial x_4}{\partial \theta_4}\right) \tag{4.2}$$

To convert cylinder force $F_{4,*}$ into joint torque $\tau_{4,*}$:

$$\tau_{4,*} = \left(\frac{\partial x_4}{\partial \theta_4}\right) F_{4,*} \tag{4.3}$$

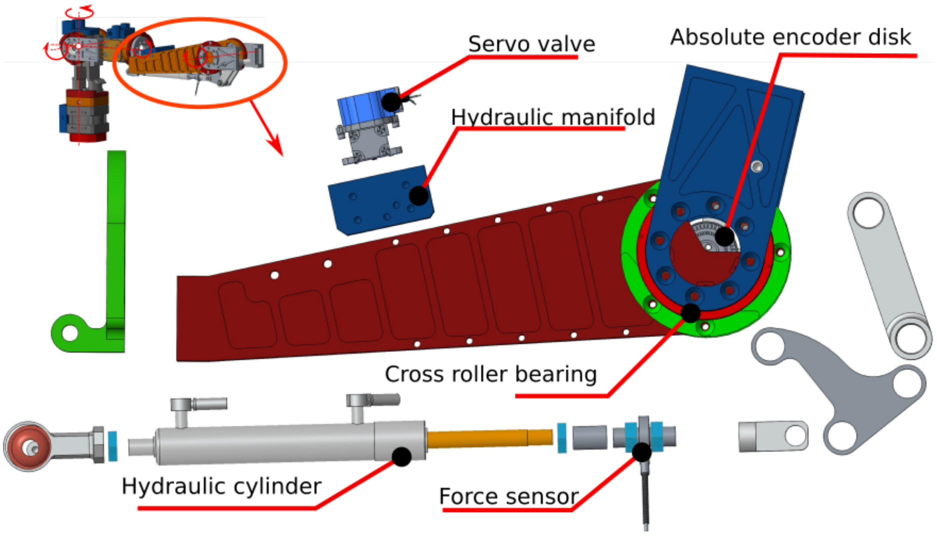
Servo valve
Absolute encoder disk
Hydraulic manifold
Cross roller bearing
Hydraulic cylinder
Force sensor

Figure 4.4: The elbow joint CAD mechanical assembly in exploded view.

To this end, the rest of this section is dedicated to derive the kinematics of elbow joint's mechanism. I synthesised a four bar linkage mechanism for EFE joint to achieve a required joint range-of-motion and output torque. This mechanism is inspired by an excavator bucket joint, where an extra link (labelled as c_6) is added between the cylinder attachment and linkage as shown in Fig. 4.5.

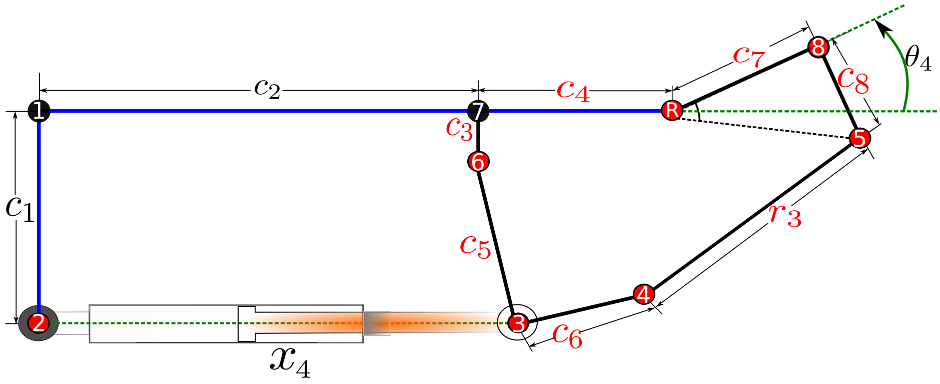
c_2
c_4
c_7
θ_4
c_8
1
7
R
8
5
c_3
6
c_1
c_5
r_3
4
2
3
c_6
x_4

Figure 4.5: Schematic of the elbow joint mechanism to map cylinder motion into elbow joint motion, eventually linear cylinder force to elbow joint torque. All the red nodes (e.g, (2),(3),(4),(5),(6),(8) and (R)) are free to rotate along their axis and black nodes (e.g, (1) and (7)) are fixed within mechanical constraints.

4.2.2.1 Kinematics of Elbow Joint's Mechanism

In order to find a direct relation between cylinder and joint velocity, I required to find a relation between cylinder x_4 length given a joint angle θ_4. The schematic presented in Fig. 4.6 allows to defined the geometric relation:

$$\psi_8(\theta_4) = \pi - \psi 2 - \psi 7 + \theta_4. \tag{4.4}$$

Considering $\triangle(6R5)$, I defined

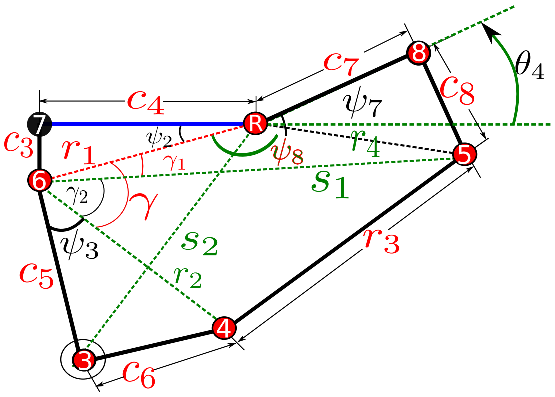
c_7
8
θ_4
c_4
7
R
c_8
ψ_7
c_3
r_1
ψ_2
γ_1
ψ_8
r_4
5
6
s_1
γ_2
γ
ψ_3
s_2
r_3
c_5
r_2
4
3
c_6

Figure 4.6: It is a close-up of Fig. 4.5 schematic with respect to node (7), (6), (3), (4), (5), (8) and (R)

$$s_1(\theta_4) = \sqrt{{r_1}^2 + {r_4}^2 - 2\, r_1\, r_4\, \cos\left(\psi_8(\theta_4)\right)} \tag{4.5}$$

where, $\psi_2 = \arctan\left(\frac{c_3}{c_4}\right)$, $\psi_7 = \arctan\left(\frac{c_8}{c_7}\right)$, $r_1 = \sqrt{{c_3}^2 + {c_4}^2}$, and $r_4 = \sqrt{{c_7}^2 + {c_8}^2}$. Now using $\triangle(6R5)$ and $\triangle(564)$ shown in Fig. 4.6, I defined $\gamma(\theta_4)$:

$$\gamma(\theta_4) = \arccos\left(\frac{s_1(\theta_4)^2 + {r_1}^2 - {r_4}^2}{2\, s_1(\theta_4)\, r_1}\right) + \arccos\left(\frac{s_1(\theta_4)^2 + {r_2}^2 - {r_3}^2}{2\, s_1(\theta_4)\, r_2}\right) \tag{4.6}$$

The schematic close-up shown in Fig: 4.7, allows to define following geometric relation:

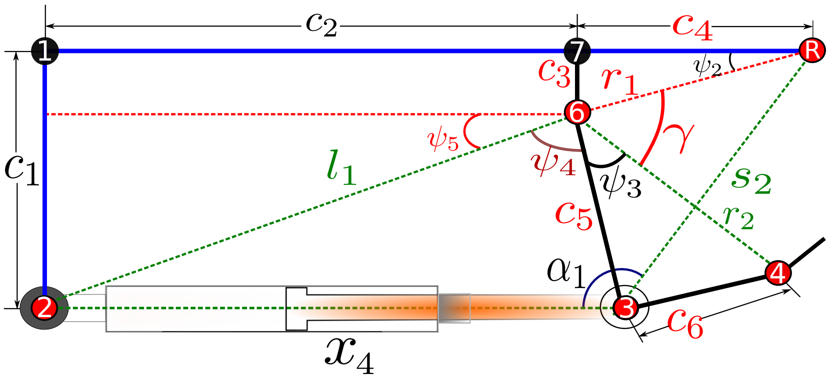
c_2
c_4
1
7
R
c_3
r_1
ψ_2
6
c_1
ψ_5
γ
l_1
ψ_4
ψ_3
s_2
c_5
r_2
α_1
4
2
3
c_6
x_4

Figure 4.7: Schematic close-up of Fig. 4.5 between node (1), (2), (3), (4), (6), (7) and (R).

$$\psi_4(\theta_4) = \frac{3}{2}\pi - \psi_6 - \psi_3 - \psi_5 - \gamma(\theta_4) \tag{4.7}$$

where, $\psi_6 = \pi/2 - \psi_2$, $\psi_3 = \arctan\left(\frac{c_6}{c_5}\right)$, $\psi_6 = \pi/2 - \psi_2$ and $\psi_5 = \arctan\left(\frac{(c_1 - c_3)}{c_2}\right)$. $\triangle(263)$ allows to define a relation between the cylinder position (x_4) and joint angle θ_4:

$$x_4(\theta_4) = \sqrt{{c_5}^2 + {l_1}^2 - 2\, c_5\, l_1\, \cos\left(\psi_4(\theta_4)\right)} \tag{4.8}$$

Finally, differentiation (4.8) with respect to θ_4 provides a direct relation between elbow cylinder and joint velocity.

$$\frac{\partial x_4}{\partial \theta_4} = \frac{c_5\, l_1\, \sin(\psi_4(\theta_4))}{\sqrt{{c_5}^2 + {l_1}^2 - 2\, c_5\, l_1\, \cos(\psi_4(\theta_4))}} \tag{4.9}$$

4.2.2.2 Elbow Target Design Parameters and Constraints

We have to define the target design parameters for optimization. In the case of the elbow joint mechanism (presented in the previous section), the target design parameters are the following:

$$x = [c_1, c_2, c_3, c_4, c_5, c_6, c_7, c_8, r_3]. \tag{4.10}$$

These parameters are the unknown mechanism link lengths (x) that are directly related to elbow joint torque output ($\tau_{4,*}$) given a cylinder force ($F_{4,*}$) as defined in (4.3). This cylinder force to torque conversion results in a non-linear output profile. Due to fact that there is a non-linear relation between the cylinder linear and joint angular velocity (4.2), and also the amount of force produced by the hydraulic cylinder while extending or retracting (4.4). To this end, the required elbow joint torque profile is approximated as a 3^{rd} order polynomial. The polynomial $f_0(\theta_4)$ served as a base line to approximate required torque profile (with hydraulic cylinder extending (red solid line) and retracting (red dash line)), as shown in Fig. 4.8, and defined as a function of elbow joint angle θ_4:

$$f_0(\theta_4) = a_1\theta_4^3 + a_2\theta_4^2 + a_3\theta_4 + a_4, \tag{4.11}$$

where polynomial coefficients $a_{(*)}$ are solved for peak estimated required torque and given as:

$$a_{(*)} = \begin{cases} a_1 = 1.977 \\ a_2 = -28.61 \\ a_3 = 6.958 \\ a_4 = 172.8 \end{cases} \tag{4.12}$$

The remaining parameters such as (a) joint range-of-motion (θ_4), and (b) actuator stroke length (X_c) are design constraints. The constraint over required elbow joint range-of-motion is defined as:

$$q_{min_4} \leq \theta_4 \leq q_{max_4} \tag{4.13}$$

where, $q_{min_4} = 0[rad]$ and $q_{max_4} = 2.26[rad]$ are defined in Section 3.3.4.6. The selected hydraulic cylinder for elbow has total stroke length of $0.070[m]$ as given in Table. 3.10 and constraint as:

$$s_{min_4} = 0.001[m] \leq X_{c_4} \leq s_{max_4} = 0.069[m], \tag{4.14}$$

where X_{c_4} is current cylinder length as a function of joint angle θ_4. The motivation behind keeping a safety margin of $0.001[m]$ on both extremes, is to avoid internal impact on the cylinder sealing, when it is fully extended or retracted. In the next section, I will explain how to optimize these unknown design parameters to achieve desired torque output?

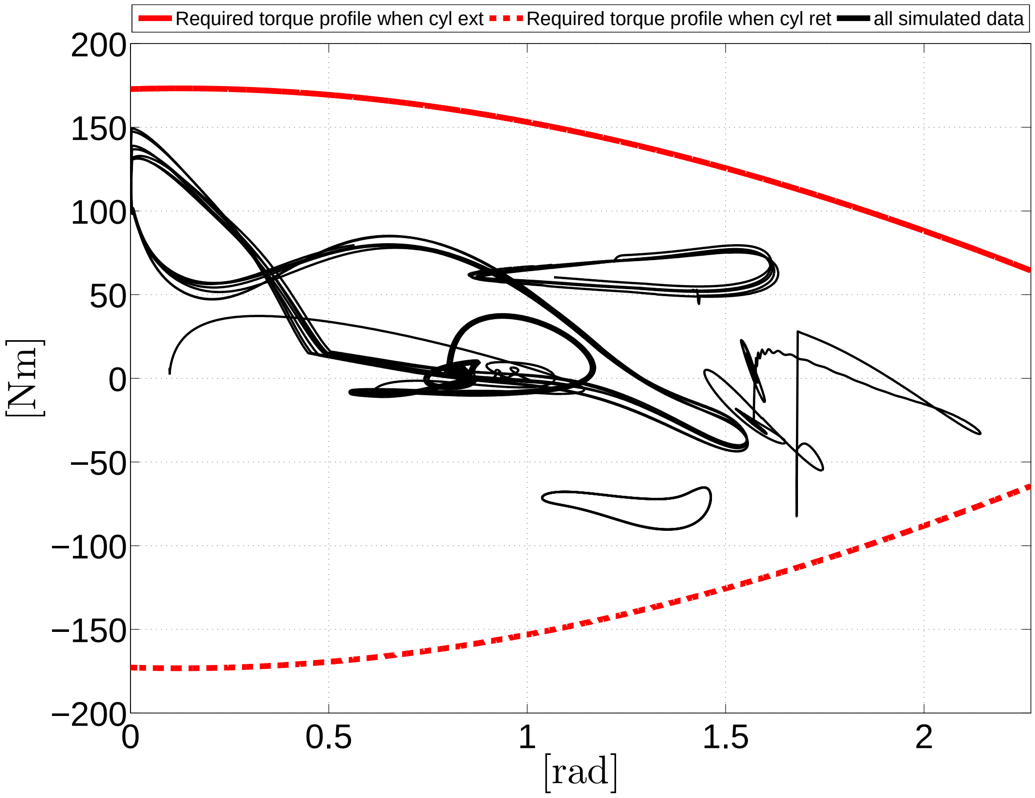

Figure 4.8: A 3^{rd} order polynomial approximation of required torque profile for elbow joint. The red solid line represent required torque when the cylinder is extending and a dash line when it is retracting. These curves are superimposed over estimated required torque acquired from simulation of representative tasks in black sold lines (see Section 3.3.4 for further details)

4.2.2.3 Elbow Joint Mechanism Optimization

The goal of the optimization problem is to find optimized design parameters (x) which minimize the error between target torque profile (f_0) and mechanism torque output (τ_4) given mechanical constraints. To this end, the object function is defined as:

$$\min_x f(x) = \sum_{\theta_4 = q_{min_4}}^{q_{max_4}} \sum_{X_{c_4} = s_{min_4}}^{s_{max_4}} (f_0(\theta_4) - \tau(\theta_4, X_{c_4}, x, F_{4,*}))^2 \tag{4.15}$$

$$\text{subject to the equality constraints} \begin{cases} s_{min_4} = 0.001[m] \text{ if } q_{min_4} = 0[rad] \\ s_{max_4} = 0.069[m] \text{ if } q_{max_4} = 2.26[rad] \end{cases} \tag{4.16}$$

$$\text{subject to the inequality constraints} \begin{cases} q_{min_4} = 0[rad] \leq \theta_4 \leq q_{max_4} = 2.26[rad] \\ s_{min_4} = 0.001[m] \leq X_{c_4} \leq s_{max_4} = 0.069[m] \end{cases} \tag{4.17}$$

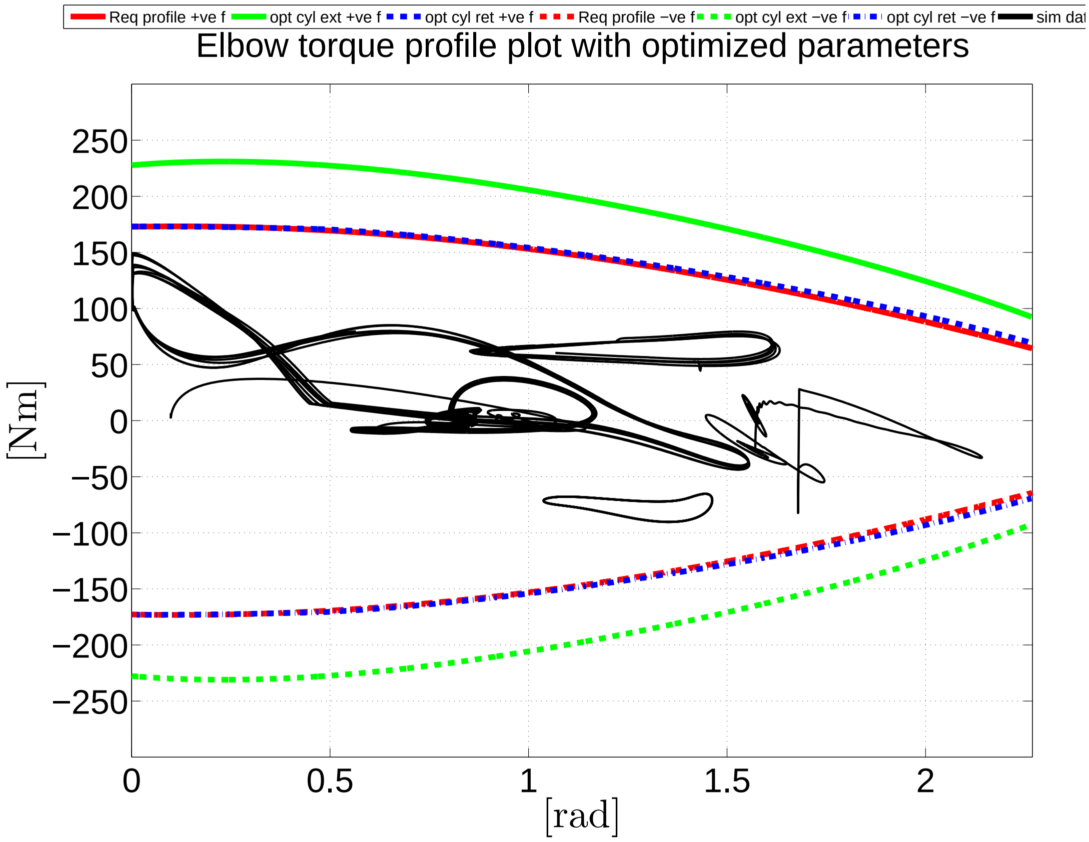

Figure 4.9: The Elbow joint torque profile with optimized design parameters. The green solid and dash line represent torque output with hydraulic cylinder extension with positive and negative force direction. The blue dash and " −.−" lines represent torque output with hydraulic cylinder retracting with positive and negative force direction. The red sold and the dash line represents target torque profile. The black sold lines represent simulated data of representative tasks.

Design parameter	Upper bound (UB) [mm]	Lower bound (LB) [mm]	Optimized values(x)[mm]
c_1	fixed	fixed	52.5
c_2	fixed	fixed	250
c_3	10	0	2
c_4	25	15	25
c_5	60	30	55
c_6	40	35	38.93
c_7	55	45	45
c_8	15	4	15
r_3	63.5	50	63.5

Table 4.4: Optimized designed parameters

Where x is a set of design parameters (4.10) that we want to optimize given minimum cylinder force. To this end, I chose the cylinder retracting force $F_{4,ret}$ as it is less then $F_{4,ext}$ (4.4). Similar to [Khan et al., 2015], I used Matlab function "fmincon" to

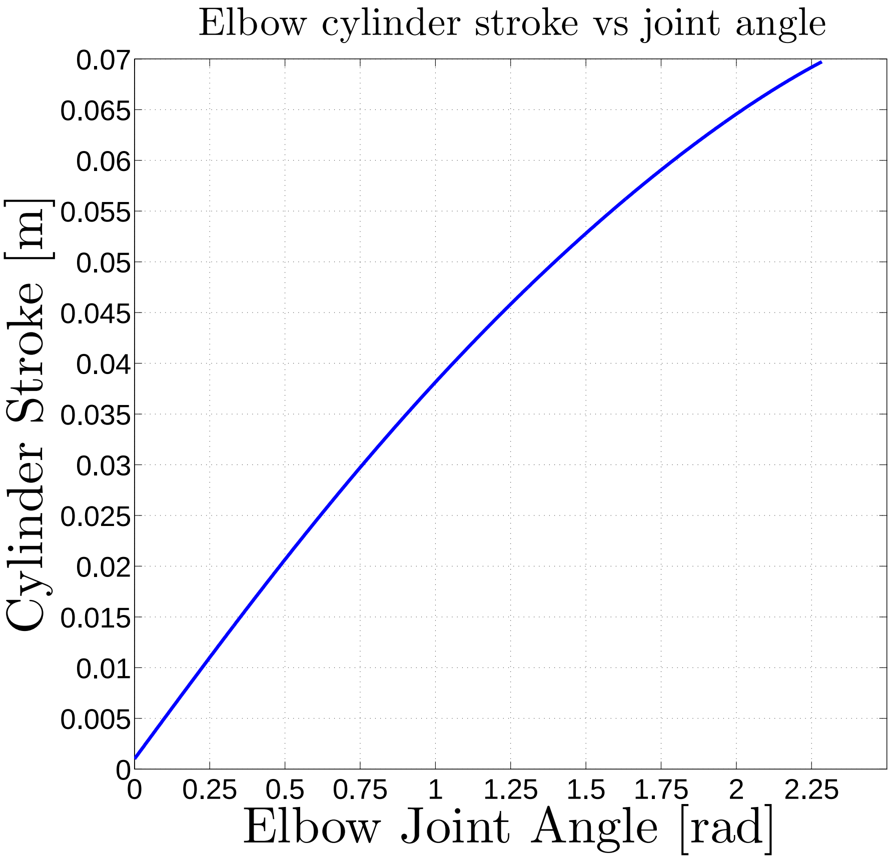

Figure 4.10: The elbow cylinder stroke vs joint angle

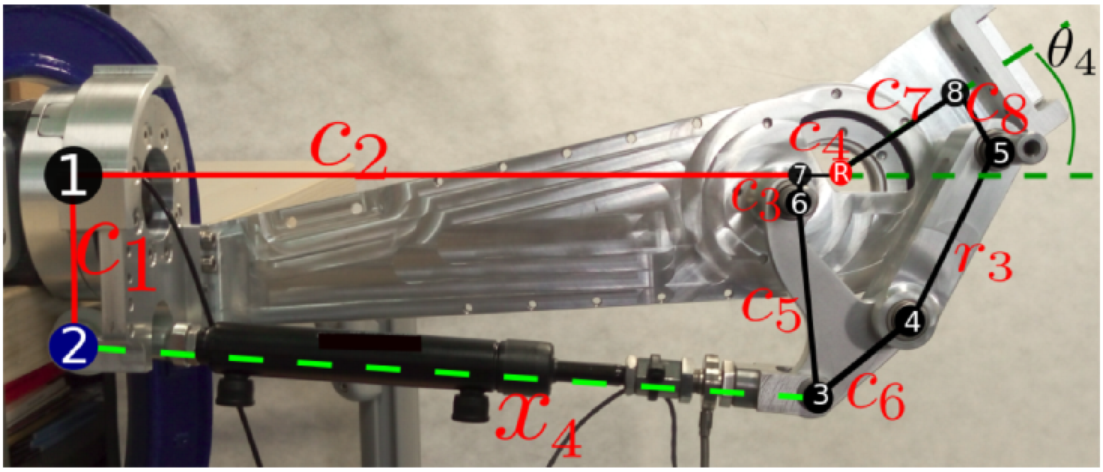

Figure 4.11: The real hardware implementation of the elbow joint mechanism with optimized link lengths. The c_1 is link is connecting node (1) to (2), c_2 is a link between node (1) and (7), c_3 between node (7) and (6), c_4 is connecting node (7) to node (R), c_5 is a physical link connection between node (6) and (3), c_6 is a physical link between node (3) and (4), c_7 is connecting node (R) to (8), c_8 is a connection between node (5) to (8), r_3 is a physical link between node (4) and (5), x_4 is the elbow cylinder length and θ_4 is the elbow joint angle.

minimize object function (4.15). We set upper and lower bounds over design parameters to ensure a compact mechanism design (see Table. 4.4). I fixed the parameter c_1 and c_2, to ensure upper arm length to be within kinematic limits and estimated based on mock-up design. The optimizer finds a set of optimal design parameters that achieve the objective function (4.15) and satisfy the constraints defined in (4.16) and (4.17). The optimized design parameters are given in Table. 4.4. The optimized torque output profile is shown in Fig. 4.9 which satisfy constraints given in (4.16) and (4.17), also as shown Fig. 4.10. Finally, the implementation of optimized four-bar linkage mechanism is shown in Fig. 4.11.

4.2.3 Wrist design (2DoF)

The Wrist Rotation (WR) and Wrist Flexion/Extension (WFE) are the last two joints in the kinematic chain of HyArm. The wrist joints play an important role in determining end-effector position and orientation with less effort compared to shoulder joints. The rest of this section describes the mechanical design of the HyArm wrist.

4.2.3.1 Wrist Rotation

The Wrist Rotation (WR) joint is actuated by a single vane hydraulic motor. It provides a constant torque of $60Nm$ at $20[MPa]$ and a total range-of-motion $270[deg]$ (See Table. 4.2). Similar to the shoulder's joints, WR joint is equipped with torque and position sensor, hydraulic servo valve and manifold. The mechanical components of the WR are shown in Fig. 4.12.

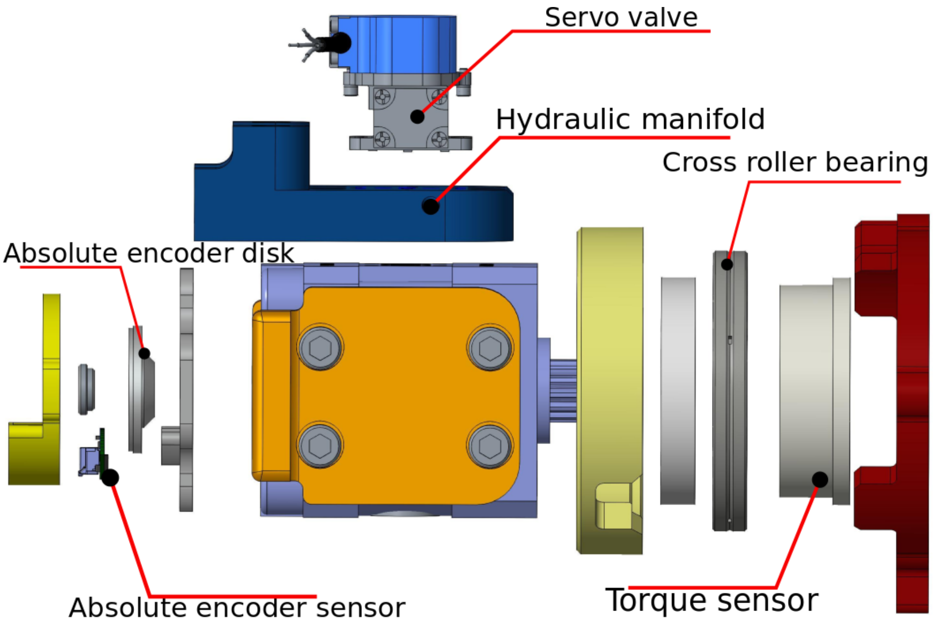

Figure 4.12: Wrist Rotation,WR

4.2.3.2 Wrist Flexion/Extension

Finally, the last joint in the chain, WFE. Similar to the elbow joint, the WFE is also actuated by an asymmetric hydraulic cylinder and equipped with servo valve, manifold, and force and position sensors as shown in Fig. 4.13. A standard lever mechanism is

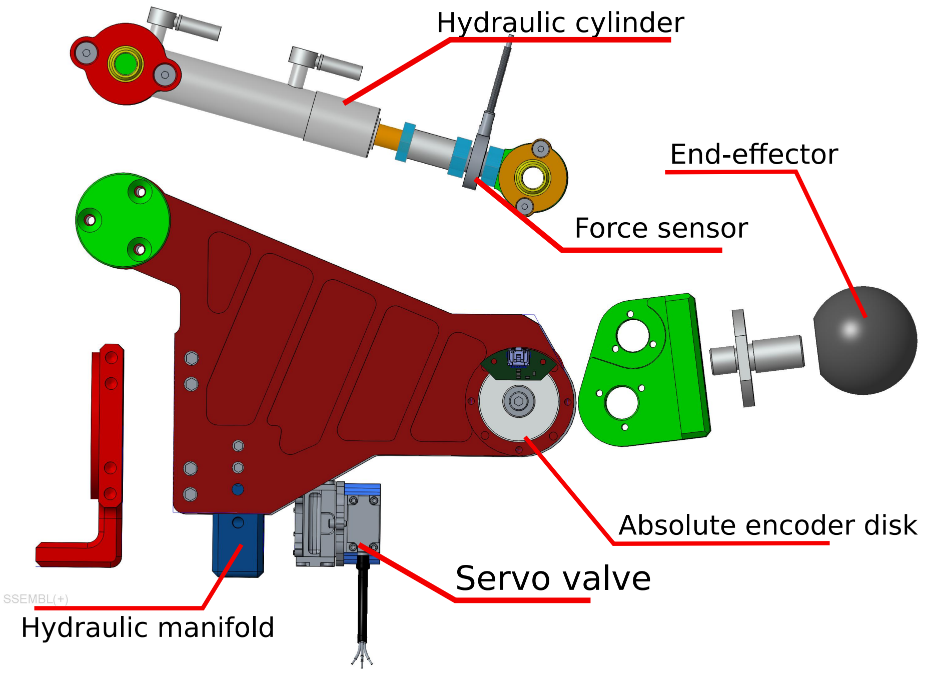
Hydraulic cylinder
End-effector
Force sensor
Absolute encoder disk
Servo valve
SSEMBL(+)
Hydraulic manifold

Figure 4.13: Wrist Flexion/Extension (WFE)

designed for WFE to acquire the required joint torque output and range-of-motion. The optimization approach described above is used to select the mechanism link lengths. In order to acquire optimized link lengths for WFE, I defined the kinematic relation between wrist cylinder linear and joint angular velocities $\left(\frac{\partial x_6}{\partial \theta_6}\right)$. To convert cylinder force F_6 into joint torque τ_6:

$$\tau_6 = \left(\frac{\partial x_6}{\partial \theta_6}\right) F_6 \tag{4.18}$$

This section describes the synthesis of WFE joint mechanism. The mechanism

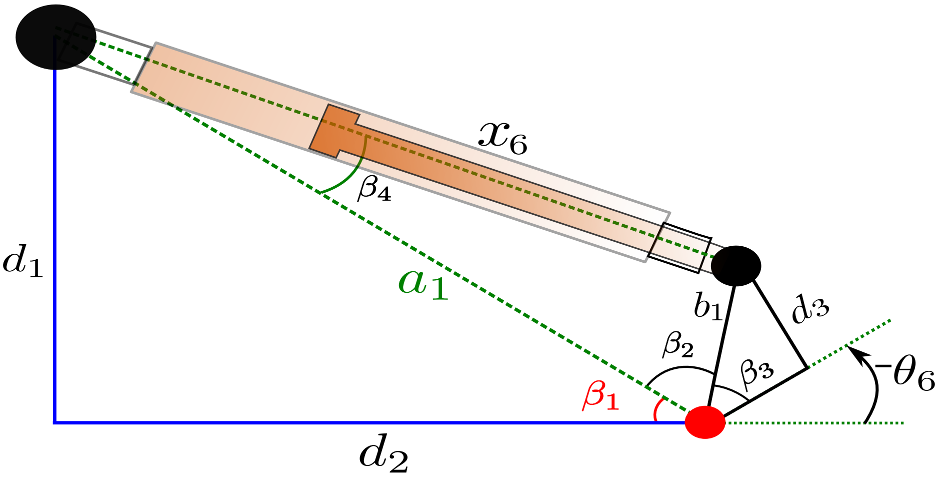
x_6
β_4
d_1
a_1
b_1
d_3
β_2
β_3
$-\theta_6$
β_1
d_2

Figure 4.14: Geometry of WFE joint angle θ_6 with essential mechanical links.

schematic presented in Fig. 4.14 were used to define the geometric relations,

$$\beta_2(\theta_6) = \pi - \beta_1 - \beta_3 - \theta_6, \tag{4.19}$$

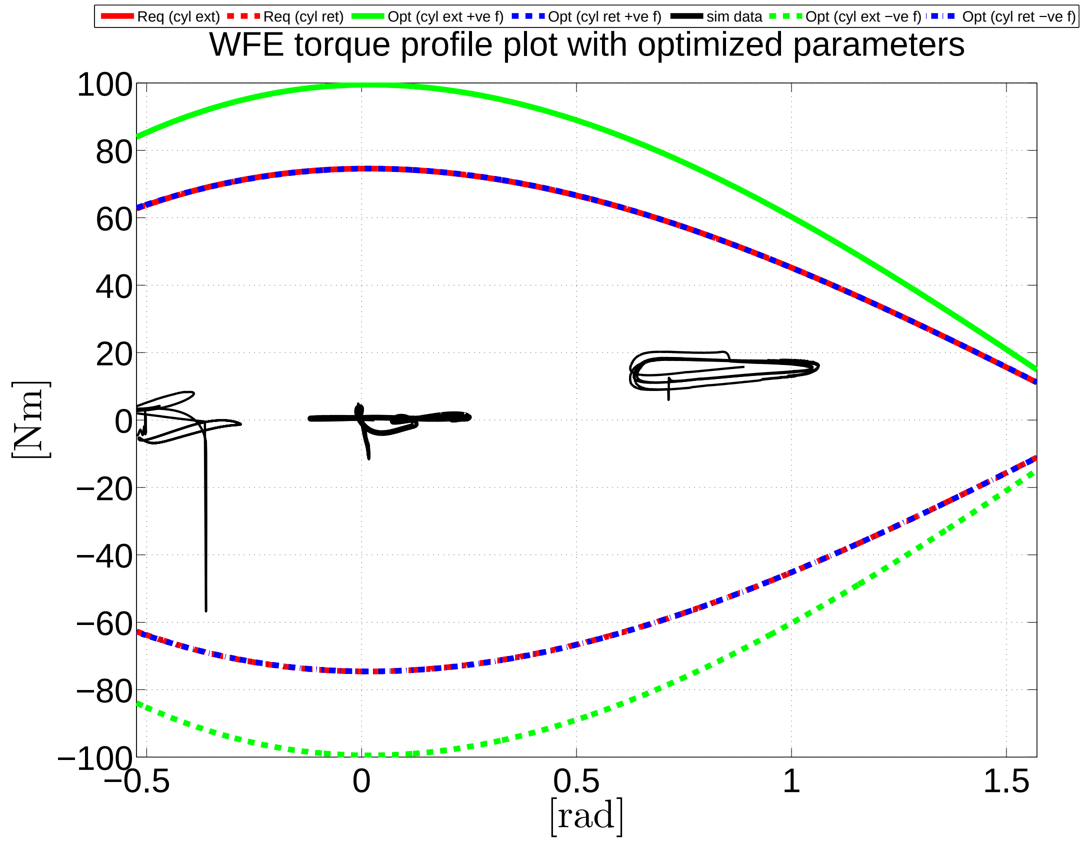

Figure 4.15: The WFE joint torque profile with optimized design parameters. The green solid and dash line represent torque output with hydraulic cylinder extension with positive and negative force direction. The blue dash and " −.− " lines represent torque output with hydraulic cylinder retracting with positive and negative force direction. The red sold and the dash line represent target torque profile. The black solid lines describes the simulated data of representative tasks.

that leads to a relation between WFE cylinder length x_6 and joint angle θ_6, i.e.

$$x_6(\theta_6) = \sqrt{{a_1}^2 + {b_1}^2 - 2\, a_1\, b_1\, \cos\left(\beta_2(\theta_6)\right)} \tag{4.20}$$

where, $a_1 = \sqrt{{d_1}^2 + {d_2}^2}$, $\beta_1 = \arctan(\frac{d_1}{d_2})$ and $\beta_3 = \arctan(\frac{d_3}{d_1})$.

Taking partial differentiation of (4.20) with respect to θ_6 provides a direct relation between wrist cylinder and joint velocities:

$$\frac{\partial x_6}{\partial \theta_6} = \frac{a_1\, b_1\, \sin\left(\beta_2(\theta_6)\right)}{\sqrt{{a_1}^2 + {b_1}^2 - 2\, a_1\, b_1\, \cos\left(\beta_2(\theta_6)\right)}} \tag{4.21}$$

The unknown design parameter for WFE joints are:

$$\Upsilon = [d_1, d_2, d_3, b_1]. \tag{4.22}$$

The required WFE joint torque profile is approximated as a 3^{rd} order polynomial

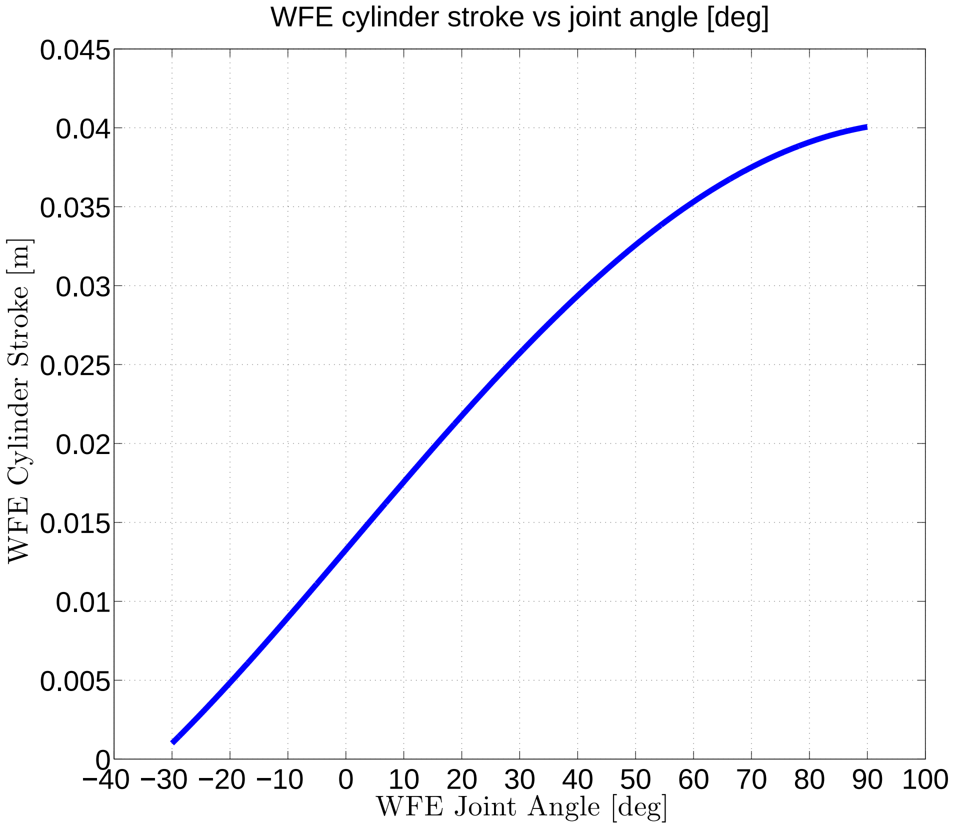

Figure 4.16: The WFE cylinder stroke vs joint angle

$\rho_0(\theta_6)$ as shown in Fig. 4.17. and defined as function θ_6:

$$\rho_0(\theta_6) = e_1\theta_6^3 + e_2\theta_6^2 + e_3\theta_6 + e_4, \tag{4.23}$$

where, polynomial coefficients $e_{(*)}$ are solved for peak estimated required torque and given as:

$$e_{(*)} = \begin{cases} e_1 = 7.081 \\ e_2 = -37.52 \\ e_3 = 1.059 \\ e_4 = 74.57 \end{cases} \tag{4.24}$$

The constraint over WFE joint range-of-motion and cylinder stroke length are defined as:

$$q_{min_6} = -0.5[rad] \leq \theta_6 \leq q_{max_6} = 1.57[rad] \tag{4.25}$$

$$s_{min_6} = 0.001[m] \leq X_{c_6} \leq s_{max_6} = 0.039[m]. \tag{4.26}$$

Where as the WFE joint cylinder has total stroke length of $0.040[m]$ as given in Table. 3.10. Similar to elbow joint, I kept a safety margin of $0.001[m]$ on both extreme. The object function for WFE is defined as:

$$\min_{\Upsilon} f(\Upsilon) = \sum_{\theta_6=q_{min_6}}^{q_{max_6}} \sum_{X_{c_6}=s_{min_6}}^{s_{max_6}} \left(f_0(\theta_6) - \tau(\theta_6, X_{c_6}, \Upsilon, F_{6,ret})\right)^2 \tag{4.27}$$

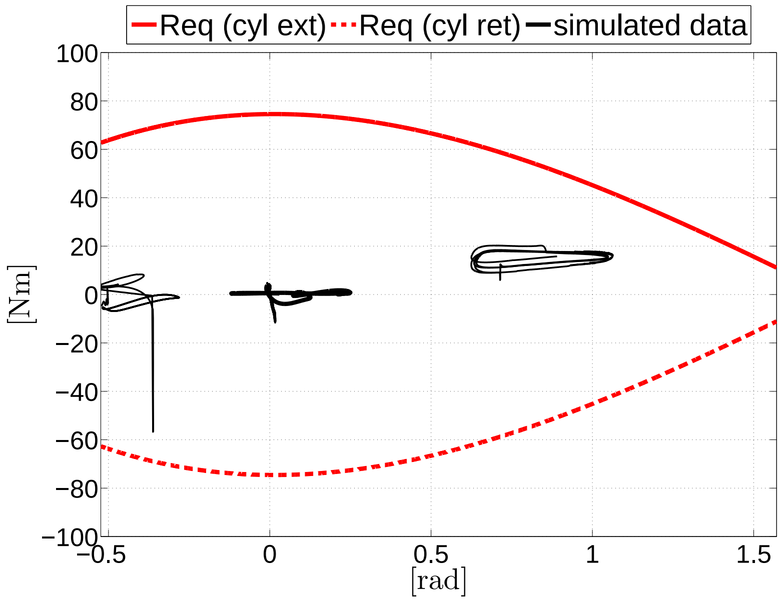

Figure 4.17: The approximated required torque profile for WFE joint, is shown in red solid and dash lines when cylinder is extending and retracting, respectively. These curves are superimposed over estimated required torque acquired from simulation of representative tasks in black sold lines (see Section 3.3.4 for further details)

$$\text{subject to the equality constraints} \begin{cases} s_{min_6} = 0.001[m] \text{ if } q_{min_6} = -0.52[rad] \\ s_{max_6} = 0.039[m] \text{ if } q_{max_6} = 1.57[rad] \end{cases} \tag{4.28}$$

$$\text{subject to the inequality constraints} \begin{cases} q_{min_6} = -0.52[rad] \leq \theta_6 \leq q_{max_6} = 1.57[rad] \\ s_{min_6} = 0.001[m] \leq X_{c6} \leq s_{max_6} = 0.039[m] \end{cases} \tag{4.29}$$

Similar to elbow mechanism optimization, I used the WFE cylinder retracting force $F_{6,ret}$. In case of WFE, I let optimizer to select link lengths without any bounds. The optimized Υ link lengths are given in Table. 4.5, which achieved the object function (4.27), within defined constraints given in (4.28) and (4.29). The optimized WFE joint torque profile shown in Fig. 4.15, that satisfy constraints as shown in Fig. 4.16.

Design parameter	Optimized values(Υ)[mm]
d_1	65.08
d_2	146.15
d_3	24
b_1	24.75

Table 4.5: Optimized designed parameters for WFE joint

4.3 Hydraulic Circuit

This section discusses the hydraulic circuit schematics for HyArm. The hydraulic power is supplied to HyArm through two flexible hoses which can be connected directly to either hydraulic pump or HyQ. Figure. 4.18 shows the hydraulic circuit components: An accumulator to smooth out pressure ripples and provide extra flow during fast variations in hydraulic flow, and pressure gauge to measure supplied pressure to HyArm. Each cylinder and motor: hydraulic flow between their respective chambers is controlled by a servo-valve which is directly attached to the hydraulic manifold. We designed compact hydraulic manifolds for each actuator which route hydraulic fluid flow between each actuator and were validated by FEM analysis. Each hydraulic manifold (a) takes supply/return fluid flow from the preceding actuator or main supply sources, (b) then routes it to the respective servo valve, (c) which routes to each actuator chamber, and (d) to the next actuator in the chain. These hydraulic manifolds are shown in Fig. 4.19 with their respective joint labels.

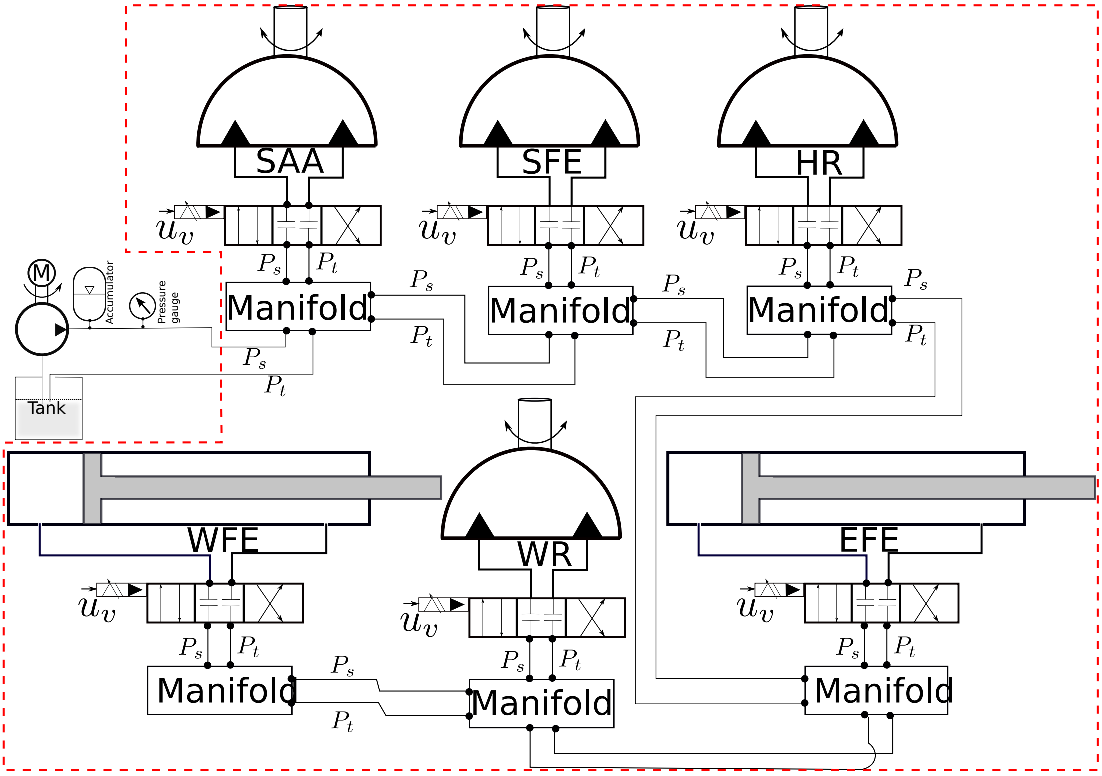

Figure 4.18: Hydraulic circuit schematic for HyArm. The main hydraulic power is supplied through two flexible hoses which can be connect directly to either hydraulic pump or HyQ.

4.4 Electronics and Control System Layout

The electronics and control system layout for HyArm is summarized in Fig. 4.20. The electronics system consists of two arm electronic units connected in series with a valve electronic unit. The EtherCat bus enables real time and high speed communication between each unit. These electronic units are physically connecting through EtherNet cables which also supply power to each unit. Each arm unit collects input signals from

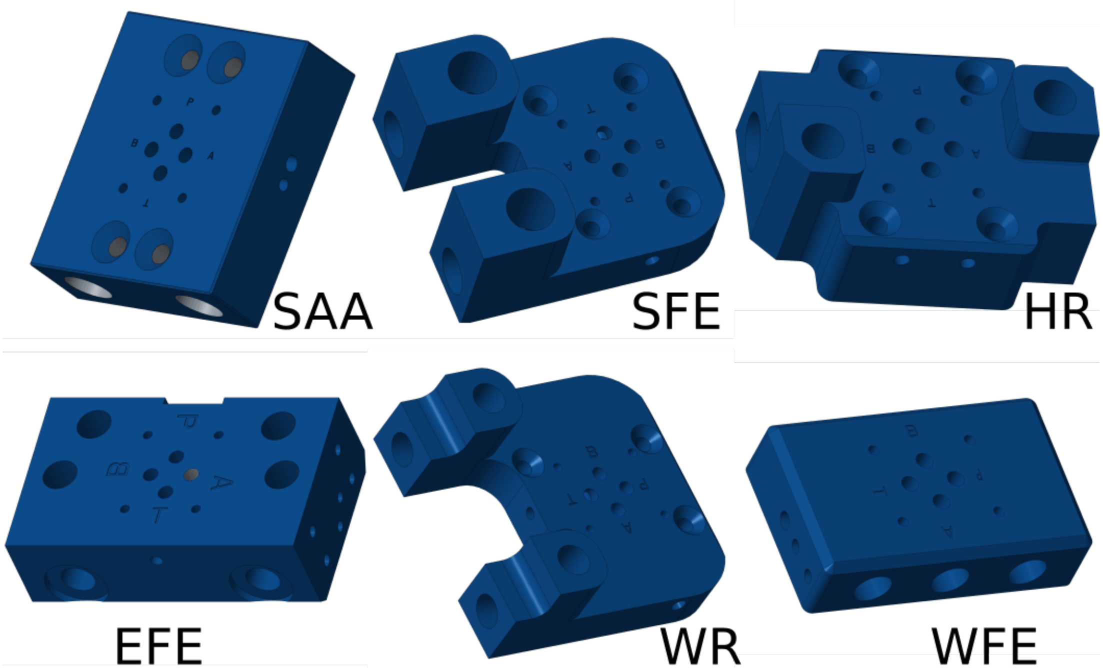

Figure 4.19: Custom designed compact hydraulic manifolds for HyArm actuators.

three 19 bit absolute position encoders, a force and two custom designed torque sensors. The valve unit is an interface between servo valve, arm units and real time control PC. It amplifies servo signal coming from a low-level controller to hydraulic valves. When HyArm is not attached to HyQ, an external power supply provides 24 volts to the valve electronic unit. The control PC and valve electronic unit are the only external units which are not integrated inside HyArm's mechanical structure.

The control system architecture is based on a single centralized control PC that supervises the entire low and high level control and I/O communication. The software used is the SL [Schaal, 2006] (see Section 3.3 for further details) which runs the real time simulation and contains the control architecture. The high level control and trajectory planner is implemented in task servo. The low level controller is implemented in motor servo (runs at $1KHz$) which can switch between simulation or real hardware interface. This feature allows to simulate the robot behaviours in simulation (environment) and then later on the real robot, without any modification in task servo. To integrate the arm (electronically) with a mobile platform, it only requires to connect with HyQ (on-board) Control PC through EtherCat network switch and provide 24-volts.

4.5 Hardware Integration of HyArm with HyQ

This section presents hardware integration of HyArm with HyQ in single and dual-arm configurations. The shoulder base attachment study in the previous chapter provided optimized design parameters which are used for dual-arm integration in Section 4.5.2. As an intermediated step, I studied and proposed a single arm configuration with HyQ as described below.

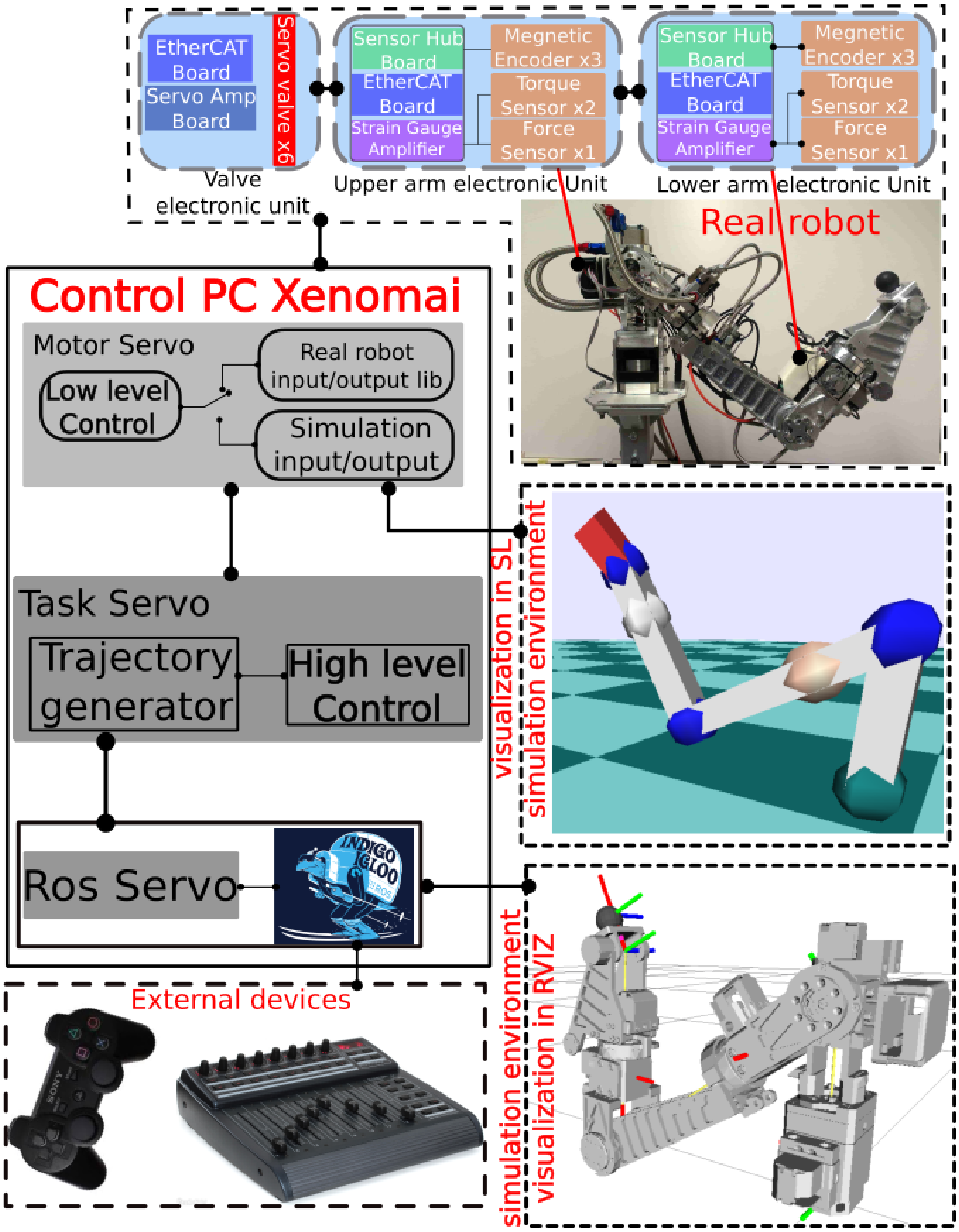
EtherCAT Board
Servo Amp Board
Servo valve x6
Valve electronic unit
Sensor Hub Board
EtherCAT Board
Strain Gauge Amplifier
Megnetic Encoder x3
Torque Sensor x2
Force Sensor x1
Upper arm electronic Unit
Sensor Hub Board
EtherCAT Board
Strain Gauge Amplifier
Megnetic Encoder x3
Torque Sensor x2
Force Sensor x1
Lower arm electronic Unit
Real robot
Control PC Xenomai
Motor Servo
Low level Control
Real robot input/output lib
Simulation input/output
Task Servo
Trajectory generator
High level Control
Ros Servo
INDIGO IGLOO
visualization in SL
simulation environment
simulation environment
visualization in RVIZ
External devices

Figure 4.20: Electronics and control system layout diagram for HyArm.

4.5.1 Single Arm Configuration

This section presents system integration of a single manipulator (HyArm) and mobile platform (HyQ). The manipulator can be attached to the front-middle of the HyQ either in a elbow-down or elbow-up configuration. The placement of the manipulator in front-middle has the advantage that the weight of HyArm is shared by both front legs, but a drawback is that the weight distribution of the mobile platform gets unbalance. In the next chapter I will address this problem in detail. Given HyArm's joint range of motion, I considered three different attachment configurations as shown in Fig. 4.21, 4.22, and 4.23.

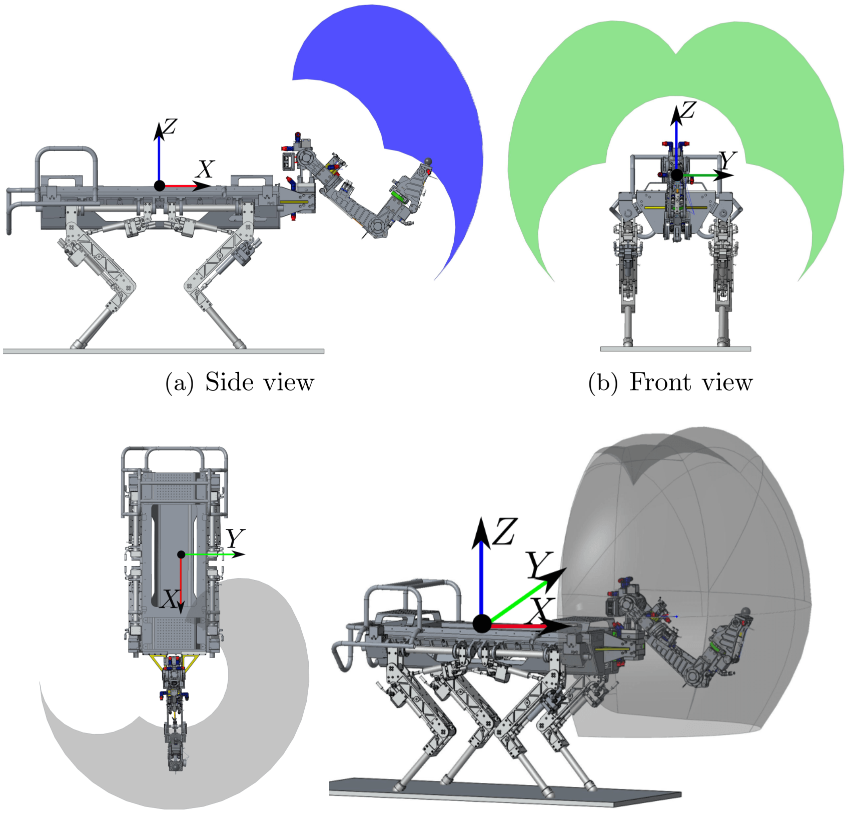

(a) Side view (b) Front view

(c) Top view (d) 3D view

Figure 4.21: Various views of the arm workspace in an elbow-down configuration 1 with the arm base aligned with Z-axis of the mobile base frame: (a) X-Z plane, (b) Y-Z plane, (c) X-Y plan and (d) 3D view.

4.5.1.1 Single Arm Elbow-down Configuration

We considered two different elbow-down configurations for HyArm to attach with HyQ so called elbow-down configurations 1 and 2. The elbow-down configuration 1 is shown in Fig. 4.21; the manipulator is base link aligned with the Z-axis of the HyQ base frame. This configuration provide a workspace in front and above the HyQ trunk. This configuration is suitable for opening a door or reaching the target object above the robot's height. However, this configuration does not provide a possibility to perform tasks such as balance assistance (acting as a fifth leg) or debris removal from the ground.

The configuration 2 shown in Fig. 4.22 is the manipulator base link rotated at $90[deg]$ with respect to the Z-axis of the HyQ base frame. In this configuration, the manipulator workspace partially overlaps with only the front left leg. This configuration provided ground reachability, but there is an inconsistency in the manipulator workspace between the left and right sides of the mobile platform.

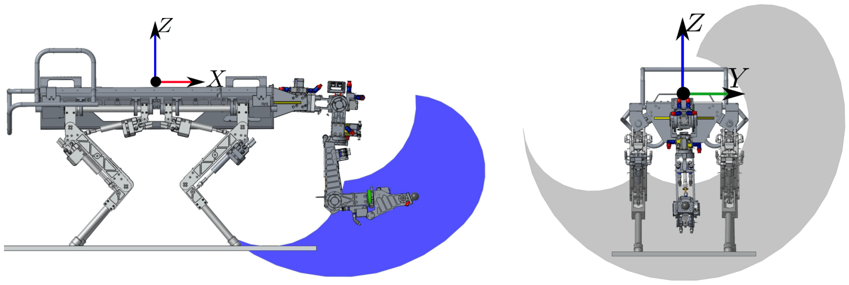

(a) Side view (b) Front view

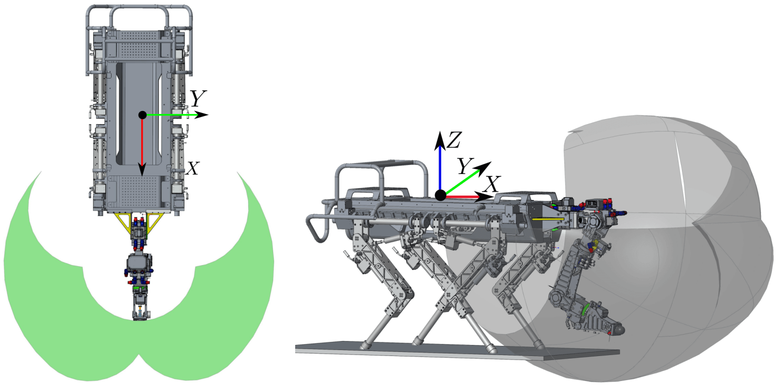

(c) Top view (d) 3D view

Figure 4.22: Various views of the arm workspace in an elbow-down configuration 2 with the arm base rotated 90[deg] w.r.t X-axis of the mobile base frame: (a) X-Z plane, (b) Y-Z plane, (c) X-Y plan and (d) 3D view.

4.5.1.2 Single Arm Elbow-up Configuration

The elbow-up configuration is shown in Fig. 4.23, where the arm base link is rotated at 180[deg] with respect to the mobile robot X-axis. This configuration allows the manipulator to achieve a uniform workspace in front, below and above the base robot trunk. We selected this configuration for our experimental studies. In this configuration, the manipulator can be used to provide balance assistance for locomotion by acting as a fifth leg or performing manipulation tasks such as removing obstacles, opening a door or simple picking and placing. The real hardware integration is shown in Fig. 4.24. The hydraulic and electric power is supplied from HyQ to HyArm. The electronics are connected to on-board real-time control PC through an EtherCat network. The on-board control PC is running real-time Xenomai to communicate with the EtherCat network and SL Software to control (see Section 4.4 for further details).

4.5.2 Dual Arm Configuration

Based on optimization results presented in Section 3.3.3, I attached a dual-arm system with HyQ as shown in Fig.4.25.

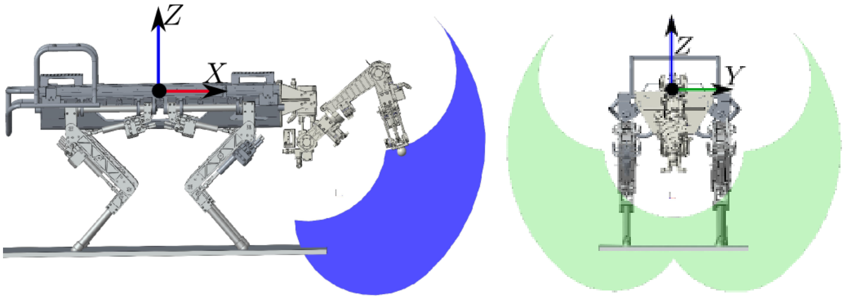

(a) Side view (b) Front view

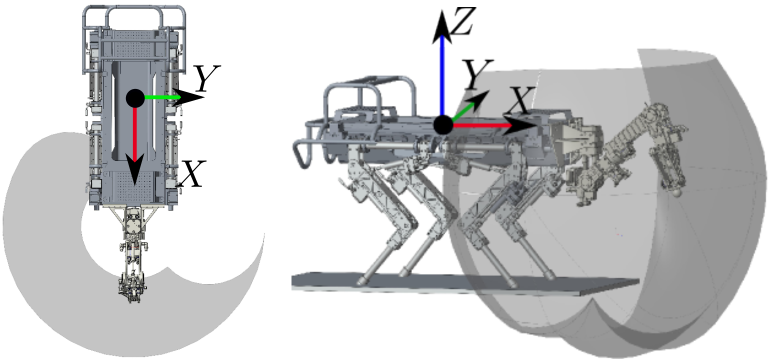

(c) Top view (d) 3D view

Figure 4.23: Various views of the arm workspace in an elbow-up configuration with the arm base rotated 180[deg] w.r.t X-axis of the mobile base frame: (a) X-Z plane, (b) Y-Z plane, (c) X-Y plan and (d) 3D view.

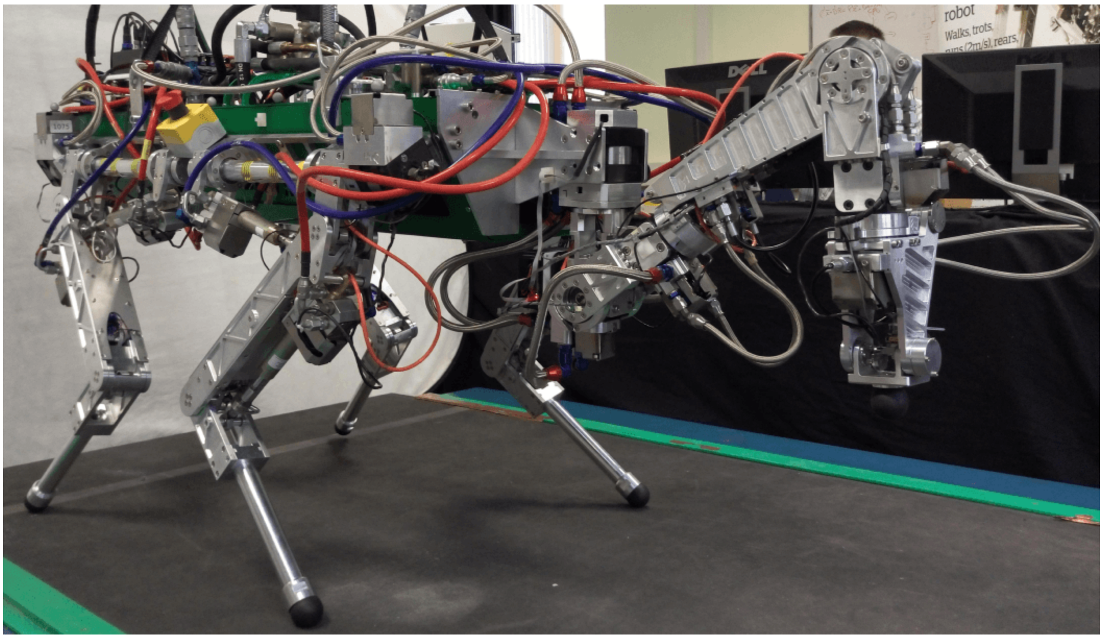

Figure 4.24: Picture of IIT's HyQ robot [Semini et al., 2011] with the new hydraulic manipulator [Rehman et al., 2015] attached to its front creating a multi-legged mobile manipulator.

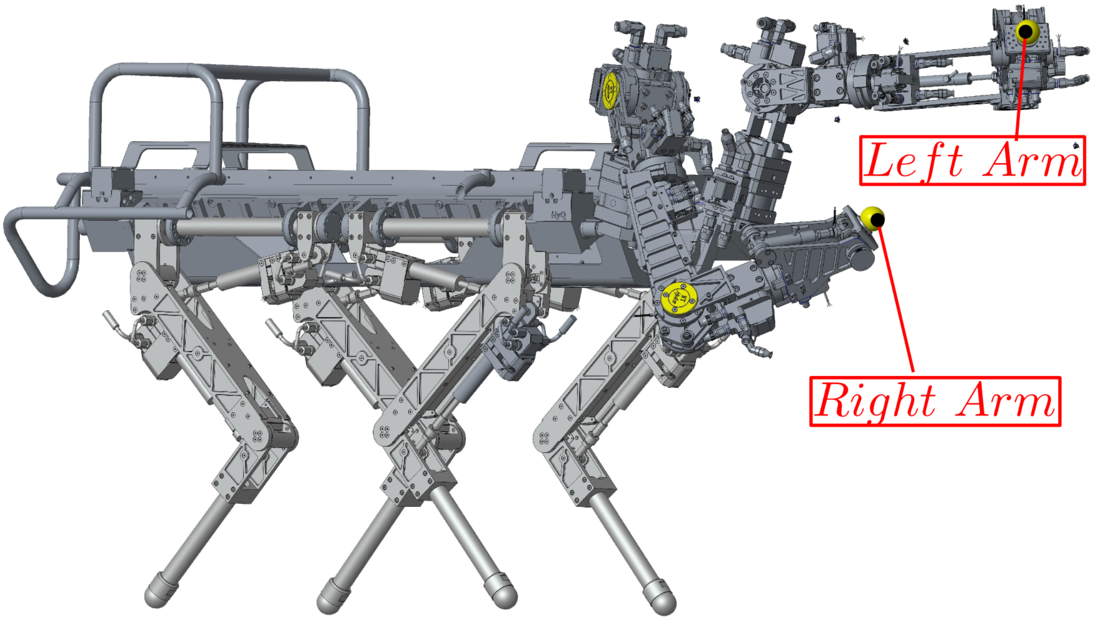
Left Arm
Right Arm

(a) The dual-arm system during operation

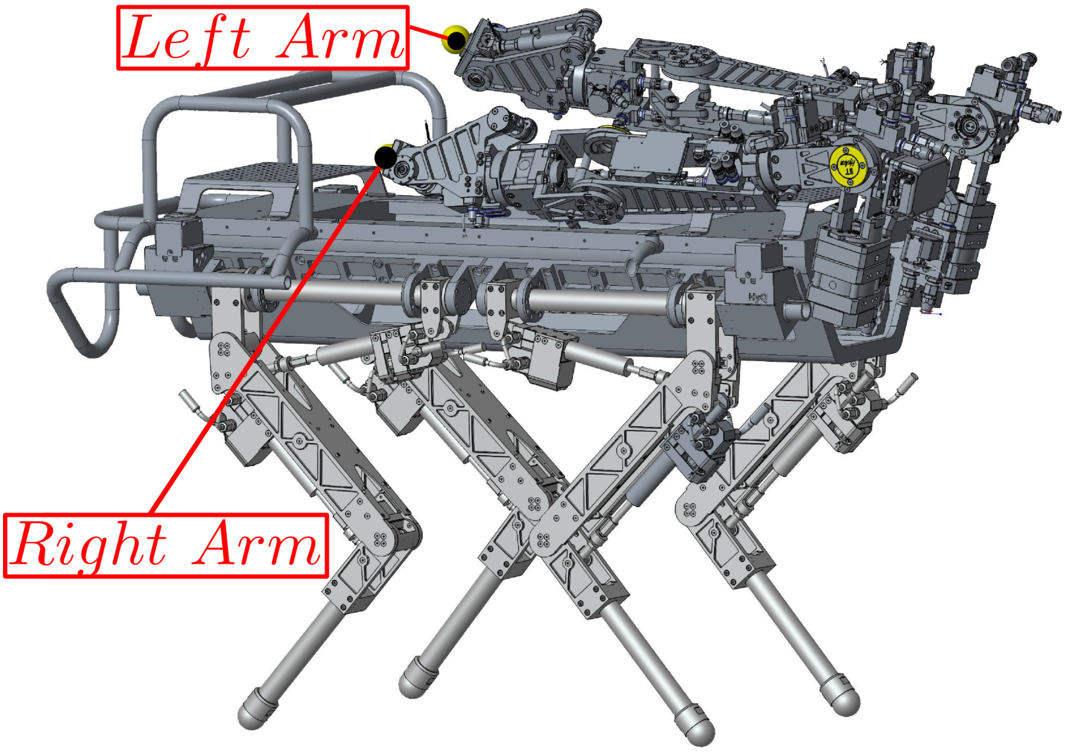
Left Arm
Right Arm

(b) The dual-arm system in stowed position

Figure 4.25: Centaur-like robot: The dual-arm system in (a) during operation and (b) stowed position

Chapter 5

Controllers of Robotic Arm and Mobile Platform

5.1 Hydraulic Model Based Low-level Torque Control of Robotic Arm

The target applications of mentioned in Chapter. 1 (see Section. 1.1), for a centaur-like robot required to interact with its surrounding environment or the target objects without causing excessive forces. Using pure position/velocity control for centaur-like robot limbs is not sufficient for such application(s). The interaction with the environment or target objects is better dealt with in the torque/force domain, rather than only in position [Craig, 1989, Spong et al., 2006, Siciliano and Khatib, 2008]. HyQ (mobile platform for centaur-like robot) is a fully torque controlled robot [Boaventura et al., 2012a]. The block diagram of HyQ low level torque control (inner loop) with an outer controller is shown in Fig. 5.1.

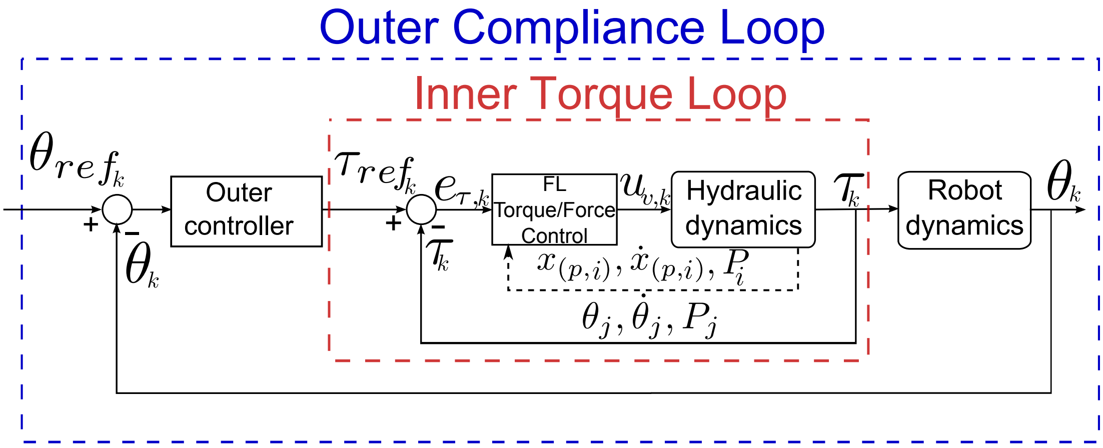
Outer Compliance Loop
Inner Torque Loop
θ_{ref_k}
+
−
θ_k
Outer controller
τ_{ref_k}
$e_{\tau,k}$
+
−
τ_k
FL Torque/Force Control
$u_{v,k}$
Hydraulic dynamics
$x_{(p,i)}, \dot{x}_{(p,i)}, P_i$
$\theta_j, \dot{\theta}_j, P_j$
τ_k
Robot dynamics
θ_k

Figure 5.1: Block diagram of HyQ control framework inner loop is a low level joint torque control with a outer controller [Boaventura et al., 2012a]

The outer loop creates the torque reference for inner torque loop controller, which calculate a input control signal $u_{v,k}$ for the hydraulic valve. Both the outer and inner controller use state feedback (τ_k,θ_k) from the hydraulic and robot dynamics. In the case of HyQ, the torque error $e_{\tau,k}$ is transformed into a force error using an effective lever arm of k^{th} joint actuated by the hydraulic cylinder. The effective lever arm varies according to the k^{th} leg joint position. Where $k = HAA, HFE, KFE$ are each leg joints in the series (see Section 3.2.1.1 for kinematic structure of HyQ).

The motivation to use the same control framework for HyArm comes from HyQ. As a matter of fact, based on this control framework HyQ has shown a wide range of abilities such as trotting [Barasuol et al., 2013], running [Semini et al., 2015], step reflex [Focchi et al., 2013a] and navigation over unstructured terrain [Winkler et al., 2014]; all these tasks involve direct contact with the ground. I will explains, how this control framework is used for hydraulically actuated robotic arm with $6DoF$ in series.

5.1.1 Hydraulic dynamics

The forward dynamics of the manipulator take torque as input to generate a desire joint motion. In order to achieve high performance accuracy for tracking desire joint's torque, we have to provide desired reference torque to the robot with the highest possible accuracy. In a simple mechanical case, the force is transmitted to a load through a compliant transmission element. Hence, the force dynamics depends on three elements: an actuator, a transmission source and load dynamics. An actuator provides an external force which accelerates a mass and it has an instantaneous velocity $\dot{x}_{vs}$. This velocity transmitted as an input to transmission spring (with a stiffness k_t) results in an output force f. The spring output force accelerates the load mass, generating instantaneous load velocity $\dot{x}_l$. In the case of hydraulics, pump and valve together are the velocity source. The hydraulic pump pressurises the fluid and the servo valve controls fluid flow inside the hydraulic actuator chambers. Therefore, the servo valve and flow dynamics determine the velocity source dynamics, and transmission stiffness depends on fluid compressibility and volume in each chamber. The a hydraulic actuator (cylinder and motor) model that describes the relation between control input to servo valve u_v, fluid flow dynamics and torque/force, is separately presented in the next section. Although it is coupled with the robotic arm's joint motion through θ and $\dot{\theta}$.

5.1.1.1 Model of the hydraulic rotary motor

The hydraulic motor schematics shown in Fig. 5.2 consists of a servo valve and a hydraulic motor. A control input u_v, chose the direction and magnitude of oil flow q_a and q_b in each chamber A and B, [Manring, 2005]:

$$q_{a,j} = \begin{cases} k_{v,1}\, u_{v,j}\sqrt{P_s - P_{a,j}} & if \quad u_{v,j} \geq 0 \\ k_{v,3}\, u_{v,j}\sqrt{P_{a,j} - P_t} & if \quad u_{v,j} < 0 \end{cases} \tag{5.1}$$

$$q_{b,j} = \begin{cases} -k_{v,2}\, u_{v,j}\sqrt{P_{b,j} - P_t} & if \quad u_{v,j} \geq 0 \\ -k_{v,4}\, u_{v,j}\sqrt{P_s - P_{b,j}} & if \quad u_{v,j} < 0 \end{cases} \tag{5.2}$$

where $j = \{1, 2, 3, 5\}$ corresponds to joint SAA, SFE, HR and WR, respectively. P_s and P_r are the supply and return pressures. The valve coefficients is denoted by $k_{v,w}$ (where $w = 1, 2, 3, 4$). This coefficients is related to the physical properties of the valve. While $P_{a,j}$ and $P_{b,j}$ represent pressure in chamber A and B. Neglecting external and internal leakage, the hydraulic pressures at each chamber are defined by the differential equations, [Manring, 2005]:

$$\dot{P}_{a,j} = \frac{\beta}{v_{a,j}}\left(q_{a,j} - D_{m,j}\dot{\theta}_j\right) \tag{5.3}$$

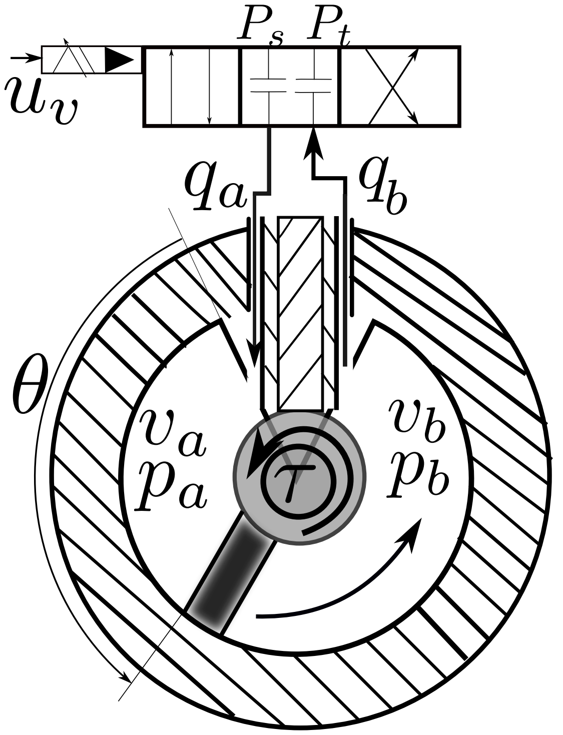

Figure 5.2: Cross section of a single-vane rotary hydraulic actuator illustrating the principle of operation and definition of variables: u_v is control signal, p_a and p_b are the chamber pressures, v_a and v_b are the chamber volumes, q_a and q_b are the fluid flow in and out from chamber A and B, P_s and P_t are the supply and the tank return pressures, θ is vane position, τ is the actuator torque.

$$\dot{P}_{b,j} = \frac{\beta}{v_{b,j}} \left(D_{m,j}\dot{\theta}_j + q_{b,j} \right) \tag{5.4}$$

where, $v_{a,j} = v_{au,j} + D_{m,j}\theta_j$ and $v_{b,j} = v_{bu,j} + v_{tot,j} - D_{m,j}\theta_j$ are chamber a and b volume respectively with $v_{au,j}$ and $v_{bu,j}$ being unused volumes of oil, when motor on either mechanical limits of their total rang-of-motion, The motor vane position and angular velocity is represented by θ_j and $\dot{\theta}_j$, respectively. The volumetric displacement of hydraulic motor presented by $D_{m,j}$. The torque τ produce by rotary motor can be calculated as:

$$\tau_j = D_{m,j}(P_{a,j} - P_{b,j}) \tag{5.5}$$

which time derivative is:

$$\dot{\tau}_j = D_{m,j}(\dot{P}_{a,j} - \dot{P}_{b,j}) \tag{5.6}$$

Substituting, (5.3)-(5.4) and (5.1)-(5.2) in (5.6) allows to define:

$$\dot{\tau}_j = f_{m,j}(\theta_j, \dot{\theta}_j) + g_{m,j}(P, \theta_j, u_{v,j}) \tag{5.7}$$

Where,

$$f_{m,j}(\theta_j, \dot{\theta}_j) = -\beta D_{m,j}^2 \left(\frac{1}{v_{a,j}(\theta_j)} + \frac{1}{v_{b,j}(\theta_j)} \right) \dot{\theta}_j \tag{5.8}$$

$$g_{m,j}(P, \theta_j, u_{v,j}) = g_{m,j}^{(+)}(P, \theta_j, u_{v,j}) \left(\frac{1 + sign(u_{v,i})}{2} \right) + g_{m,j}^{(-)}(P, \theta_j, u_{v,j}) \left(\frac{1 - sign(u_{v,i})}{2} \right), \tag{5.9}$$

and

$$g_{m,j}^{(+)}(P, \theta_j, u_{v,j}) = \beta D_{m,j} u_{v,j} \left(\frac{k_{v,1}\sqrt{P_s - P_{a,j}}}{v_{a,j}(\theta_j)} + \frac{k_{v,2}\sqrt{P_{b,j} - P_t}}{v_{b,j}(\theta_j)} \right) \quad for \quad u_{v,j} \geq 0 \tag{5.10}$$

$$g_{m,j}^{(-)}(P, \theta_j, u_{v,j}) = \beta D_{m,j} u_{v,j} \left(\frac{k_{v,3}\sqrt{P_{a,j} - P_t}}{v_{a,j}(\theta_j)} + \frac{k_{v,4}\sqrt{P_s - P_{b,j}}}{v_{b,j}(\theta_j)} \right) \quad for \quad u_{v,j} < 0 \tag{5.11}$$

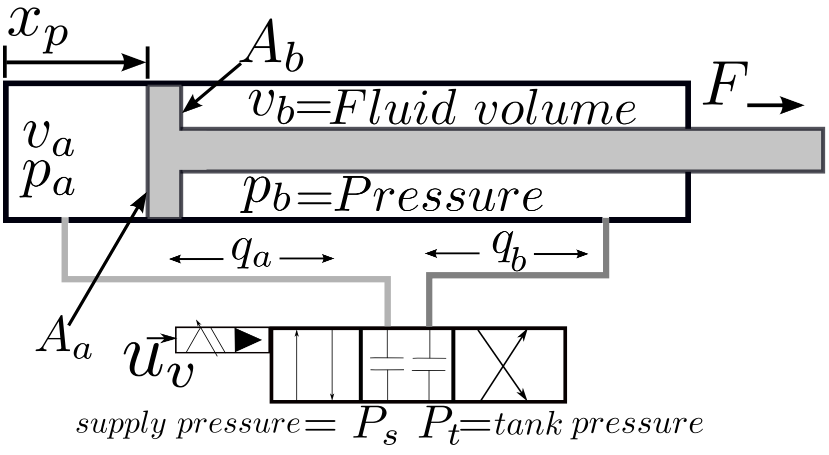

Figure 5.3: Cross section of asymmetric single rod cylinder hydraulic actuator illustrating the principle of operation and definition of variables: u_v is control signal, p_a and p_b are chamber pressures, v_a and v_b are chamber volumes A_a and A_b are piston and annulus areas, q_a and q_b are fluid flow in and out from chamber A and B, P_s and P_t are supply and tank return pressures, x_p piston position and F is actuator force.

5.1.1.2 Model of the Hydraulic Cylinder

The hydraulic schematic shown in Fig. 5.3, consist of a servo valve and asymmetric single rod cylinder used to produce forces. We used (5.1) and (5.2) to describes the relation between control input and oil flow for each chamber and replaced j with i, where $i = \{4, 6\}$ corresponds to either joint EFE and WFE, respectively. The P_s and P_r are the supply and return pressures. While $P_{a,i}$ and $P_{b,i}$ represent pressure in chamber A and B. Neglecting external and internal leakage, the hydraulic pressures at each chamber are defined by the differential equations, [Manring, 2005]:

$$\dot{P}_{a,i} = \frac{\beta}{v_{a,i}}(q_{a,i} - \dot{x}_{p,i}A_a) \tag{5.12}$$

$$\dot{P}_{b,i} = \frac{\beta}{v_{b,i}}(q_{b,i} + \dot{x}_{p,i}A_b) \tag{5.13}$$

where $v_{a,i} = (v_{pl} + A_a x_{p,i})$ and $v_{b,i} = (v_{pl} + A_b(s - x_{p,i}))$ are chamber a and b volume respectively with v_{pl} being the unused volumes of oil, when the cylinder is fully extended or retracted, β represents the fluid bulk modulus, s is maximum stroke length and $x_{p,i}$ the piston position defined as,

$$x_{p,i} = (x_{c,i}(\theta_i) - x_{m,i}), \tag{5.14}$$

where $x_{c,i}$ is the current length of the hydraulic cylinder, $x_{m,i}$ its minimum length. $\dot{x}_p$ in (5.12) (5.13) is the piston velocity,

$$\dot{x}_{p,i} = \frac{\partial x_{p,i}}{\partial \theta_i}\dot{\theta}_i \tag{5.15}$$

The force produced by the hydraulic actuator can be calculated as,

$$F = P_{a,i}A_a - P_{b,i}A_b, \tag{5.16}$$

which time derivative is:

$$\dot{F} = \dot{P}_{a,i}A_a - \dot{P}_{b,i}A_b. \tag{5.17}$$

Substituting (5.12)-(5.13) and (5.1)-(5.2) into (5.17) allows to define that:

$$\dot{F} = f_c(x_{p,i}, \dot{x}_{p,i}) + g_c(P, x_{p,i}, u_{v,i}) \tag{5.18}$$

where,

$$f_c(x_{p,i}, \dot{x}_{p,i}) = -\beta \dot{x}_p \left(\frac{A_a^2}{v_{a,i}(x_p)} + \frac{A_b^2}{v_{b,i}(x_p)} \right) \tag{5.19}$$

$$g_c(P, x_{p,i}, u_{v,i}) = g_c^{(+)}(P, x_{p,i}, u_{v,i}) \left(\frac{1 + sign(u_{v,i})}{2} \right) + g_c^{(-)}(P, x_{p,i}, u_{v,i}) \left(\frac{1 - sign(u_{v,i})}{2} \right), \tag{5.20}$$

and

$$g_c^{(+)}(P, x_{p,j}, u_{v,i}) = \beta\, u_{v,i} \left(\frac{A_a k_{v,1}\sqrt{P_s - P_{a,i}}}{v_{a,i}(x_p)} + \frac{A_b k_{v,2}\sqrt{P_{b,i} - P_t}}{v_{b,i}(x_p)} \right) \quad for \quad u_{v,i} \geq 0 \tag{5.21}$$

$$g_c^{(-)}(P, x_{p,j}, u_{v,i}) = \beta\, u_{v,i} \left(\frac{A_a k_{v,3}\sqrt{P_{a,i} - P_t}}{v_{a,i}(x_p)} + \frac{A_b k_{v,4}\sqrt{P_s - P_{b,i}}}{v_{b,i}(x_p)} \right) \quad for \quad u_{v,i} < 0 \tag{5.22}$$

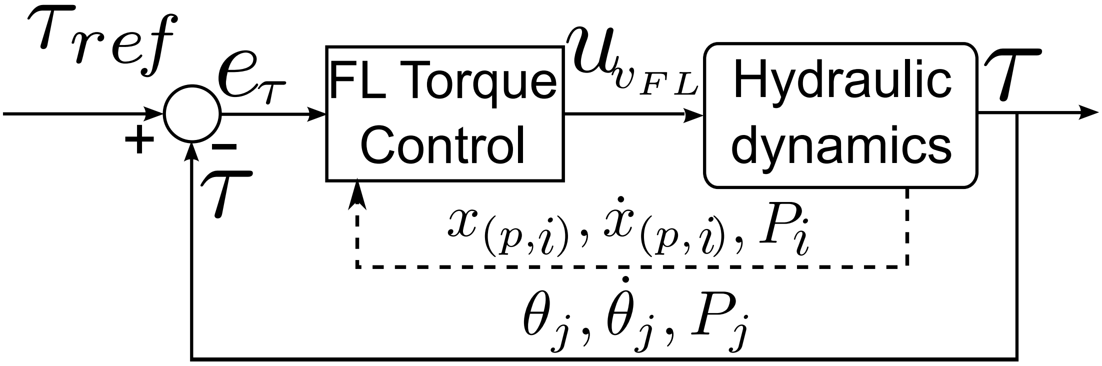

Figure 5.4: Block diagram of feedback linearisation torque control. The feedback linearisation is a model-based controller. In case of hydraulic cylinder it feedback piston position (x_p) and velocity $\dot{x}_p$, and in the case of hydraulic motor, vane position θ and velocity $\dot{\theta}$. It also compensate for load velocity influence and the pressure dynamics. Where $i = \{4, 6\}$ corresponds to either joint EFE and WFE and $j = \{1, 2, 3, 5\}$ corresponds to joint SAA, SFE, HR and WR actuated by hydraulic cylinder and motor, respectively.

5.1.2 Feedback Linearisation Torque Control

The relation between hydraulic flow in each actuator chamber $q_{a,*}, q_{b,*}$ and valve control input $u_{v,*}$ is a non-linear relation which results in a non-linear output torque/force, as represented by (5.1)-(5.2). A feedback linearisation technique is applied to improve force tracking by linearise the torque/force dynamics that compensates for flow and pressure non-linearities [Boaventura et al., 2012a]. By choosing valve control input $u_{v,*}$:

$$u_{v,*} = \frac{1}{g_*(\cdot)} (v_* - f_*(\cdot)) \tag{5.23}$$

where $*$ corresponds to robotic arm joints either actuated by hydraulic cylinder or motor, if $*^{th}$ joint is actuated by hydraulic cylinder $f_*(\cdot)$ and $g_*(\cdot)$ are given in (5.19) and (5.20), otherwise in (5.8) and (5.9), respectively. We have chosen v to be a PI controller with an additional feed forward term corresponding to the time derivative of the torque reference:

$$\dot{\tau} = v = \dot{\tau}_{ref} - k_p(\tau_{ref} - \tau) - ki_i \int (\tau_{ref} - \tau)dt \tag{5.24}$$

Then solving (5.24) equation of the linearised torque error dynamics:

$$\dot{e}_\tau - k_p e_\tau - k_i \int e_\tau dt = 0 \tag{5.25}$$

where, k_p and k_i are proportional and integral gains and e_τ is torque tracking error $e_\tau = (\tau_{ref} - \tau)$. Note that, in case of hydraulic cylinder torque tracking error e_τ is converted into force error. The real time implementation of the feedback linearisation torque control was not easy. Since, HyArm does not have pressure sensors for measuring pressures in each chamber pressure $p_{a,*}, p_{b,*}$ for each actuator. Based on load cell or torque measurement, we estimated the chamber pressures to calculate the function

$g(P,*)$. To handle modeling error and ensure stability, the gain $k_p c$ and $k_v c$ are included in the control law (as proposed by [Boaventura et al., 2012a]) in (5.23):

$$u_{v_{FL},*} = \frac{k_{pc}}{g_*(\cdot)}\left(v_* - k_v c f_*(\cdot)\right) \tag{5.26}$$

where, k_{pc} is pressure compensation gain and k_{vc} is velocity compensation gain. Finally, the block diagram of feedback linearisation torque control is shown in Fig. 5.4.

5.1.3 Outer Controller

A simple PD position control loop used as an outer controller cased with the feedback linearisation torque controller:

$$\tau_{ref_k} = k_{p_k}(\theta_{ref_k} - \theta_k) + k_{d_k}(\dot{\theta}_{ref_k} - \dot{\theta}_k) \tag{5.27}$$

where k_{p_k} denotes the values of proportional gains, can be interpreted as a spring stiffness and k_{d_k} the values of derivative gains which can interpreted as a damper. The τ_{ref_k} torque references to the inner torque controllers. The $\theta_{ref_k}, \dot{\theta}_{ref_k}$ and $\theta_k, \dot{\theta}_k$ are k^{th} joint reference trajectories and actual measurement.

5.2 High-level Controllers

The integration of robotic arm(s) with HyQ enables the HyQ to perform new tasks such as debris removal, balance assistance, door opening, and object manipulation. On the other hand, the integration of the arm, opens new challenges such as how to maintain the mobility and balance of the quadruped robot. When the integrated arm interacts with the environment or carries an unknown payload, a fundamental issue arises because the Center of Mass (CoM) of the whole robot can be dramatically shifted and the overall robot balance can be affected. In addition to this, for an object manipulation, it is important that the arm controller is robust against external/internal disturbances (payload variation and unknown dynamics such as friction and inertial forces coming from the mobile base). This requires a suitable control scheme which is robust to disturbances and uncertainties coming from the robot dynamics and environment.

To tackle with these challenges, we present a high level control framework that integrates the mobile platform controller with a robust arm controller. The arm controller is presented in Section 5.2.1, estimates and compensates external/internal disturbances while tracking desired joint trajectories. The mobile platform controller stabilizes the CoM position and the robot trunk orientation while optimizing for the Ground Reaction Forces (GRFs) as presented in Section 5.2.2.

5.2.1 The Arm Controller

As a first step in the development of the arm controller with a mobile platform, it is useful to evaluate the influence that the mobile platform has on the arm dynamics. Unlike Section 5.2.2, where we used a simplified model, here we will consider the full floating base model of the robot.

The dynamics of a floating-base articulated-body system can be expressed as two coupled dynamics equations: the one of the floating-base body (6 DoFs underactuated) and the one of the n rigid-bodies attached to it. In the case of our robot we have 5 kinematic branches: 4 legs and 1 arm, thus $n = n_{legs} + n_{arm}$. The equation of motions for the floating base robot (3.3) can be subdivided as follows [Featherstone, 2007]:

$$\left[\begin{array}{c|c} I_0^c & F \\ \hline F^T & M \end{array}\right] \begin{bmatrix} a_0 \\ \ddot{q} \end{bmatrix} + \begin{bmatrix} h_0^c \\ h \end{bmatrix} = \begin{bmatrix} 0 \\ \tau \end{bmatrix}, \tag{5.28}$$

where $I_0^c \in \mathbb{R}^{6\times 6}$ is the composite rigid body inertia of the robot, $F \in \mathbb{R}^{6\times n}$ is a matrix which contains the spatial forces required at the floating base to support each joint variable, h_0^c is the spatial bias force for the composite rigid body containing the whole floating-base system, $M \in \mathbb{R}^{n\times n}$ denotes active joints links (legs and arm) inertia matrix, $h \in \mathbb{R}^n$ denotes the correspondent vector of Coriolis, centrifugal and gravitational forces, $a_0 \in \mathbb{R}^6$ and $\ddot{q} \in \mathbb{R}^n$ denote floating-base and joint acceleration vectors, respectively, and $\tau \in \mathbb{R}^n$ denotes vector of joint torques and including the contribution of ground reaction forces. Starting with (5.28), we subtract $F^T(I_0^c)^{-1}$ times the first row from the second row. The resulting equation is

$$\left[\begin{array}{c|c} I_0^c & F \\ \hline 0 & M - F^T(I_0^c)^{-1}F \end{array}\right] \begin{bmatrix} a_0 \\ \ddot{q} \end{bmatrix} + \begin{bmatrix} h_0^c \\ h - F^T(I_0^c)^{-1}h_0^c \end{bmatrix} = \begin{bmatrix} 0 \\ \tau \end{bmatrix}. \tag{5.29}$$

The bottom row from (5.29), which can be decoupled as:

$$M^{fl}\ddot{q} + h^{fl} = \tau \tag{5.30}$$

where $M^{fl} = M - F^T(I_0^c)^{-1}F$ and $h^{fl} = h - F^T(I_0^c)^{-1}h_0^c$. This equation provides a direct relation between $\ddot{q}$ and τ incorporating the inertia of the base. M^{fl} and h^{fl} can be regarded as floating-base analogues to the coefficients of the standard fixed-base dynamic equation. Equation (5.30), can be further partitioned as follows:

$$\left[\begin{array}{c|c} M_{11}^{fl} & M_{12}^{fl} \\ \hline M_{21}^{fl} & M_{22}^{fl} \end{array}\right] \begin{bmatrix} \ddot{q}_{n_{legs}} \\ \ddot{q}_{n_{arm}} \end{bmatrix} + \begin{bmatrix} h_{n_{legs}}^{fl} \\ h_{n_{arm}}^{fl} \end{bmatrix} = \begin{bmatrix} \tau_{n_{legs}} \\ \tau_{n_{arm}} \end{bmatrix} \tag{5.31}$$

Extracting the bottom row from (5.31) we get:

$$M_{21}^{fl}\ddot{q}_{n_{legs}} + M_{22}^{fl}\ddot{q}_{n_{arm}} + h_{n_{arm}}^{fl} = \tau_{n_{arm}}. \tag{5.32}$$

Rearranging (5.32) and adding an external disturbance term τ_{ext},

$$\tau_{n_{arm}} = M_{22}^{fl}\ddot{q}_{n_{arm}} + M_{21}\ddot{q}_{n_{legs}} + h_{n_{arm}}^{fl} + \tau_{ext}, \tag{5.33}$$

presents a direct relation between $\ddot{q}_{n_{arm}}$, $\ddot{q}_{n_{legs}}$, external disturbance τ_{ext}, the influence of leg motion (internal disturbance), and $\tau_{n_{arm}}$. (5.33) can only be used to develop model-based control schemes which require a perfect knowledge of robot dynamics and disturbances. The robot dynamics non-linear terms are tightly coupled, and small model discrepancies can lead to instabilities. To avoid model estimation we choose a model-free control scheme based on time-delay estimation (TDE).

Time Delay Estimation

The target of the arm controller is to compensate all external and internal disturbances such that the arm joints positions $q_{n_{arm}}$ can track a desired trajectory $q_{n_{arm}}^d$ in a robust way. To achieve this we adopt a time-delay estimation (TDE) scheme [Youcef-Toumi and Ito, 1988], [Hsia et al., 1991] which provides a model-free control law to compensate for the non-linearities terms of robot dynamics and to enforce the desired dynamics for the tracking error. Following a procedure similar to [Lee et al., 2013], we rearrange (5.33) and introduce a constant diagonal matrix $\overline{M}$, which may assume the nominal values of M_{22}^{fl}:

$$\tau_{arm} = (\overline{M} + M_{22}^{fl} - \overline{M})\ddot{q}_{n_{arm}} + M_{21}^{fl}\ddot{q}_{n_{legs}} + h_{n_{arm}}^{fl} + \tau_{ext} \tag{5.34}$$

now we work-out the linear (decoupled) part and group all the non-linearities and couplings of the robot dynamics, internal and external disturbances into a vector H:

$$\tau_{n_{arm}} = \overline{M}\ddot{q}_{n_{arm}} + \underbrace{(M_{22}^{fl} - \overline{M})\ddot{q}_{n_{arm}} + M_{21}^{fl}\ddot{q}_{n_{legs}} + h_{n_{arm}}^{fl} + \tau_{ext}}_{H} \tag{5.35}$$

$$\tau_{n_{arm}} = \overline{M}\ddot{q}_{n_{arm}} + H \tag{5.36}$$

A model-free time delay controller designed for tracking joint position has the following structure:

$$\tau_{n_{arm}}^{d} = \overline{M}\upsilon + \hat{H} \tag{5.37}$$

where υ represents the control input to the linear system ($\bar{M}$ is constant diagonal) and is defined as follows:

$$\upsilon = \ddot{q}_{n_{arm}}^{d} + K_{d_{n_{arm}}}\dot{e}_{n_{arm}} + K_{p_{n_{arm}}}e_{n_{arm}} \tag{5.38}$$

where $e_{n_{arm}}$ is the tracking error between the actual $q_{n_{arm}}$ and the desired $q_{n_{arm}}^{d}$ arm joint position, $\hat{H}$ is an estimate of H and $K_{p_{n_{arm}}}$ and $K_{d_{n_{arm}}}$ are the proportional and derivative gains respectively. Next, we substitute (5.38) as the control input to (5.37). If $\hat{H}$ is a good estimate of H the tracking error converges to zero with a desired second-order dynamics set by $K_{d_{n_{arm}}} = 2\omega_n\varsigma I_n$ and $K_{p_{n_{arm}}} = \omega_n^2 I_n$, where ω_n and ς are desired natural frequency and damping ratio, respectively.

From (5.36), it can be noted that $H = \tau_{arm} - \overline{M}\ddot{q}_{arm}$. Due to a violation of causality we cannot use measurement data of τ and $\ddot{q}_{arm}$ at time t to compute H. In this respect the main idea of TDE is to use 1-sample delayed measurements for the estimation:

$$\hat{H} \approx \tau_{arm}(t - T_s) - \overline{M}\ddot{q}_{arm}(t - T_s) \tag{5.39}$$

where T_s is the sampling interval, for example, $T_s = 1ms$ is used in this case study. Finally, we use (5.39) into (5.37) to obtain the torque command $\tau_{n_{arm}}^{d}$ that will compensate for external and internal disturbances and track the desired arm position trajectory. The stability condition of the time-delay controller is well-established by Youcef-Toumi [Youcef-Toumi and Wu, 1992] and Hsia [Hsia and Gao, 1990], independently, represented as $||I - M_{22}^{fl-1}\bar{M}|| < 1$.

5.2.2 Mobile platform controller

In this section, we present the algorithm used for controlling the CoM position and robot trunk orientation while optimizing for the ground reaction forces (GRFs). The mobile platform controller is proposed and implemented by [Focchi et al., 2015]. The arm placement shifts the CoM significantly, requiring an algorithm which redistributes the load of the stance feet to maintain the balance. For control purposes we applied a linear mapping between GRFs and robot body accelerations using a lower dimensional model of the robot (massless legs) which takes into account only the centroidal dynamics.

Centroidal robot dynamics

We assume the GRFs are the only external forces acting on the system. Therefore, we can express the linear acceleration of the CoM $\ddot{x}_{com} \in \mathbb{R}^3$ and the angular acceleration of the base $\dot{\omega}_b$ as functions of the GRFs (i.e. $f_1, \ldots, f_c \in \mathbb{R}^3$, where c is the index of stance feet):

$$m(\ddot{x}_{com} + g) = \sum_{i=1}^{c} f_i \tag{5.40}$$

$$I_G \dot{\omega}_b \simeq \sum_{i=1}^{c} (p_{com,i} \times f_i), \tag{5.41}$$

where $m \in \mathbb{R}$ is the total robot's mass, $g \in \mathbb{R}^3$ is the gravity acceleration vector, $I_G \in \mathbb{R}^{3\times3}$ is the centroidal rotational inertia [Orin et al., 2013], $p_{com,i} \in \mathbb{R}^3$ is a vector going from the CoM to the position of the i^{th} foot defined in an inertial world frame $\mathcal{W}$ (see Fig. 5.5). Since our platform has nearly point-like feet, we assume that it cannot generate moments at the contacts, thus f_c are pure linear forces. As a final remark the term $\dot{I}_G \omega_G$ in the Euler equation (5.41) was neglected. Indeed, even though the presence of the moving masses of the arm links can potentially create changes on I_G, we will only consider experiments which involves small ω_G, making the term $\dot{I}_G \omega_G$ very small. Where (5.40) and (5.41) describe how the GRFs affect the CoM acceleration and the angular acceleration of the robot's base.

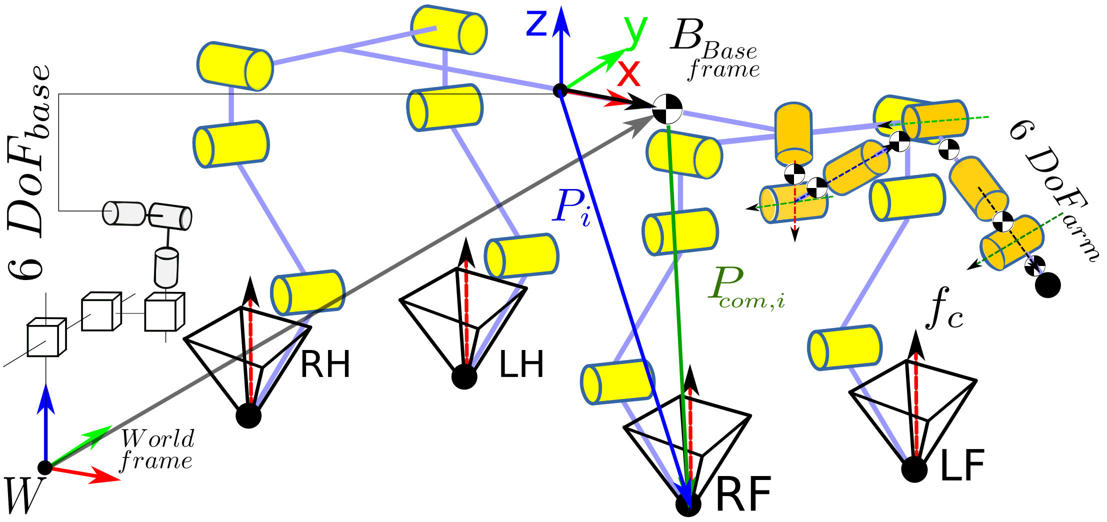

Figure 5.5: Summary of the nomenclature used for mobile platform controller. Leg labels: left front (LF), right front (RF), left hind (LH) and right hind (RH). The world frame W, the base frame B (attached to the geometric center of the robot body). Left subscripts indicate the reference frame, for instance $B^{x_{com}}$ is the location of the CoM w.r.t. the base frame. In case of no left subscript, quantities are expressed w.r.t. W. The C_i is i^{th} contact point between ground and i^{th} limb. The f_c is the ground reaction force (GRFs), where c is the number of stance feet.

Control of CoM and base orientation

A *trajectory generation* module (see. Fig. 5.6) computes desired trajectories for the CoM, the base orientation the swing foot (e.g. to achieve a static walking pattern [Focchi et al., 2015]). We compute the desired acceleration of the CoM $\ddot{x}^d_{com} \in \mathbb{R}^3$ and the desired angular acceleration of the robot's base $\dot{\omega}^d_b \in \mathbb{R}^3$ using a PD control law:

$$\ddot{x}^d_{com} = K_{pcom}(x^d_{com} - x_{com}) + K_{dcom}(\dot{x}^d_{com} - \dot{x}_{com}) \tag{5.42}$$

$$\dot{\omega}^d_b = K_{pbase}e(R^d_b R^\top_b) + K_{dbase}(\omega^d_b - \omega_b) \tag{5.43}$$

where $x^d_{com} \in \mathbb{R}^3$ is the desired position of the CoM, and $R^\top_b \in \mathbb{R}^{3\times3}$ and $R^d_b \in \mathbb{R}^{3\times3}$ are coordinate rotation matrices representing the actual and desired orientation of the base w.r.t. the world reference frame, respectively, $e(\cdot) : \mathbb{R}^{3\times3} \rightarrow \mathbb{R}^3$ is a mapping from a rotation matrix to the associated rotation vector, $\omega_b \in \mathbb{R}^3$ is the angular velocity of the base.

Computation of desired GRFs

Given a desired value of the linear acceleration of the CoM and the angular acceleration of the robot's base it is possible to rewrite (5.40) and (5.41) in matrix form:

$$\underbrace{\begin{bmatrix} I & \dots & I \\ [p_{com,1}\times] & \dots & [p_{com,c}\times] \end{bmatrix}}_{A} \underbrace{\begin{bmatrix} f_1 \\ \cdot \\ \cdot \\ \cdot \\ f_c \end{bmatrix}}_{f} = \underbrace{\begin{bmatrix} m(\ddot{x}^d_{com} + g) \\ I_g \dot{\omega}^d_b \end{bmatrix}}_{b}, \tag{5.44}$$

The desired GRFs are computed every control loop by solving the following optimization problem as a quadratic program [Focchi et al., 2015]:

$$\begin{aligned} f^d = & \underset{f \in \mathbb{R}^k}{\operatorname{argmin}} (Af - b)^\top S(Af - b) + \alpha f^\top W f \\ & \text{s.t.} \quad \underline{d} < Cf < \bar{d}, \end{aligned} \tag{5.45}$$

where $S \in \mathbb{R}^{6\times6}$ and $W \in \mathbb{R}^{k\times k}$ are positive-definite weight matrices, $\alpha \in \mathbb{R}$ weighs the secondary objective (e.g. regularization to keep the solution bounded), $C \in \mathbb{R}^{p\times k}$ is the inequality constraint matrix, $\underline{d}, \bar{d} \in \mathbb{R}^p$ the lower/upper bound respectively, with p being the number of inequality constraints. These ensure that a) the GRFs lie inside the friction cones and b) the normal components of the GRFs stay within some user-defined values. We exploit the redundancy of the solution to ensure the respect of these inequality constraints, and approximate friction cones with a square pyramid model to express them as linear constraints. The desired joint torques $\tau^d_{legs} \in \mathbb{R}^{n_{legs}}$ (where n_{legs} is the number of leg actuated joints) computed by superimposing two control actions. First, the mobile platform control block maps the desired GRFs f^d into joint space, outputting the feedforward torques τ_{ff}:

$$\tau_{ff} = -S_{legs} J^\top_c f^d, \tag{5.46}$$

where $J_c \in \mathbb{R}^{k\times n+6}$ is the stacked Jacobian of the contact points and S_{legs} is a selection matrix that selects the legs DoF. The same mapping was used by Ott et al.

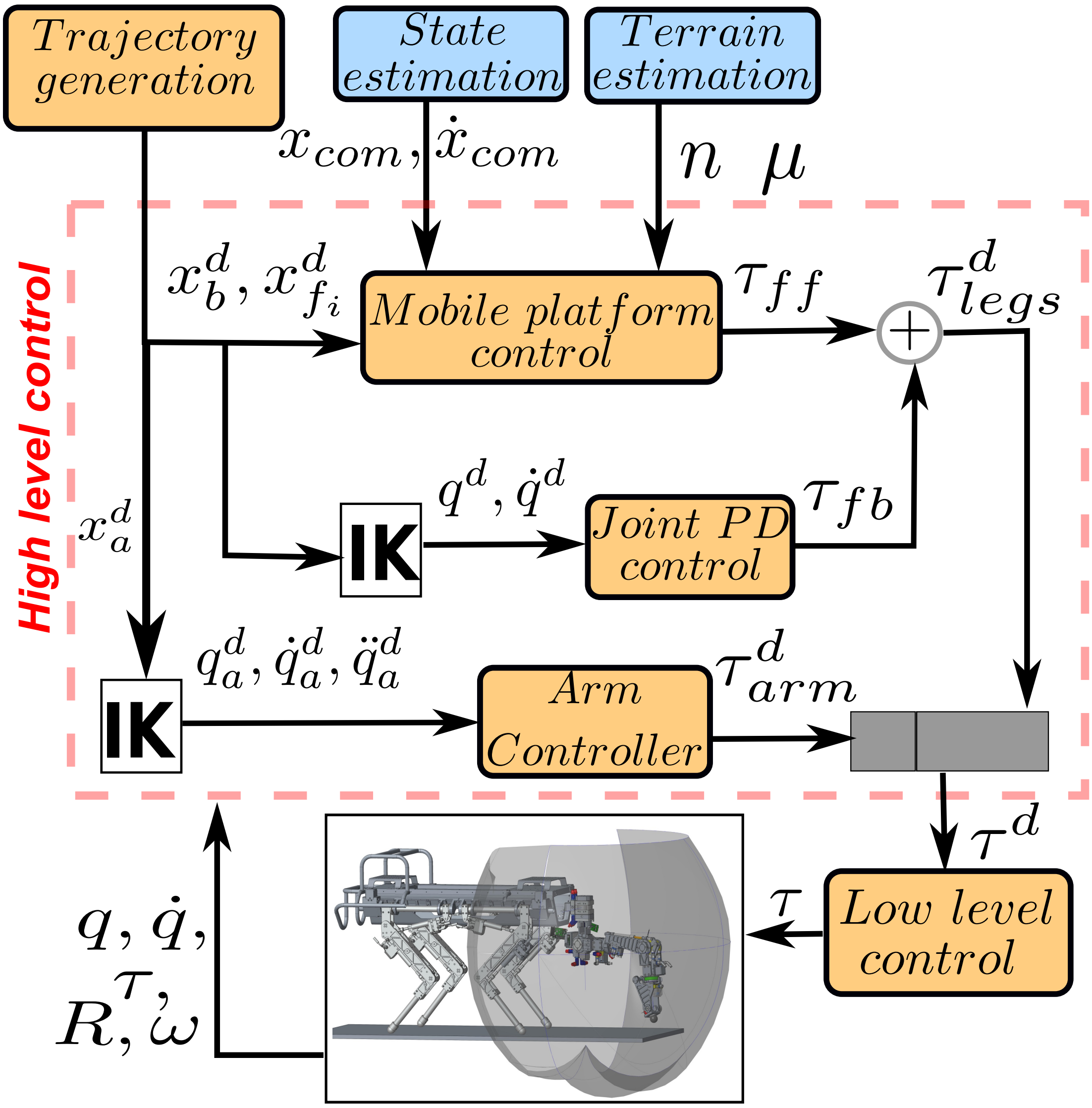
Trajectory generation
State estimation
Terrain estimation
$x_{com}, \dot{x}_{com}$
$n \quad \mu$
High level control
$x_b^d, x_{f_i}^d$
Mobile platform control
τ_{ff}
τ_{legs}^d
x_a^d
IK
$q^d, \dot{q}^d$
Joint PD control
τ_{fb}
IK
$q_a^d, \dot{q}_a^d, \ddot{q}_a^d$
Arm Controller
τ_{arm}^d
τ^d
Low level control
τ
$q, \dot{q}, \tau, R, \omega$

Figure 5.6: Block diagram of the control framework. The trajectory generation block compute desired trajectories for robot CoM, the base orientation and joints, high level control computes the reference torques for the low-level controller. For further detail see Section 5.2.1 and 5.2.2.

[Ott et al., 2011] and it is valid only for quasi-static motion. Second, the joint PD control block consists of a proportional-derivative (PD) joint-position controller with low gains motivated by safety reasons that hydraulic actuators can generate fast and powerful movements, and it is also used to move the swing leg. During the swing motion we increase the PD gains of the swing leg joints to improve tracking capabilities. The desired arm torques τ^d_{arm} are computed as described in Section 5.2.1. The whole vector of desired torque $\tau^d = \begin{bmatrix} {\tau^d_{legs}}^T & {\tau^d_{arm}}^T \end{bmatrix}^T$ is then sent to the underlying joint-torque controllers (see Fig 5.6) [Boaventura et al., 2012a]. In Chapter 6, we will present the experimental to evaluate the performance of integrated control framework.

5.3 Payload estimation

Payload estimation is an essential feature for our platform because the weight added by an object at the end of the arm can cause loss of stability if not properly accounted for. In this section, we will present how we implemented this feature in our framework. We assume there are not relevant disturbance forces coming from the quadruped platform. In this respect, we treat the arm as mounted onto a fixed base. Moreover we focus on the case of a point mass object rigidly attached to the arm tip (hand) leaving the generalization to the case of a rigid-body moving object to future works. The time delay controller will compensate for the joint position tracking error generated by the added payload. The basic idea is to compare the arm torques predicted by the model with the real ones. Subsequently, mapping the resulting torque error vector to the force at the end effector through kinematics. And finally projecting the resulting wrench (6 Dofs) in the direction of gravity to identify the gravity (linear) force of the added mass.

$$\begin{aligned} {}_wF_m &= {}_wX_b^* J^{-T}(\tau_{ID} - \tau_{arm}) \\ m_p &= {}_wF_{m_z}/g \end{aligned} \tag{5.47}$$

where ${}_wF_m$ is the wrench at the end effector defined in the world frame, ${}_wX_b^*$ is a pure rotation spatial transform which maps the wrench from the base to the world frame. $J \in \mathbb{R}^{6\times 6}$ is the Jacobian of the end-effector from the arm attachment to the end-effector (note that we use a standard inversion because Jacobian is a square matrix). τ_{ID} are the torques predicted by the model of the arm to stay in the actual configuration, τ_{arm} the measured torques. We used estimated payload m_p to update the CoM location to ensure the stability of the robot. In next chapter (see Section 6.2.3), we will presents the experimental result of payload estimation scheme.

Chapter 6

Experimental Results and Discussion

6.1 Fixed Based Manipulator Experimental Results and Discussion

We performed various experiments to evaluate the performance of the low level torque control framework presented in Section 5.1. I performed a gradual assessment of the full system by dividing it into two different groups: (a) sine tasks for fixed base robotic arm under torque control with and without payload to assess desired torque tracking; and (b) static tasks to assess the desired torque tracking without outer controller influence.

6.1.1 Sine Task for Fixed Base Robotic Arm Under Torque Control with and without Payload

We set a sinusoidal signal as a desired position reference for all the joints to the outer controller with various frequencies $0.5Hz$ and $1Hz$), as shown in Fig 6.1 and 6.2, respectively. The black (dash line) represents the desired position (first column) and torque (second column) as a reference for each joint and red (sold line) is the actual measurement starting from base joint SAA to WFE (last joint). The distal joint links have smaller inertia compared, to joints closer to the robotic arm base. Therefore, their position tracking performance is better then torque tracking and is otherwise true for joints closer to base joint, especially comparing first (SAA) and last (WFE) joints. The SAA torque tracking performance in both experiential results with 0.5Hz and 1Hz is better then its positing tracking. Because the first joint needs to accelerate, a bigger inertia result means better torque tracking. On the other hand, WFE joint have better position tracking then torque due to small inertia of the last link.

To further test the performance of inner torque loop, we performed another experiment, where we rigidly attached a $5kg$ payload to the end-effector of $HyArm$. I set sinusoidal signals with $0.5Hz$ frequency as position reference to the outer controller; results are summarized in Fig 6.3. It is clear that, torque tracking for the last joint improved compared to previous experimental results at the cost of reduced position tracking. It is worth mentioning that each joint's position tracking has a dead-zone which can be improved by adding feed-forward terms to overcome actuator internal friction.

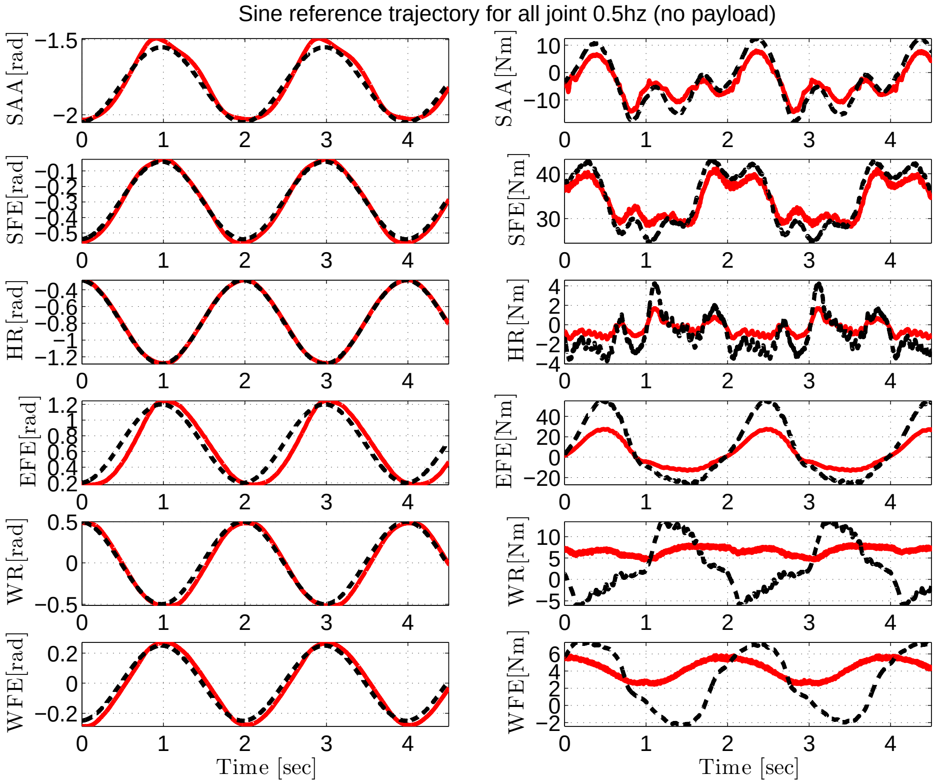

Figure 6.1: Experiment 1: sinusoidal reference trajectory for all joints at 0.5Hz without payload. Where, black (dash line) represents desired position (first column) and torque (second column) as a reference for each joint and red (sold line) is actual measurement starting from base joint SAA to WFE (last joint).

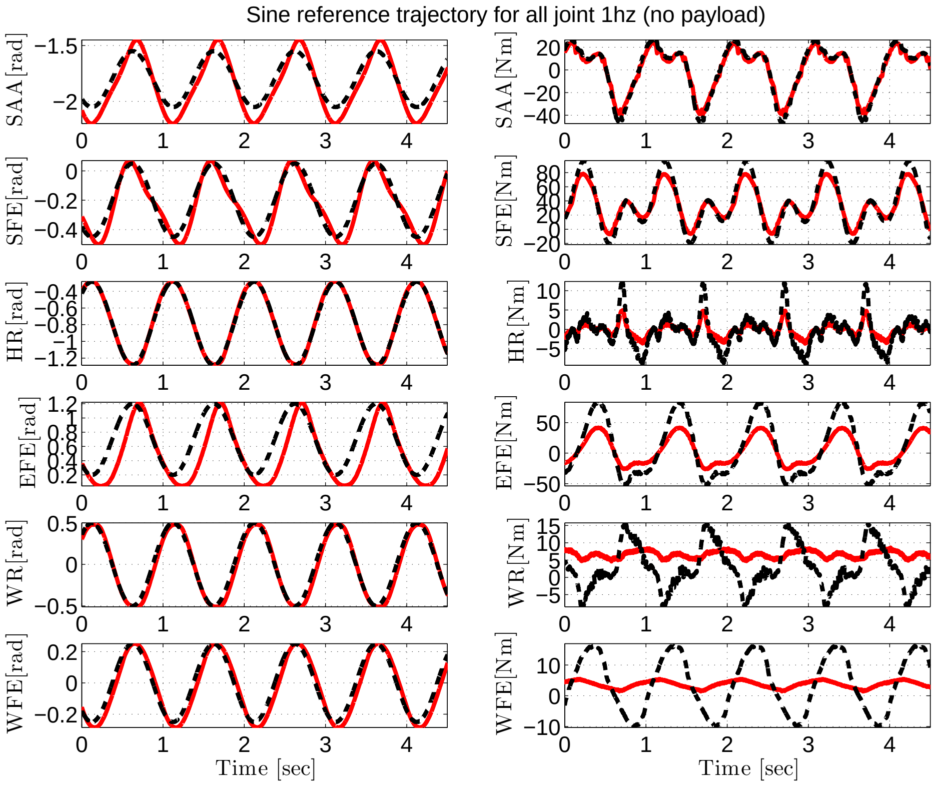

Figure 6.2: Experiment 2: sinusoidal reference trajectory for all joints at 1Hz without payload. Where, black (dash line) represents desired position (first column) and torque (second column) as a reference for each joint and red (sold line) is actual measurement starting from base joint SAA to WFE (last joint).

6.1.2 Static Task Under Torque Control for Fixed Base Robotic Arm

The inner torque loop performance can also be affected by outer controller performance. To this end, we performed static tests. In this experiment, the K_p gain for each joint was set to 150 then reduced to 75 and 25, which represent the joint's stiffness Nm/rad. I set a default joint position as a reference to the outer controller and only fed in current joint position and external forces which were applied by a user at the end-effector of the HyArm. The static tests result with joint's stiffness set 150$[Nm/rad]$ are presented in Fig. 6.5, which showed that the torque controller performed as excepted (better torque tracking). A youtube video link is given in Chapter C in which HyArm is demonstrating torque controlled capability for both sine and static tasks.

6.2 High-level Controllers Experimental Results and Discussion

We carried out a set of experiments on the multi-legged mobile manipulator to test the integrated control framework presented in Section 5.2. We performed a gradual assessment of the full system by dividing it into four different groups: (A) A static test with a moving arm, to assess the capability of the mobile platform controller to regulate the CoM motion. Indeed the CoM moves due to the motion of the arm

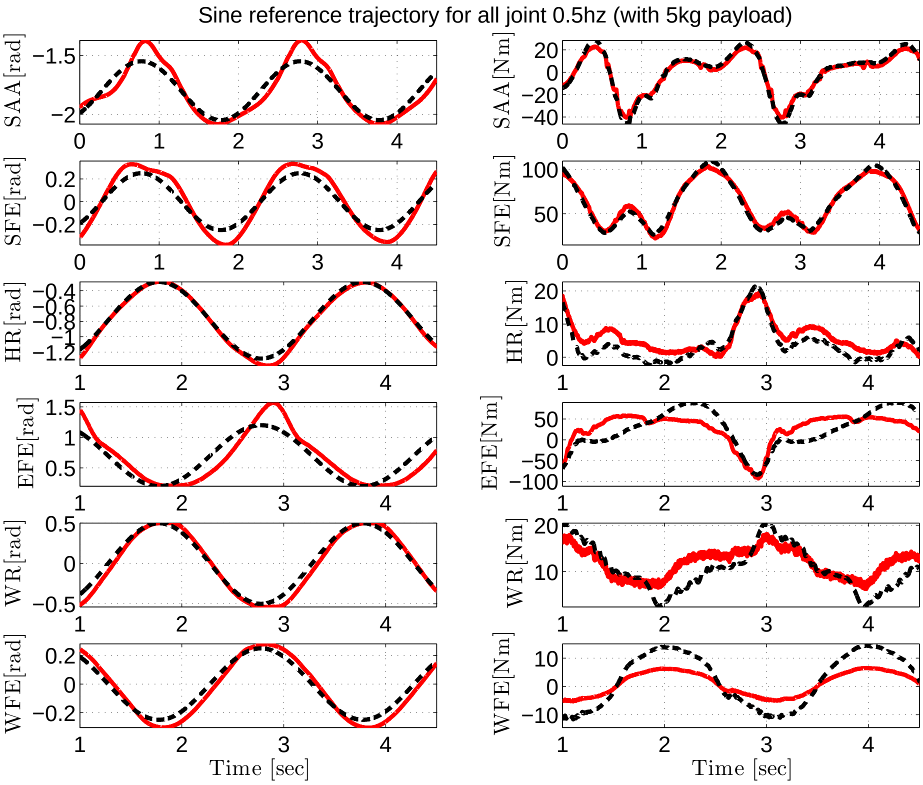

Figure 6.3: Experiment 3: sinusoidal reference trajectory for all joints at 0.5Hz with 5kg payload. Where, black (dash line) represents desired position (first column) and torque (second column) as a reference for each joint and red (sold line) is actual measurement starting from base joint SAA to WFE (last joint).

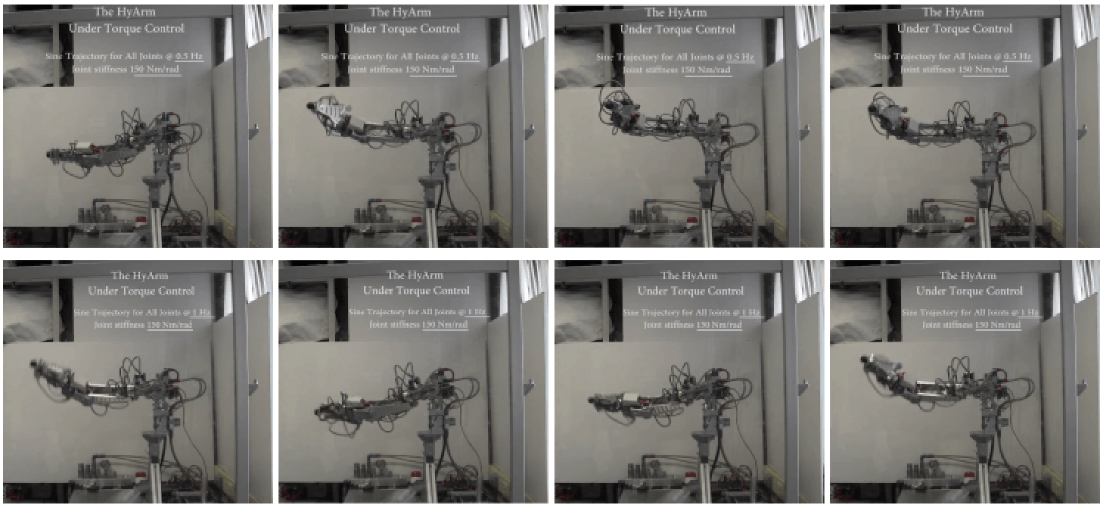
The HyArm
Under Torque Control
Sine Trajectory for All Joints @ 0.5 Hz
Joint stiffness 150 Nm/rad
The HyArm
Under Torque Control
Sine Trajectory for All Joints @ 1 Hz
Joint stiffness 150 Nm/rad

Figure 6.4: Snapshots of the two experimental trials used to evaluate the performance of our low level control framework. From top to bottom: sinusoidal reference trajectory for all joints at 0.5Hz (first row) and with (second row) sinusoidal reference trajectory for all joints at 1Hz. A youtube video link is given in Chapter C in which HyArm is demonstrating torque controlled capability for both sine and static tasks.

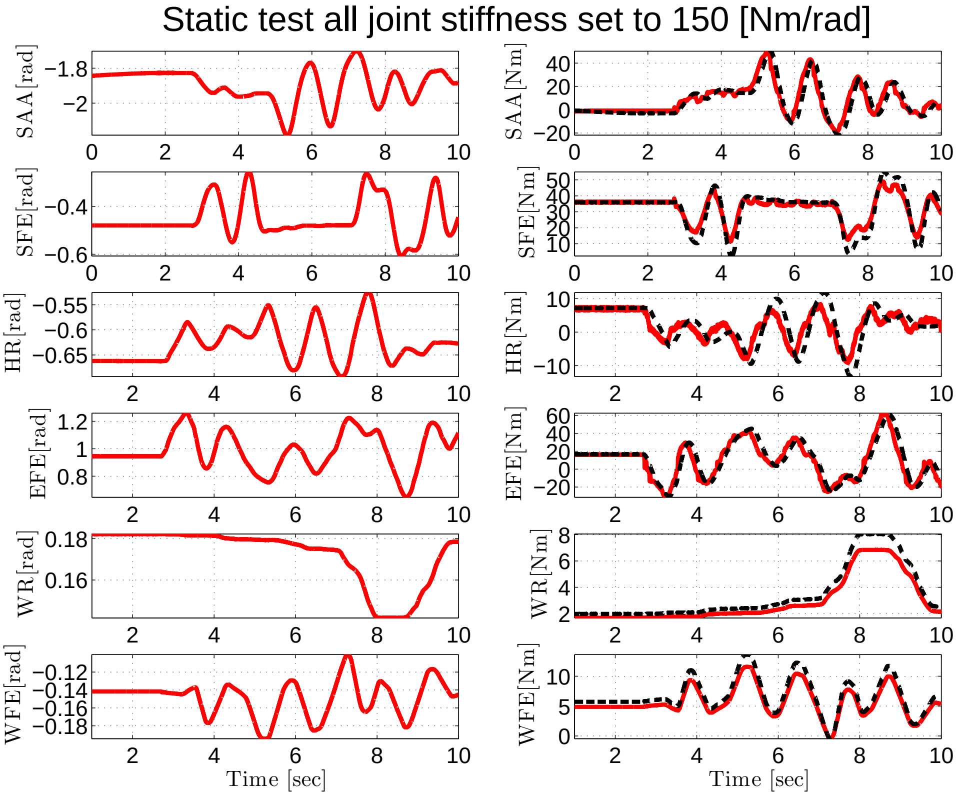

Figure 6.5: Experiment 4: Static test for HyArm attached a fixed base. The external forces are applied by a user at the end-effector of HyArm to assess inner loop torque controller joint torque tracking performance.

and to compensate for the unbalanced load caused by the weight of the arm. (B) Arm controller tracking, to assess the desired joint position tracking capabilities of the arm controller while compensating for gravity, friction and other disturbances. (C) Payload estimation while the mobile platform is standing still and the arm is carrying an unknown payload. (D) Walking tests with the arm moving, to verify the capability of both the arm and mobile controllers.

6.2.1 Static base with moving arm

Although the mobile platform controller for legs is decoupled from the arm, there is a significant influence from the arm motion. This can be dealt (damped) with the mobile platform controller, because we consider the contribution of the arm joints in the whole robot CoM computation and this is actively controlled in our framework.

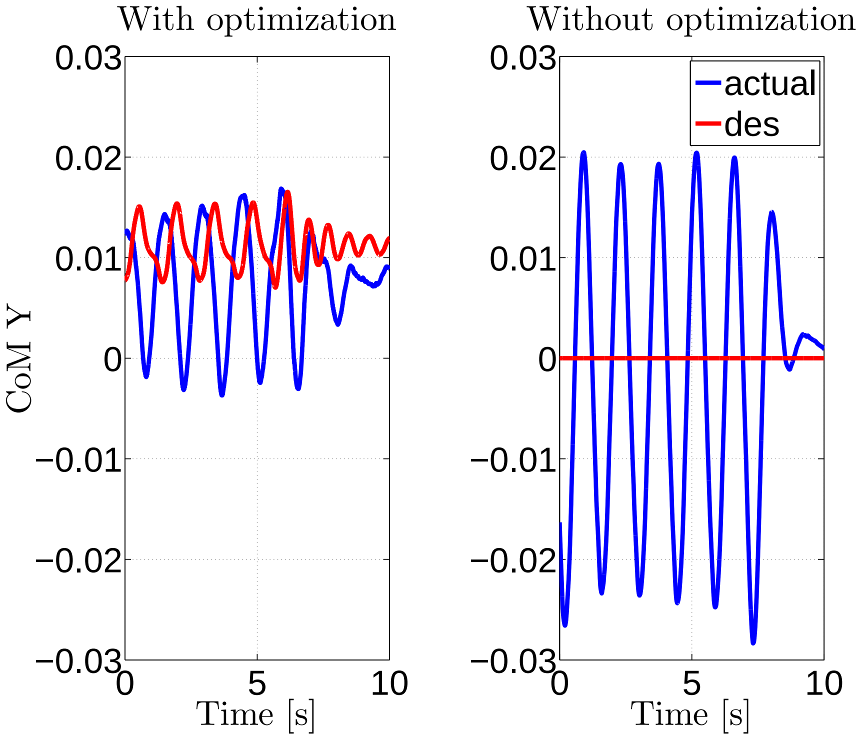

Figure 6.6: Rejection of arm motion disturbances at $0.7Hz$, on the robot CoM with and without the mobile platform controller. Blue line represent the actual COM $Y[m]$ position. Whereas, the red line represent desired COM $Y[m]$ position.

Frequencies	With optimization	Without optimization
0.5Hz	0.0058	0.0141
0.6Hz	0.0060	0.0142
0.7Hz	0.0070	0.0144

Table 6.1: root-mean-square (RMS) value of peak to peak oscillation on CoM Y $[m]$ due to arm motion at different frequencies

Fig. 6.6 shows the effectiveness of the mobile platform controller by comparing two scenarios, (a) when the mobile controller is actively damping disturbances coming from the arm motion by optimizing the GRF and (b) without optimization. We gave a sinusoidal trajectory as a reference to the arm SAA joint with an amplitude of $0.5rad$ and frequency at $0.7Hz$ as a disturbance source for the mobile platform. In Fig. 6.7 the first column shows effects of the arm motion the base robot torso is pitched forward and creating a big yaw motion compared to the second column with GRF optimization robot torso is stable and horizontal. We performed the various experiments with different frequencies, root-mean-square (RMS) value peak to peak oscillation on CoM Y are summarized in Table 6.1. A youtube video link is given in Chapter C that shows the experimental results with static base and moving arm.

6.2.2 Arm controller tracking

In this section, we show experimental results that demonstrate the ability of the TDE controller o reject gravity disturbances (for further details see Section 5.2.1). For the sake of brevity, we will only report the tracking of the three shoulder joints which are mostly affected by gravity and large inertia. As shown in Fig. 6.8, the desired trajectories are defined by a sinusoidal function with different frequencies for each shoulder joint. Despite the absence of any kind of gravity compensation, the torque disturbance coming from gravity is appropriately rejected during the arm motion and the tracking accuracy is not disturbed.

6.2.3 Payload estimation

To show the payload estimation capability of the approach illustrated in Section 5.3, we attached a $5kg$ mass to the arm tip. To discard high frequency disturbances from the estimation the output m_p of the estimator, which is recomputed at each control loop a 1st order butterworth filter with 1 Hz cut-off frequency. In Fig. 6.9 we show the estimation for the mass added at time $3.75s$. The estimation error is around $0.5kg$. A limitation of this approach is that the quality of the estimation is limited by modeling errors. Thus model identification should be carried out to improve the model until the desired accuracy in the payload estimation is achieved.

6.2.4 Walking tests with arm

We performed walking tests with the arm moving to verify both the mobile platform and arm controller capability. In Fig. 6.10 and a youtube video link given in Chapter C shows the experimental results of walking tests with static and moving arm.

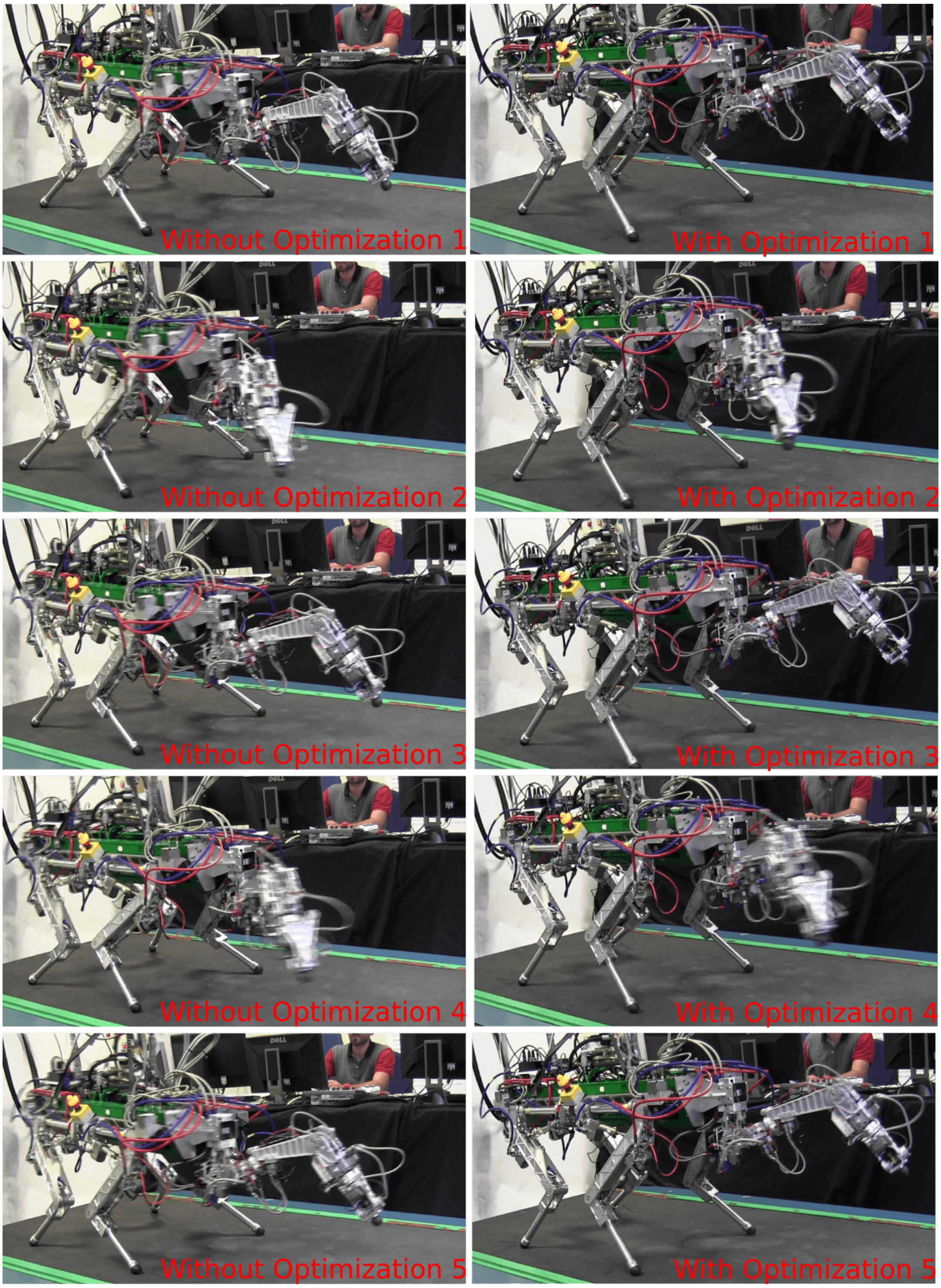
Without Optimization 1
With Optimization 1
Without Optimization 2
With Optimization 2
Without Optimization 3
With Optimization 3
Without Optimization 4
With Optimization 4
Without Optimization 5
With Optimization 5

Figure 6.7: Snapshots of the two experimental trials used to evaluate the performance of control framework. The robotic arm is mounted in front of HyQ. From left to right: Static tests with moving arm without (first column) and with (second column) mobile platform controller, respectively.

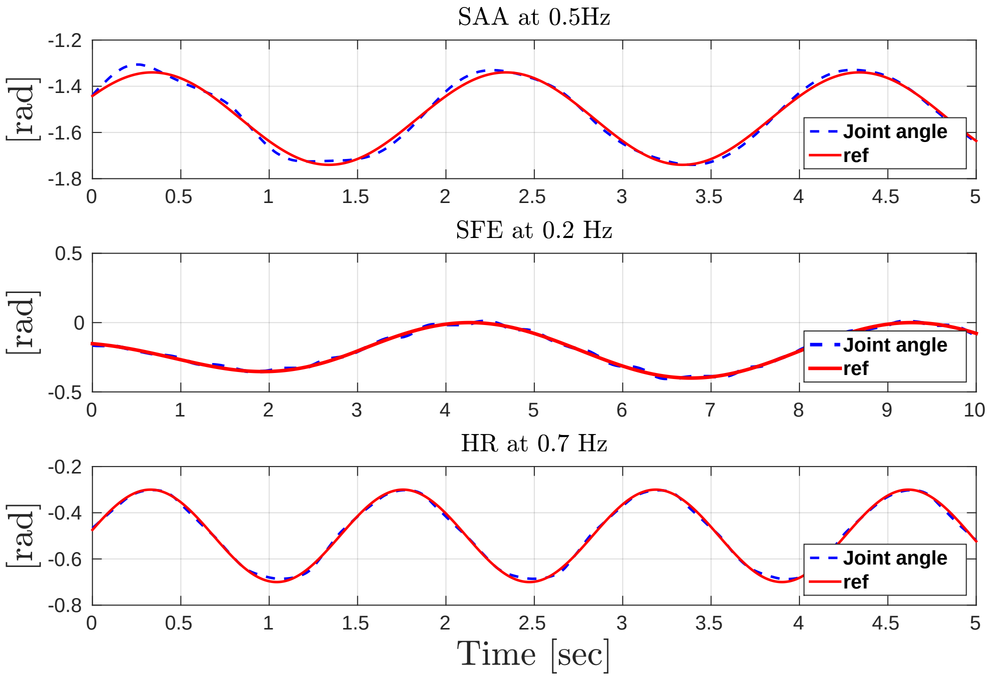

Figure 6.8: The first three shoulder joints position tracking: the blue dotted line represent the result of time delay controller and the red solid line represent the desired trajectory.

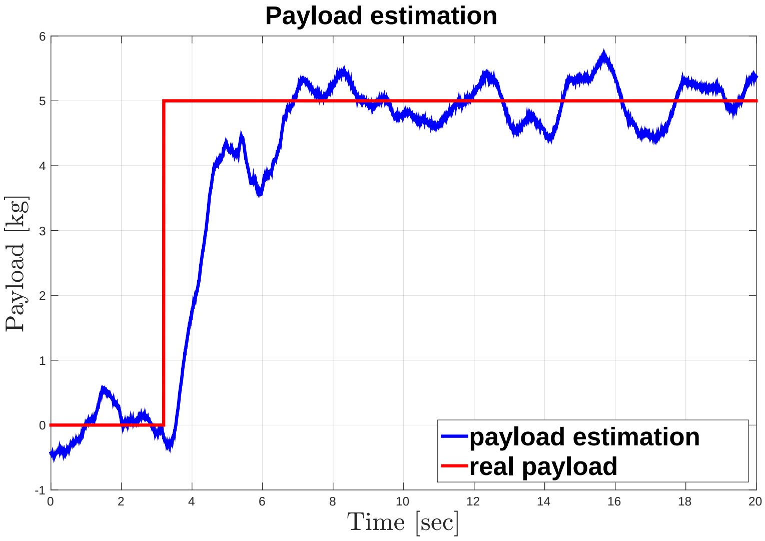

Figure 6.9: Payload estimation results of a $5kg$ payload added at the end-effector of robotic arm. The blue line represents payload to estimation and red line represents added payload at time $3.75s$.

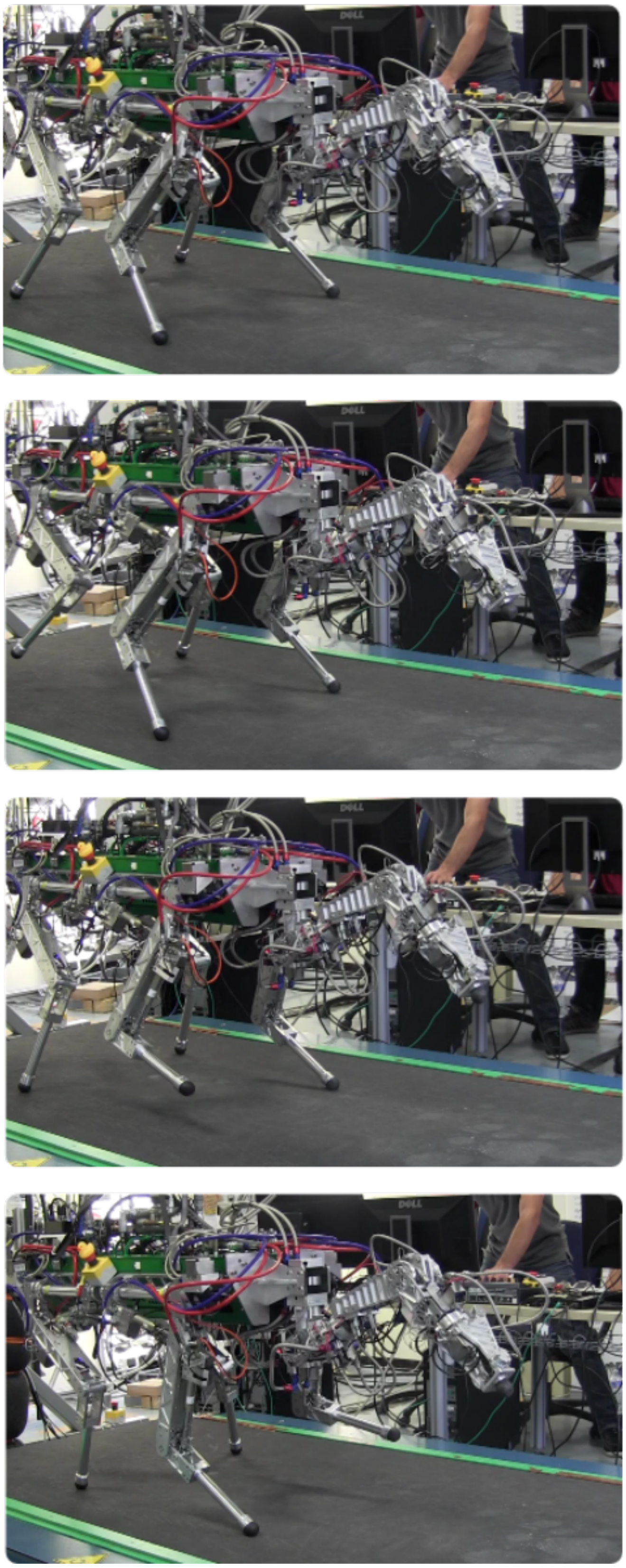

Figure 6.10: Snapshots of the walking experimental to evaluate the performance of our framework.

Chapter 7

Conclusion and Future Work

7.1 Conclusion

In this dissertation, I addressed a limitation presents in exiting quadruped robots, the lack of manipulation ability. The manipulation ability becomes essential for quadruped robots whose target applications require to manipulate an object, open a door, remove debris, or provide balance assistance. Indeed, a combination of quadruped locomotion stability with the ability to perform manipulation tasks can be crucial for search and rescue missions in natural disaster scenarios.

The commercially available robotic arms are not suitable for a quadruped robot which is meant to perform agile locomotion tasks such as HyQ. These existing robotic arms suffer from serious limitation; they are either too heavy, or slow, requires a bulky external control unit or just position controlled as described in Chapter 2. The limitations of these existing manipulators reduce the number of potential application scenarios as mentioned earlier and the possibility to be integrated onto an agile mobile robot such as HyQ. Hence what is required is a novel robotic arm which is compact, light-weight, torque controlled, and without an external control unit.

To this end, I designed and developed a compact hydraulic actuated robotic arm for quadruped robots. It can mount as a single or dual arm system configuration with a quadruped robot to create a multi-legged or centaur-like robot, respectively. The design evolution of the robotic arm is presented step-by-step in Chapter 3. Based on dual-arm system performance, physical, and design specifications, We simulated a centaur-like robot. The kinematic and dynamic simulation results, were used to select design parameters. The kinematic analysis were used to find the optimized design parameters for shoulder base attachment and each joint range-of-motion of the dual arm system as summarized in Table. 3.11 and Table 3.4, respectively. The dynamic simulation results were used to estimate the required joint torque and the speed. Based on kinematic and dynamic simulation results and to keep down the total weight of the overall robotic arm, I selected the smallest and lightest combination of commercially available actuators (see Table 3.9) and servo valves. The selected servo valves clearly provided more flow as estimated but their selection is also biased based on our group experiences with MOOG E024 servo valve.

In Chapter 4 I presented the mechanical design of a robotic arm called *HyArm*. The lightest combination of hydraulic actuators selected consisted of both hydraulic motors and cylinders. The hydraulic motors are compact and provide a constant torque output over their entire range-of-motion. To this end, I used hydraulic motors for shoulder joints (SAA, SFE and HR) and wrist joint (WR). Using hydraulic motors for the shoulder joint provided a compact design, and also brought the shoulder links and actuator mass closer to the base joint of the shoulder. The WR actuator is clearly not a perfect selection; it provides more than 50% torque then that required for the simulation task, but it is the smallest and lightest actuator commercially available and provides the required the joint range-of-motion. On the other hand, hydraulic cylinders used for the elbow joint EFE and wrist joint WFE have a higher power to weight ratio but required a linkage mechanisms to map cylinder linear force to torque. Using linkage mechanisms to convert cylinder force results in non-linear torque profiles. To design the linkage mechanisms for elbow (EFE) and wrist (WFE) joints, I approximated the required torque profiles for both joint with a non-liner curve that was used as objective function for optimization problem to find linkage mechanisms link lengths as given in Table. 4.4 and Table. 4.5, respectively. The hydraulic circuit, electronics and control layout are modular in designed, which allowed to use manipulator with either a fixed or mobile base platform.

The designed robotic arm is compact, light-weight ($12.5kg$). and able to carry a heavy payload of $10kg$ in the entire workspace, when attached to a fixed base. Hence, it is suitable to integrate with an agile quadruped robot such as HyQ. As an intermediate step for hardware integration of $HyArm$ and HyQ, I selected a single arm elbow-up configuration with HyQ as shown in Fig. 4.24. This configuration allows the manipulator to achieve a uniform workspace in front, below, and above the base robot trunk. In this configuration, the manipulator can be used to provide balance assistance for locomotion by acting as a fifth leg or perform manipulation tasks such as removing obstacles, opening a door or simple pick-up and place.

I also presented a low-level torque and high level controller for the designed robotic arm in Chapter 5. The low-level torque controller of HyArm is based on HyQ proposed by [Boaventura et al., 2012a]. I performed experiments to asses the performance of low-level torque control framework. With experimental results presented in Chapter 6, I concluded that the desired torque tracking is improved by adding an external payload (which resulted in a high load demand from actuators). The experimental results also established that the outer PD controller affecting the inner loop torque tracking. We proposed a control framework which integrated the high-level robotic arm controller with a mobile platform controller to ensure mobility and balance in Chapter 5. The high level arm controller, estimates and compensates external/internal disturbances while tracking a joint desired trajectory. The mobile platform controller stabilizes the CoM position and the robot trunk orientation while optimizing for the Ground Reaction Forces (GRFs). We presented experimental results on real robotic arm both with fixed base and mobile base. We carried out various experiments for a gradual assessment of the proposed high-level control framework as presented in Chapter 6. All the experimental results are also video documented. The video links are given in Chapter C.

7.2 Future Work

The future work from hardware will deal with improving hydraulic hose routing, the designing of a light-weight hydraulic gripper and attachment of real dual arm system with HyQ. In future, an extra $1DoF$ could be added to each designed robotic arm to create $7DoF$ robotic arm, which will allow to perform more complex manipulation tasks.

The future works for high level control framework will mainly focus on extending the arm controller and combining it with the mobile controller. The arm controller will be extended to achieve active impedance behaviour. It will allow the manipulator to be compliant when interacting with the environment but stiff otherwise. The arm will no longer be considered as separate from the controller of the legs. The arm joints will be incorporated in the optimization as if it was a fifth leg, and the end-effector force will be controlled in a similar fashion as the foot contact forces. Furthermore, we will be extending this control framework for the centaur-like robot and performing real world experiments.

Appendix A

List of Publications

- **B. U. Rehman**, M. Focchi, J. Lee, H. Dallali, D. G. Caldwell and C. Semini "Towards a Multi-legged Mobile Manipulator," IEEE International Conference on Robotics and Automation (ICRA), 2016 (Accepted).

- **B. U. Rehman**, M. Focchi, M. Frigerio, J. Gold smith, D. G. Caldwell and C. Semini, "Design of a Hydraulically Actuated Arm for a Quadruped Robot," in Proceedings of the International Conference on Climbing and Walking Robots (CLAWAR), 2015.

- C. Semini, J. Goldsmith, **B. Ur Rehman**, M. Frigerio, V. Barasuol, M. Focchi, D. G. Caldwell, "Design overview of the hydraulic quadruped robots HyQ2Max and HyQ2Centaur," The Fourteenth Scandinavian International Conference on Fluid Power (SICFP), 2015.

- P. La Hera, **B. U. Rehman**, D. Ortíz, "Electro-hydraulically actuated forestry manipulator: Modeling and Identification," IEEE International Conference on Intelligent Robots and Systems (IROS), 2012.

Appendix B

Kinematics Model of 6-DoF Robotic arm

This appendix presents the kinematic model of the 6-DoF robotic arm. The kianemtic model is used in chapter 3 to simulate robot.

B.1 Forward Kinematic Model of 6-DoF Arm

The forward kinematic equation relate the position and orientation of end-effector given the values for the joint variables of the robot. From a purely kinematic point of view, The HyArm (Fig. **??**) is a robot with 6-DoF as a chain of revolute joints. Inspired by human arm anatomy, each actuated joint is labelled as follows: Shoulder Adduction/Abduction (SAA), Shoulder Flexion/Extension (SFE), Humerus Rotation (HR), Elbow Flexion/Extension (EFE), Wrist Flexion/Extension (WFE) with relative coordinate frame are shown in Fig. B.1.

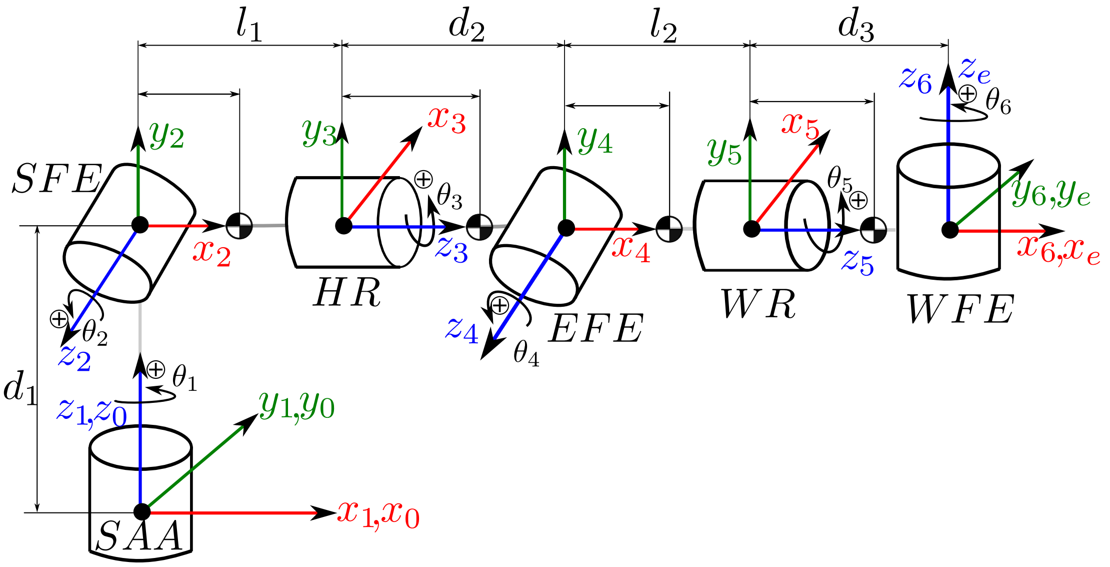

l_1
d_2
l_2
d_3
SFE
y_2
x_2
z_2
θ_2
y_3
x_3
θ_3
z_3
HR
y_4
x_4
z_4
θ_4
EFE
y_5
x_5
θ_5
z_5
WR
z_6
z_e
θ_6
y_6,y_e
x_6,x_e
WFE
d_1
θ_1
z_1,z_0
y_1,y_0
x_1,x_0
SAA

Figure B.1: The HyArm kinematics: Shoulder Adduction/Abduction (SAA), Shoulder Flexion/Extension (SFE), Humerus Rotation (HR), Elbow Flexion/Extension (EFE), Wrist Rotation (WR), Wrist Flexion/Extension (WFE), all the joint angles are shown at zero configuration

It is shown in Fig. B.1, link-frame assignments in the configuration corresponding to all joint angles are zero. Once the link frames and corresponding link parameters (Table. B.1) have been defined, kinematic equations is straight forward. The forward kinematics which relates end-effector (ee) position and orientation with respect to base-frame 0, given the joint angles can be define as:

$$T_6^0 = T_1^0 T_2^1 T_3^2 T_4^3 T_5^4 T_6^5 \tag{B.1}$$

where, each of the link transformations:

$$T_1^0 = Trans_{(0,0,0)} Rot_{(0,0,0)} = \begin{bmatrix} \cos(\theta_1) & -\sin(\theta_1) & 0 & 0 \\ \sin(\theta_1) & \cos(\theta_1) & 0 & 0 \\ 0 & 0 & 1 & 0 \\ 0 & 0 & 0 & 1 \end{bmatrix} \tag{B.2}$$

$$T_2^1 = Trans_{(0,0,d_1)} Rot_{(\frac{\pi}{2},0,0)} = \begin{bmatrix} \cos(\theta_2) & -\sin(\theta_2) & 0 & 0 \\ 0 & 0 & -1 & 0 \\ \sin(\theta_2) & \cos(\theta_2) & 0 & d_1 \\ 0 & 0 & 0 & 1 \end{bmatrix} \tag{B.3}$$

$$T_3^2 = Trans_{(l_1,0,0)} Rot_{(0,\frac{\pi}{2},0)} = \begin{bmatrix} 0 & 0 & 1 & l_1 \\ \sin(\theta_3) & \cos(\theta_3) & 0 & 0 \\ -\cos(\theta_3) & \sin(\theta_3) & 0 & 0 \\ 0 & 0 & 0 & 1 \end{bmatrix} \tag{B.4}$$

$$T_4^3 = Trans_{(0,0,d_2)} Rot_{(0,-\frac{\pi}{2},0)} = \begin{bmatrix} 0 & 0 & -1 & 0 \\ \sin(\theta_4) & \cos(\theta_4) & 0 & 0 \\ \cos(\theta_4) & -\sin(\theta_4) & 0 & d_2 \\ 0 & 0 & 0 & 1 \end{bmatrix} \tag{B.5}$$

$$T_5^4 = Trans_{(l_2,0,0)} Rot_{(0,\frac{\pi}{2},0)} = \begin{bmatrix} 0 & 0 & 1 & l_2 \\ \sin(\theta_5) & \cos(\theta_5) & 0 & 0 \\ -\cos(\theta_5) & \sin(\theta_5) & 0 & 0 \\ 0 & 0 & 0 & 1 \end{bmatrix} \tag{B.6}$$

$$T_6^5 = Trans_{(0,0,d_3)} Rot_{(-\frac{\pi}{2},0,-\frac{\pi}{2})} = \begin{bmatrix} \sin(\theta_6) & \cos(\theta_6) & 0 & 0 \\ 0 & 0 & 1 & 0 \\ \cos(\theta_6) & -\sin(\theta_6) & 0 & d_3 \\ 0 & 0 & 0 & 1 \end{bmatrix} \tag{B.7}$$

link lenght	values
d_1	$0.178m$
l_1	$0.112m$
d_2	$0.304m$
l_2	$0.112m$
d_3	$0.184m$

Table B.1: The HyArm: link lengths

Appendix C

Video links

- The youtube link of simulation of centaur-like robot and real robot experiments on designed robotic arm (under torque controlled): `http://youtu.be/JhbHPZc-NGU`
- The youtube link for experimental results of multi-legged robot: `https://youtu.be/RKwWxEc-ric`
- Reuters article on HyQ-centaur, link:
  `http://www.reuters.com/article/us-hyq-robot-idUSKCN0UP1FO20160111`
- Reuters HyQ-centaur article's youtube video link: `https://www.youtube.com/watch?v=UQIwtaAcLCs`

Bibliography

[Abe et al., 2013] Abe, Y., Stephens, B., Murphy, M. P., and Rizzi, A. A. (2013). Dynamic whole-body robotic manipulation. In *Proc. SPIE 8741, Unmanned Systems Technology*.

[Aero, 2015] Aero (2015). Aero. `https://plus.google.com/117741255440007459954/posts/CRCAUdp8weG`. Online; accessed 2015.

[Bagheri et al., 2015] Bagheri, M., Ajoudani, A., Lee, J., Caldwell, D., and Tsagarakis, N. (2015). Kinematic analysis and design considerations for optimal base frame arrangement of humanoid shoulders. In *Robotics and Automation (ICRA), 2015 IEEE International Conference on*.

[Barasuol et al., 2013] Barasuol, V., Buchli, J., Semini, C., Frigerio, M., Pieri, E. R. D., and Caldwell, D. G. (2013). A reactive controller framework for quadrupedal locomotion on challenging terrain. *2013 IEEE International Conference on Robotics and Automation (ICRA)*, pages 2554–2561.

[Bischoff et al., 2010] Bischoff, R., Kurth, J., Schreiber, G., Koeppe, R., Albu-Schaeffer, A., Beyer, A., Eiberger, O., Haddadin, S., Stemmer, A., Grunwald, G., and Hirzinger, G. (2010). The kuka-dlr lightweight robot arm - a new reference platform for robotics research and manufacturing. *Robotics (ISR), 2010 41st International Symposium on and 2010 6th German Conference on Robotics (ROBOTIK)*.

[Bluethmann et al., 2003] Bluethmann, W., Ambrose, R., Diftler, M., Askew, S., Huber, E., Goza, M., Rehnmark, F., Lovchik, C., and Magruder, D. (2003). Robonaut: A robot designed to work with humans in space. *Autonomous Robots*.

[Boaventura et al., 2015] Boaventura, T., Buchli, J., Semini, C., and Caldwell, D. (2015). Model-based hydraulic impedance control for dynamic robots. In *Robotics, IEEE Transactions on*.

[Boaventura et al., 2013] Boaventura, T., Cerda, G., Havoutis, I., Semini, C., Buchli, J., and Caldwell, D. G. (2013). Active compliance for highly-dynamic legged locomotion. *IEEE/RSJ International Conference on Intelligent Robots and Systems*. Accepted for publication.

[Boaventura et al., 2012a] Boaventura, T., Semini, C., Buchli, J., Frigerio, M., Focchi, M., and Caldwell, D. G. (2012a). Dynamic torque control of a hydraulic quadruped robot. *2012 IEEE International Conference on Robotics and Automation*, pages 1889–1894.

[Boaventura et al., 2012b] Boaventura, T., Semini, C., Buchli, J., Frigerio, M., Focchi, M., and Caldwell, D. G. (2012b). Dynamic torque control of a hydraulic quadruped robot. In *IEEE International Conference in Robotics and Automation*, pages 1889–1894.

[Bowling and Khatib, 2002] Bowling, A. and Khatib, O. (2002). Actuator selection for desired dynamic performance. In *Intelligent Robots and Systems, 2002. IEEE/RSJ International Conference on.*

[Chatzakos and Papadopoulos, 2008] Chatzakos, P. and Papadopoulos, E. (2008). The influence of dc electric drives on sizing quadruped robots. In *Robotics and Automation, 2008. ICRA 2008. IEEE International Conference on.*

[Cheng et al., 2007] Cheng, G., Hyon, S.-H., Morimoto, J., Ude, A., Hale, J., Colvin, G., Scroggin, W., and Jacobsen, S. (2007). Cb: a humanoid research platform for exploring neuroscience. *Advanced Robotics*, 21(10):1097–1114.

[Craig, 1989] Craig, J. J. (1989). *Introduction to Robotics: Mechanics and Control.* Addison-Wesley Longman Publishing Co., Inc.

[Dallali et al., 2013] Dallali, H., Mosadeghzad, M., Medrano-Cerda, G., Loc, V.-G., Tsagarakis, N., Caldwell, D., and Gesino, M. (2013). Designing a high performance humanoid robot based on dynamic simulation. In *Modelling Symposium (EMS), 2013 European.*

[Featherstone, 2007] Featherstone, R. (2007). *Rigid Body Dynamics Algorithms.* Springer, New York.

[FMC, 2015] FMC (2015). Fmc technologies. `http://www.fmctechnologies.com/en/SchillingRobotics/Schilling-Manipulators.aspx`. Online; accessed 2015.

[Focchi et al., 2013a] Focchi, M., Barasuol, V., Havoutis, I., Buchli, J., Semini, C., and Caldwell, D. G. (2013a). Local reflex generation for obstacle negotiation in quadrupedal locomotion. In *Int. Conf. on Climbing and Walking Robots (CLAWAR).*

[Focchi et al., 2013b] Focchi, M., Cerda, G. A., Boaventura, T., Frigerio, M., Semini, C., Buchli, J., and Caldwell, D. G. (2013b). Robot impedance control and passivity analysis with inner torque and velocity feedback loops. In *Transactions on industrial Electronics.*

[Focchi et al., 2015] Focchi, M., Del Prete, A., Havoutis, I., Featherstone, R., Caldwell, D., and Semini, C. (2015). High-slope Terrain Locomotion for Torque-Controlled Quadruped Robots. Technical report.

[Frigerio et al., 2012] Frigerio, M., Buchli, J., and Caldwell, D. G. (2012). Code generation of algebraic quantities for robot controllers. In *IEEE/RSJ International Conference on Intelligent Robots and Systems (IROS).*

[HDT, 2013] HDT (2013). Hdt global. `http://www.hdtglobal.com/series/robotics/`. Online; accessed July-2013.

[Hebert et al., 2015] Hebert, P., Bajracharya, M., Ma, J., Hudson, N., Aydemir, A., Reid, J., Bergh, C., Borders, J., Frost, M., Hagman, M., et al. (2015). Mobile manipulation and mobility as manipulationdesign and algorithms of robosimian. *Journal of Field Robotics.*

[Hirose et al., 2005] Hirose, S., Yokota, S., Torii, A., Ogata, M., Suganuma, S., Takita, K., and Kato, K. (2005). Quadruped walking robot centered demining system - development of titan-ix and its operation-. In *Robotics and Automation, 2005. ICRA 2005. Proceedings of the 2005 IEEE International Conference on.*

[HITACHI-ART, 2014] HITACHI-ART (2014). Hitachi-art centaur. `http://www.hitachi.co.jp/rd/portal/research/robotics/history/1990.html`. Online; accessed 2014.

[HITACHI-ART-CENTAUR, 1990] HITACHI-ART-CENTAUR (1990). Hitachi-art centaur. `http://cyberneticzoo.com/teleoperators/1984-93-nuclear-inspection-centaur-robot-art-project-japanese/`. Online; accessed 2013.

[HLK-40500R, 2015] HLK-40500R (2015). Hydro-lek. `http://www.hydro-lek.com/datasheets/Manipulators/HLK-40500R.pdf#view=FitH`. Online; accessed 2015.

[HLK-CRA6, 2015] HLK-CRA6 (2015). Hydro-lek. `http://www.hydro-lek.com/datasheets/Manipulators/HLK-CRA6.pdf#view=FitH`. Online: accessed 2015.

[HLK-HD6W, 2015] HLK-HD6W (2015). Hydro-lek. `http://www.hydro-lek.com/datasheets/Manipulators/HLK-HD6W.pdf#view=FitH`. Online: accessed 2015.

[Hogan, 1985] Hogan, N. (1985). Impedance control: An approach to manipulation: Part I – Theory. *ASME, Transactions, Journal of Dynamic Systems, Measurement, and Control*, 107:1–7.

[Hsia and Gao, 1990] Hsia, T. and Gao, L. (1990). Robot manipulator control using decentralized linear time-invariant time-delayed joint controllers. In *1990 IEEE International Conference on Robotics and Automation*, pages 2070–2075. IEEE.

[Hsia et al., 1991] Hsia, T., Lasky, T., and Guo, Z. (1991). Robust independent joint controller design for industrial robot manipulators. In *Industrial Electronics, IEEE Transactions on.*

[HYDRA-MP, 2015a] HYDRA-MP (2015a). Knr-systems. `http://rnd.knrsys.com/english/view.html?id_no=24&id_no1=5`. Online; accessed 2015.

[HYDRA-MP, 2015b] HYDRA-MP (2015b). Knr systems: youtube channel. `https://www.youtube.com/watch?v=XMtMc5ZR5YY`. Online accessed in 2015.

[HYDRA-UW, 2015] HYDRA-UW (2015). Knr-systems. `http://rnd.knrsys.com/english/view.html?id_no=25&id_no1=5`. 2015.

[iftler et al., 2011] iftler, M., Mehling, J., Abdallah, M., Radford, N., Bridgwater, L., Sanders, A., Askew, R., Linn, D., Yamokoski, J., Permenter, F., Hargrave, B., Piatt, R., Savely, R., and Ambrose, R. (2011). Robonaut 2 - the first humanoid robot in space. In *Robotics and Automation (ICRA), 2011 IEEE International Conference on.*

[Jaco, 2013] Jaco (2013). Jaco by kinova, reseller robotnik. `http://www.robotnik.eu/robotics-arms/kinova-jaco-arm/`. Online; accessed July-2013.

[Junichi et al., 1990] Junichi, A., Mineo, I., Takashi, N., and Asamu, A. (1990). Field test of aquatic walking robot for underwater inspection. In *Proceedings of the 7th ISARC, Bristol, United Kingdom.*

[Kaneko et al., 2002] Kaneko, K., Kajita, S., Kanehiro, F., Yokoi, K., Fujiwara, K., Hirukawa, H., Kawasaki, T., Hirata, M., and Isozumi, T. (2002). Design of advanced leg module for humanoid robotics project of meti. In *Robotics and Automation, 2002. Proceedings. ICRA '02. IEEE International Conference on.*

[Khan et al., 2015] Khan, H., Featherstone, R., Caldwell, D. G., and Semini, C. (2015). Bio-inspired knee joint mechanism for a hydraulic quadruped robot. In *International Conference on Automation, Robotics and Applications (ICARA).*

[Khan et al., 2013] Khan, H., Semini, C., Barasuol, V., and Caldwell, D. G. (2013). Actuator sizing for highly-dynamic quadruped robots based on squat jumps and running trots. In *Int. Conf. on Climbing and Walking Robots (CLAWAR).*

[Kucuk and Bingul, 2005] Kucuk, S. and Bingul, Z. (2005). Robot workspace optimization based on a novel local and global performance indices. In *Industrial Electronics, 2005. ISIE 2005. Proceedings of the IEEE International Symposium on.*

[Lee et al., 2013] Lee, J., Dallali, H., Tsagarakis, N., and Caldwell, D. (2013). Robust and model-free link position tracking control for humanoid coman with multiple compliant joints. In *International Conference on Humanoid Robots (Humanoids),.*

[Lee and Lee, 1988] Lee, S. and Lee, J. (1988). Task-oriented dual-arm manipulability and its application to configuration optimization. In *Decision and Control, 1988., Proceedings of the 27th IEEE Conference on.*

[Lenarčič and Thomas, 2002] Lenarčič, J. and Thomas, F. (2002). *Advances in robot kinematics: theory and applications.* Springer Science & Business Media.

[Lohmeier et al., 2006a] Lohmeier, S., Buschmann, T., Schwienbacher, M., Ulbrich, H., and Pfeiffer, F. (2006a). Leg design for a humanoid walking robot. In *Humanoid Robots, 2006 6th IEEE-RAS International Conference on.*

[Lohmeier et al., 2006b] Lohmeier, S., Buschmann, T., Ulbrich, H., and Pfeiffer, F. (2006b). Modular joint design for performance enhanced humanoid robot lola. In *Robotics and Automation, 2006. ICRA 2006. Proceedings 2006 IEEE International Conference on.*

[LWR-4D, 2013] LWR-4D (2013). Robotnik. `http://www.robotnik.eu/robotics-arms/lwa-4d/`. Onlined; accessed July-2013.

[Manring, 2005] Manring, N. (2005). *Hydraulic Control Systems.* Wiley.

[Munsang et al., 1999] Munsang, K., Sungchul, K., Sooyong, L., Woojin, C., Kyoungrae, C., and Chong-Won, L. (1999). Development of a humanoid robot centaur-design, human interface, planning and control of its upper-body. In *Systems, Man, and Cybernetics, 1999. IEEE SMC '99 Conference Proceedings.*

[Orin et al., 2013] Orin, D. E., Goswami, A., and Lee, S.-H. (2013). Centroidal dynamics of a humanoid robot. *Autonomous Robots*, 35(2-3):161–176.

[Ott et al., 2006] Ott, C., Eiberger, O., Friedl, W., Bauml, B., Hillenbrand, U., Borst, C., Albu-Schaffer, A., Brunner, B., Hirschmuller, H., Kielhofer, S., Konietschke, R., Suppa, M., Wimbock, T., Zacharias, F., and Hirzinger, G. (2006). A humanoid two-arm system for dexterous manipulation. In *IEEE-RAS International Conference on Humanoid Robots,.*

[Ott et al., 2010] Ott, C., Mukherjee, R., and Nakamura, Y. (2010). Unified impedance and admittance contro. In *IEEE International Conference on Robotics and Automation (ICRA).*

[Ott et al., 2011] Ott, C., Roa, M. a., and Hirzinger, G. (2011). Posture and balance control for biped robots based on contact force optimization. *2011 11th IEEE-RAS International Conference on Humanoid Robots*, pages 26–33.

[Parmiggiani et al., 2012] Parmiggiani, A., Metta, G., and Tsagarakis, N. (2012). The mechatronic design of the new legs of the icub robot. In *Humanoid Robots (Humanoids), 2012 12th IEEE-RAS International Conference on.*

[Patel and Sobh, 2014] Patel, S. and Sobh, T. (2014). Manipulator performance measures-a comprehensive literature survey. In *Journal of Intelligent & Robotic Systems.*

[Raibert and Craig, 1981] Raibert, M. and Craig, J. (1981). Hybrid position/force control of manipulators. *ASME Journal of Dynamic Systems, Measurement, and Control*, 107:126–133.

[Rainer et al., 2010] Rainer, B., Kurth, J., Schreiber, G., Koeppe, R., Albu-Schffer, A., Beyer, A., Eiberger, O., Haddadin, S., Stemmer, A., Grunwald, G., and Hirzinger, G. (2010). The KUKA-DLR lightweight robot arm - a new reference platform for robotics research and manufacturing in robotics (isr). In *41st int. symposium on and 2010 6th german conference on robotics (robotik).*

[Rehman et al., 2015] Rehman, B. U., Focchi, M., Frigerio, M., Goldsmith, J., Caldwell, D. G., and Semini, C. (2015). Design of a hydraulically actuated arm for a quadruped robot. In *Proceedings of the International Conference on Climbing and Walking Robots (CLAWAR).*

[Rehman et al., 2016] Rehman, B. U., Focchi, M., Lee, J., Dallali, H., Caldwell, D. G., and Semini, C. (2016). Towards a multi-legged mobile manipulator. In *IEEE International Conference on Robotics and Automation (ICRA) (Accepted).*

[Roennau et al., 2014] Roennau, A., Heppner, G., Nowicki, M., and Dillmann, R. (2014). Lauron v: a versatile six-legged walking robot with advanced maneuverability. In *Advanced Intelligent Mechatronics (AIM), 2014 IEEE/ASME International Conference on.*

[Schaal, 2006] Schaal, S. (2006). The SL simulation and real-time control software package. Technical Report, (Online) Accessed February 2011 at *http://www-clmc.usc.edu/publications/S/schaal-TRSL.pdf.*

[Semini, 2010] Semini, C. (2010). *HyQ – Design and Development of a Hydraulically Actuated Quadruped Robot.* PhD thesis, Istituto Italiano di Tecnologia (IIT) and University of Genova.

[Semini et al., 2015] Semini, C., Barasuol, V., Boaventura, T., Frigerio, M., Focchi, M., Caldwell, D. G., and Buchli, J. (2015). Towards versatile legged robots through active impedance control. *The International Journal of Robotics Research (IJRR).*

[Semini et al., 2012] Semini, C., Khan, H., Frigerio, M., Boaventura-Cunha, T., Focchi, M., Buchli, J., and Caldwell, D. G. (23-26 july 2012). Design and scaling of versatile quadruped robots. *Fifteenth International Conference on Climbing and Walking Robots and the Support Technologies for Mobile Machines, Baltimore, USA*, pages pp. 273–280.

[Semini et al., 2011] Semini, C., Tsagarakis, N. G., Guglielmino, E., Focchi, M., Cannella, F., and Caldwell, D. G. (2011). Design of HyQ - a hydraulically and electrically actuated quadruped robot. *IMechE Part I: Journal of Systems and Control Engineering*, 225(6):831–849.

[Siciliano and Khatib, 2008] Siciliano, B. and Khatib, O., editors (2008). *Springer Handbook of Robotics.* Springer.

[Spong et al., 2006] Spong, M. W., Hutchinson, S., and Vidyasagar, M. (2006). *Robot modeling and control.* John Wiley & Sons.

[Stephens and Atkeson, 2010] Stephens, B. J. and Atkeson, C. G. (2010). Push recovery by stepping for humanoid robots with force controlled joints. In *Humanoids.*

[Suganuma et al., 2003] Suganuma, S., Ogata, M., Takita, K., and Hirose, S. (2003). Development of detachable tele-operation gripper for the walking robot. In *Intelligent Robots and Systems, 2003. (IROS 2003). Proceedings. 2003 IEEE/RSJ International Conference on.*

[Thomas et al., 1985] Thomas, M., Yuan-Chou, H., and Tesar, D. (1985). Optimal actuator sizing for robotic manipulators based on local dynamic criteria. In *ASME. J. Mech., Trans., and Automation.*

[Townsend and Salisbury, 1993] Townsend, W. T. and Salisbury, J. K. (1993). Mechanical design for whole-arm manipulation. *Robots and Biological Systems: Towards a New Bionics?*

[Tsagarakis et al., 2013] Tsagarakis, N., Morfey, S., Cerda, G., Zhibin, L., and Caldwell, D. (2013). Compliant humanoid coman: Optimal joint stiffness tuning for modal frequency control. In *Robotics and Automation (ICRA), 2013 IEEE International Conference on.*

[Tsuda et al., 2007] Tsuda, S., Oda, Y., Shinozaki, K., and Nakatsu, R. (2007). Concept and architecture of a centaur robot. In *Entertainment Computing ICEC 2007, Springer Berlin Heidelberg.*

[Tsuda et al., 2010] Tsuda, S., Shinozaki, K., and Nakatsu, R. (2010). Development and evaluation of a centaur robot. In *Service Robotics and Mechatronics, Springer.*

[UR, 2013] UR (2013). Universal robots. `http://www.universal-robots.com/products/`. Online; accessed 2013.

[WAM, 2013] WAM (2013). Barrett technology. `http://www.barrett.com/products-arm.htm`. Online; accessed July-2013.

[Whitney, 1987] Whitney, D. (1987). Historical perspective and state of the art in robot force control. *Int J Robotics Research*, 6(1):3–14.

[Winkler et al., 2014] Winkler, A., Havoutis, I., Bazeille, S., Ortiz, J., Focchi, M., Caldwell, D. G., and Semini, C. (2014). Path planning with force-based foothold adaptation and virtual model control for torque controlled quadruped robots. In *IEEE International Conference on Robotics and Automation (ICRA).*

[Ylonen and Halme, 2002] Ylonen, S. and Halme, A. (2002). Workpartner - centaur like service robot. In *Intelligent Robots and Systems, 2002. IEEE/RSJ International Conference on.*

[Yoshikawa, 1985] Yoshikawa, T. (1985). Manipulability of robotic mechanisms. In *The international journal of Robotics Research.*

[Youcef-Toumi and Ito, 1988] Youcef-Toumi, K. and Ito, O. (1988). A time delay controller for systems with unknown dynamics. In *American Control Conference, 1988.*

[Youcef-Toumi and Wu, 1992] Youcef-Toumi, K. and Wu, S.-T. (1992). Input/output linearization using time delay control. *Journal of dynamic systems, measurement, and control*, 114(1):10–19.